

To the University of Wyoming:

The members of the Committee approve the thesis of Clint Dunn presented on August 21, 2018.

Michael Stöllinger, Chairperson

David Bell, External Department Member

Erica Belmont

APPROVED:

Carl Frick, Head, Mechanical Engineering

Michael Pishko, Dean, College of Engineering and Applied Sciences

Dunn, Clint, Computational modeling of coal devolatilization and soot formation in Open-FOAM., M.S., Mechanical Engineering, August, 2018.

Reactive multiphase flows, such as those that occur in pulverized coal combustion, are complex processes that present unique modeling challenges. Accurately predicting soot formation and consumption, which is, in turn, strongly dependent on devolatilization and tar decomposition, is often an integral part of modeling these flows well. In this work previously developed models for coal tar decomposition and soot formation/consumption are extended to couple fully with finite rate chemistry computational fluid dynamic simulations. Alternatives to these traditional approaches that rely on coal chemistry analysis software predictions are also developed. The models are used to simulate laminar entrained coal co-flow burner experiments and the results are compared.

# COMPUTATIONAL MODELING OF COAL DEVOLATILIZATION AND SOOT FORMATION IN OPENFOAM.

by

**Clint Dunn,**

A thesis submitted to the  
Mechanical Engineering  
and the  
University of Wyoming  
in partial fulfillment of the requirements  
for the degree of

MASTER OF SCIENCE  
in  
MECHANICAL ENGINEERING

Laramie, Wyoming  
August 2018

Copyright © 2018

by

Clint Dunn

I dedicate this thesis to my parents who have supported me constantly throughout my various academic endeavors and have always believed in me.

# Contents

<b>List of Figures</b>	<b>vii</b>
<b>List of Tables</b>	<b>xi</b>
<b>Nomenclature</b>	<b>xii</b>
<b>Acknowledgments</b>	<b>xiv</b>
<b>Chapter 1 Introduction and Background</b>	<b>1</b>
1.1 Introduction . . . . .	1
1.2 Background . . . . .	2
1.2.1 Coal Devolatilization Modeling . . . . .	3
1.2.2 Soot Formation Modeling . . . . .	8
1.3 Thesis Organization . . . . .	13
<b>Chapter 2 Continuous Phase Modeling in OpenFOAM</b>	<b>14</b>
2.1 Overview . . . . .	14
2.2 Laminar Combustion Modeling . . . . .	16
2.3 Radiation Modeling . . . . .	22
2.3.1 Absorption Models . . . . .	23
<b>Chapter 3 Dispersed Phase Modeling in OpenFOAM</b>	<b>25</b>
3.1 Overview . . . . .	25
3.2 Particle Velocity, Temperature and Mass Conservation Equations . . . . .	31

3.2.1	Particle Velocity Equation . . . . .	31
3.2.2	Particle Temperature Equation . . . . .	32
3.2.3	Particle Mass Equation . . . . .	33
3.2.4	Integration of Particle Equations . . . . .	34
3.3	Devolatilization . . . . .	35
3.3.1	Dispersed Phase Source Terms . . . . .	37
3.3.2	Continuous Phase Source Terms . . . . .	38
3.4	Evaporation . . . . .	39
3.5	Radiation . . . . .	40
3.6	Convection and Drag Force Reaction Source Terms . . . . .	41
<b>Chapter 4</b>	<b>Modifications and Additions</b>	<b>43</b>
4.1	Primary Devolatilization . . . . .	46
4.1.1	AnalyticalSFORDevolatilization Model . . . . .	46
4.1.2	Using PCCL to Predict Rate Constants for the AnalyticalSFORDe- volatilization Model . . . . .	47
4.1.3	NthOrderDevolatilization Model . . . . .	49
4.2	Two Equation Soot Model . . . . .	50
4.2.1	Density Calculation Modifications for Soot . . . . .	55
4.2.2	Radiation Contribution of Soot . . . . .	56
4.3	Tar Decomposition Modeling . . . . .	57
4.3.1	Tar Tracking Model . . . . .	57
4.3.2	PC Tar Decomposition Model . . . . .	60
4.3.3	PCCL Conversion Framework (PCF) . . . . .	62
4.3.4	Note on Model Nomenclature . . . . .	67
<b>Chapter 5</b>	<b>Validation</b>	<b>70</b>
5.1	BYU Flat Flame Burner Case Setup . . . . .	71
5.1.1	Boundary Conditions . . . . .	73
5.1.2	Particle Free Comparison . . . . .	75

5.1.3	Comparison with Coal Particles . . . . .	76
<b>Chapter 6</b>	<b>Results</b>	<b>80</b>
6.1	Particle Free Simulations . . . . .	81
6.2	Utah Hiawatha with Co-flow Equivalence Ratio 1.30 . . . . .	82
6.3	Utah Hiawatha Coal with Co-flow Equivalence Ratio 1.26 . . . . .	90
6.4	Pittsburgh # 8 Coal with Co-flow Equivalence Ratio 1.30 . . . . .	90
6.5	Tar and Soot Mass Fraction Predictions . . . . .	92
<b>Chapter 7</b>	<b>Conclusions and Future Work</b>	<b>95</b>
<b>Appendix A</b>	<b>DRM-22 Mechanism</b>	<b>99</b>
A.1	Kinetics . . . . .	99
A.2	Thermodynamics . . . . .	104
<b>Appendix B</b>	<b>Input Files</b>	<b>112</b>
B.1	coalCloudProperties . . . . .	112
<b>References</b>		<b>120</b>



# List of Figures

1.1	Overview of a typical flow reactor. The dashed line on the bottom of the figure indicates symmetry and represents the centerline of the reactor. The solid black lines represent reactor walls. As the coal is injected it is heated by a co-flow, commonly composed of heated air. As the coal is heated it undergoes evaporation, devolatilization and char combustion/surface reactions. Once the volatiles are released from the coal particles they react with the gaseous environment of the reactor and potentially form soot. If a large reactor body is present then a significant amount of hot product gas recirculation is often present and aids in heat transport. . . . .	3
1.2	PCCL prediction and integrated fitted rate of volatile mass fraction yield ( $y_v$ ) for Utah Hiawatha coal on a DAF basis. . . . .	7
1.3	Diagram of devolatilization and tar breakdown pathways for Utah Hiawatha coal predicted by PCCL. All percentages are mass fractions of the initial DAF particle mass. . . . .	8
1.4	Overview of soot formation pathways. Taken from Dasgupta et al. [1]. . . . .	9
2.1	One dimensional mesh composed of three cells, W,C and E. The faces between the two cells are named a and b. . . . .	17

3.1	A representation of various parcel properties within a two dimensional mesh. In the two leftmost cells of the top row the representation of two different diameter coal particles (distinguished by color) by parcels is illustrated. On the middle row of cells the trajectory of a parcel $x_p(t)$ through several cells is represented by a black line. The instantaneous parcel velocity $U_p(t)$ is represented by the attached red arrow. In the bottom center cell the contributions of three parcels to the density transport equation source term is depicted. . .	27
3.2	Species mass fraction breakdown within each phase of Utah Hiawatha coal predicted by C3M/CPD on an as received basis. . . . .	30
4.1	Diagram of devolatilization and tar breakdown pathways within the TT model.	57
4.2	Diagram of devolatilization and tar breakdown pathways within the PC model.	60
4.3	Mass fractions of primary tar, secondary tar and soot in the zero dimensional reactor representing the particle environment. . . . .	65
4.4	Result of soot formation rate constant optimization. . . . .	67
4.5	Result of soot formation and cracking rate constant optimization. . . . .	68
5.1	Schematic of the flat flame Hencken style burner used by Ma. Figure taken from Ma [2]. . . . .	71
5.2	Simulation geometry. . . . .	72
5.3	On the left the entire inlet plane of the axisymmetric simulation is pictured. On the right a magnified image of the bottom tip of the inlet plane is shown. In both images the blue regions represent the co-flow inlet while the red region represents the coal entrainment inlet. The thin interior black lines represent cell faces. . . . .	73
6.1	Centerline temperature plot of a particle free simulation compared to the corresponding experimental data from Ma [2] for a co-flow equivalence ratio $\phi = 1.26$ . Temperatures are in Kelvin. . . . .	82

6.2	Centerline temperature plot of a particle free simulation compared to the corresponding experimental data from Ma [2] for co-flow equivalence ratio $\phi = 1.30$ . . . . .	83
6.3	Simulated soot yield compared with experimental data, illustrating the effect of the soot growth reaction. The Utah Hiawatha coal is used at a co-flow equivalence ratio of $\phi = 1.30$ . . . . .	84
6.4	Simulated soot yield compared with experimental data with the TT and PCF model both utilizing the CPD model for primary devolatilization. The Utah Hiawatha coal is used at a co-flow equivalence ratio of $\phi = 1.30$ . . . . .	86
6.5	Mass fractions of primary tar, secondary tar, soot and secondary gases in the zero dimensional reactor representing the particle environment. . . . .	87
6.6	Comparison of the Arrhenius rates determined with the PCF to those from Brown and Ma [2,3] . . . . .	88
6.7	Simulated soot yield compared with experimental data with the TT, PC and PCF model utilizing the PCCL model for primary devolatilization. The Utah Hiawatha coal is used at a co-flow equivalence ratio of $\phi = 1.30$ . . . . .	89
6.8	Soot gasification rate [ $kmol/(m^3s)$ ] with $CO_2$ for the CPD/TT model simulation case without soot growth. Pictured is the central plane of the simulation domain. The bottom axis is aligned with the central axis of the flow and the vertical axis represents radial displacement, both are in units of $[m]$ . . . . .	90
6.9	Simulated soot yield compared with experimental data for Utah Hiawatha coal at a co-flow equivalence ratio of $\phi = 1.26$ . . . . .	91
6.10	Simulated soot yield compared with experimental data for Pittsburgh #8 coal at a co-flow equivalence ratio of $\phi = 1.30$ . . . . .	92
6.11	Simulated tar mass fraction and solid particle fraction. This is the result of a simulation performed with the PCCL/TT model combination with the $\phi = 1.30$ co-flow equivalence ratio. The unit of the axes is meters. . . . .	93

6.12 Simulated soot mass fraction and solid particle fraction. This is the result of a simulation performed with the PCCL/TT model combination with the $\phi = 1.30$ co-flow equivalence ratio. The unit of the axes is meters. . . . .	94
--	----

# List of Tables

4.1	Comparison of the Arrhenius rate constants for soot formation (sf) and tar cracking (cr) calculated through the PCCL Conversion Framework and those determined from experimental data by Ma [2]. Activation energies have units of [kJ/mol] and pre-exponential factors have units of [1/s]. . . . .	67
5.1	BYU flat flame burner experiment co-flow inlet conditions adapted from Table 3.1 in Ma [2]. All species flow rates are given in units of standard liters per minute with the standard conditions of 298 [K] and 1.0 [atm]. . . . .	73
5.2	Summary of flat flame burner simulation co-flow inlet species boundary conditions. The inlet conditions are given as mass fractions following equilibration.	74
5.3	Flat flame burner simulation boundary conditions. . . . .	75
5.4	Primary devolatilization yields for Utah Hiawatha Coal. . . . .	77
5.5	Primary devolatilization yields for Pittsburgh #8 Coal. . . . .	78
6.1	Experimental case and simulation comparison matrix. The three experimental cases investigated are Utah Hiawtha at 1800 and 1900 heating conditions, UH 1900 and UH 1800; as well as the Pittsburgh #8 coal at the 1800 heating condition, P8 1800. The simulation models used are specified by the primary devolatilization model used , CPD or PCCL and the tar decomposition model used TT, PC or PCF. When the TT tar decomposition model was employed the activation of the soot model is indicated by ‘ng’ for no soot growth reaction and g for when the soot growth reaction is considered. . . . .	81

# Nomenclature

<b>Variables</b>		$E_p$	particle emission contribution
$\alpha$	thermal diffusivity	$G$	incident radiation intensity
$\dot{m}$	mass flow rate	$h_{f,\alpha}$	enthalpy of formation, species $\alpha$
$\phi$	equivalence ratio	$h_{s,\alpha}$	sensible enthalpy, species $\alpha$
$\psi$	compressibility	$I$	radiative intensity
$\rho$	density	$M$	molar mass
$\sigma_p$	particle scattering coefficient	$m$	mass
$\tilde{Y}$	mass fraction of daf intitial particle mass	$N_S$	soot particle number density
$A$	pre-exponential Arrhenius rate constant	$R$	universal gas constant
		$S$	source term
$a$	absorption coefficient	$T$	temperature
$c_p$	specific heat capacity	$U$	velocity
$D$	diffusivity	$Y$	mass fraction
$dm$	particle mass loss increment	$y$	yield, mass released normalized by initial particle mass
$E$	activation energy Arrhenius rate constant		

## Constants

$\sigma$       Steffan Boltzmann constant

### **Subscripts**

$\alpha$       species  $\alpha$

$c$       combustion

$g$       gas phase

$gs$       contribution of soot and gas

$h$       source for enthalpy equation

$m$       source for continuity equation

$p$       particles

$r$       radiation

$s$       soot

$u$       source for momentum equation

$v$       volatiles

$vap$       vaporization

$y$       source for species equations

### **Superscripts**

0      initial value

$\infty$       ultimate value

$conv$       source from convection

$daf$       dry ash free basis

$dev$       source from devolatilization

$drag$       source derived the drag force

$evap$       source from evaporation

# Acknowledgments

I would like to acknowledge and thank my committee members Dr. Stöllinger, Dr. Belmont and Dr. Bell for their support. This work was funded by grants from the University of Wyoming through an Enery GA scholarship and the School of Energy Resources. The computational resources used here were provided by the University of Wyoming Advanced Research Computing Center [4].

CLINT DUNN

*University of Wyoming*

*August 2018*



# Chapter 1

## Introduction and Background

### 1.1 Introduction

With increasing interest in finding alternative uses for coal it becomes more necessary than ever to develop models that can capture important processes involved in coal processing and elucidate their relevance to a given application. A myriad of processes have been developed to utilize coal resources including directly extracting its chemical energy through combustion, e.g. in coal fired power plants, or using it as a precursor for more valuable or readily transported fuels and products like syngas or polycyclic aromatic hydrocarbons (PAHs). Regardless of the specific process considered in order to design facilities that operate efficiently and cleanly it is necessary to possess a deep understanding of the processes that take place during coal breakdown. Of particular importance to all of these processes is coal particle devolatilization as well as the subsequent tar and soot formation and breakdown.

This work focuses on advancing state of the art models for pulverized coal particle devolatilization, tar decomposition and soot formation by coupling previous work with a more robust treatment of the hydrocarbon combustion chemistry that often accompanies coal processing. Previous modeling efforts provide a solid footing for modeling the coal decomposition processes but often have had to rely on simple hydrocarbon combustion models. This reliance precludes the full coupling of species and energy transfer between coal processes and the primary combustion model.

The importance of maintaining a tight coupling between soot/tar chemistry and the primary chemistry varies with the application. In situations with very low coal loadings, for example, the mass discrepancies that occur without accounting for this coupling can be minimal. However in situations when coal loadings are high, including the interplay with the primary chemistry can have important effects.

In this work, we utilize the open source computational fluid dynamics (CFD) package OpenFOAM [5] to perform these simulations. OpenFOAM offers many advantages over alternative CFD packages. The source code is freely available and the design of the software makes it relatively easy to implement new high level models without needing to re-implement low level CFD implementations. Of particular interest here is the ease with which high level Lagrangian particle models, such as devolatilization, can be modified or created while the underlying particle transport and phase exchange mechanisms remain intact. Furthermore, OpenFOAM provides a framework for modeling reactive, variable density, low Mach number flows that is easily coupled to the Lagrangian particle simulations.

## 1.2 Background

This work focuses on modeling three key aspects of pulverized coal combustion: coal particle devolatilization, coal tar decomposition and soot formation. In this section, an overview of coal combustion modeling is provided that describes the processes involved. Pulverized coal combustion is commonly modeled as consisting of three steps that occur sequentially as the particle is heated. First, any water stored within the particle structure is evaporated. Once the evaporation step is completed devolatilization occurs. Devolatilization is the temperature dependent process in which the solid structure of the coal particle degrades to form gaseous species, referred to as volatiles, that are then ejected from the particle. When devolatilization is finished the surface reaction model becomes active and the char remaining within the particle is heterogeneously reacted with the ambient gases. In most circumstances the most important surface reaction is the oxidation of the carbon within the char to form  $CO_2$  and  $CO$ . These three processes are illustrated within the context of a typical flow reactor in

Figure 1.1.

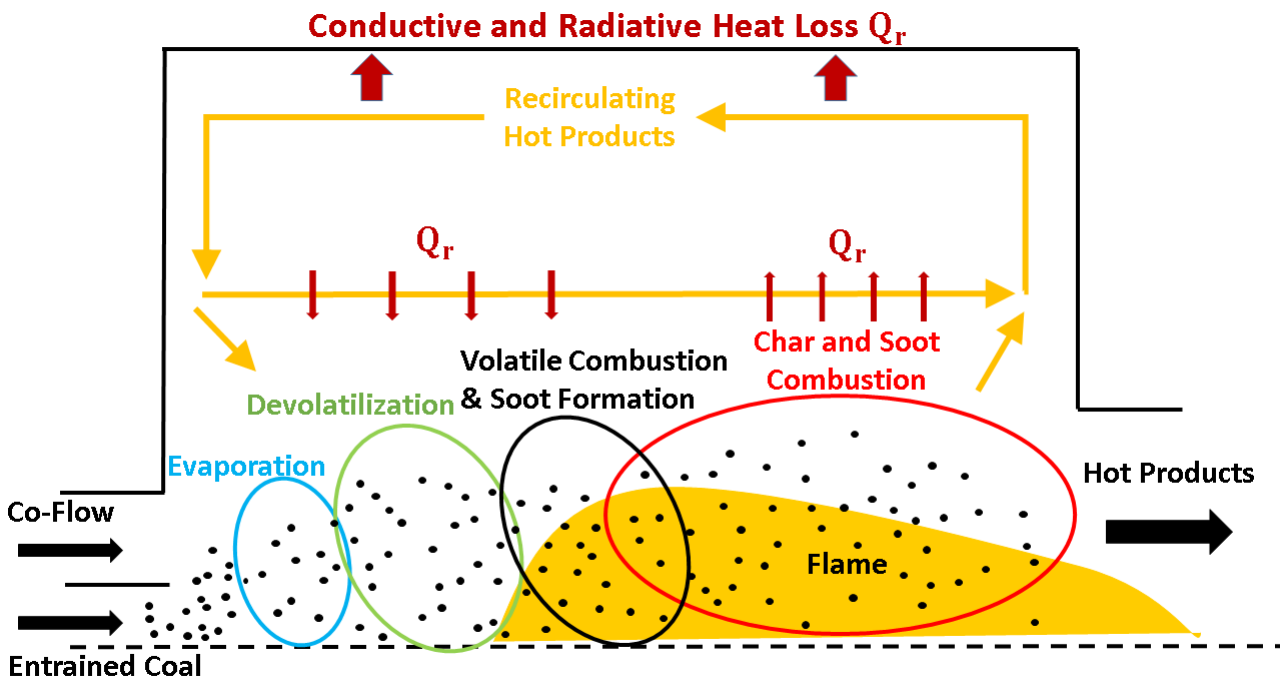


Figure 1.1: Overview of a typical flow reactor. The dashed line on the bottom of the figure indicates symmetry and represents the centerline of the reactor. The solid black lines represent reactor walls. As the coal is injected it is heated by a co-flow, commonly composed of heated air. As the coal is heated it undergoes evaporation, devolatilization and char combustion/surface reactions. Once the volatiles are released from the coal particles they react with the gaseous environment of the reactor and potentially form soot. If a large reactor body is present then a significant amount of hot product gas recirculation is often present and aids in heat transport.

Focus in this research is place on devolatilization and the subsequent formation of soot from the volatile tar. The next two subsections provide a review of the currently available modeling techniques for both processes.

### 1.2.1 Coal Devolatilization Modeling

Coal particle devolatilization is the process wherein gaseous products, i.e. volatiles, are released from the particle upon heating. A significant percentage of the chemical energy stored in a particle is present in these volatile gases. This illustrates the importance of

understanding and properly modeling the process if a comprehensive coal modeling approach is desired.

The composition and quantity of the volatile gases can vary widely depending on the heating environment and type of coal. The composition usually consists of light hydrocarbons and other non-condensable gases, e.g.  $CH_4$ ,  $H_2$ ,  $CO$ , and  $CO_2$ , as well as larger aromatic hydrocarbons that vary in size but are generally referred to as a group as tar. It has been well documented that the total volatile yield is strongly related to the heating rate in addition to the ultimate temperature [6]. This effect often results in volatile yields that significantly exceed what is predicted by the proximate analysis of the coal [7]. Furthermore, the rate of devolatilization of a particular type of coal is also a function of the heating environment and can vary widely.

Many models have been developed to describe devolatilization. They range from simple differential equations fitted to experimental devolatilization data, e.g. single kinetic rate/single first order rate (SFOR) [8,9] or distributed activation energy models [10], to more complex coal chemistry simulation programs that seek to model the underlying chemical mechanics present in coal particles to predict overall rates, e.g. Chemical Percolation Devolatilization (CPD) [11] or FlashChain (the central algorithm used in P.C. Coal Lab (PCCL)) [12].

The more complex models can accurately account for the varying heating rates and temperatures conditions that a coal particle might experience and these conditions can strongly affect devolatilization. The advantage of the simpler models is that they can be more readily included in already complex and computationally expensive CFD simulations where the direct use of the coal chemistry simulation models at each iteration could become prohibitively expensive. These simple rate models are usually reliant on rate parameters fit to experimental data that may not accurately represent the environment faced by the particles during the simulation, particularly the single kinetic rate model. Another disadvantage of the simple rate models is the need to determine the rate constants, often through matching yields to experimental results.

A common compromise which leverages the strengths of both model classes is to first use the more advanced models like CPD or PCCL to predict devolatilization characteristics

for a particular experiment. Then these rates can be used to fit the simpler models, e.g. SFOR, rate constants. Effectively the coal chemistry models provide a virtual experiment which is then used to determine the rate constants for simple models [12]. This allows the rate constants to be tailored to the coal flow of interest while maintaining computational tractability in CFD devolatilization submodels.

This approach is adopted here and we use PCCL and CPD to provide rate constants for a SFOR model used in our CFD implementation. Both are capable of predicting devolatilization rates and yields based on a user prescribed heating condition and the proximate/ultimate analysis of the coal. PCCL is capable of predicting speciated devolatilization rates and yields, i.e. individual rates and yields for each volatile species. Furthermore PCCL provides a sub-module that predicts the evolution of coal tar following its devolatilization. The implementation of CPD we use, C3M [13], predicts speciated yields but the rate used for all volatiles, including tar, is the same.

CPD is utilized here in order to remain consistent with previous studies [2, 14] that also used it to predict devolatilization behavior. PCCL is used in addition to CPD for two reasons. First, we are interested in investigating the effect that varying the devolatilization predictions can have on the overall simulation results, i.e. what effect does using PCCL rather than CPD have on the simulation results. Second, one of the models developed in this work, the PC model, described in Section 4.3.2, is based largely on leveraging the tar decomposition and soot formation predictions provided by PCCL that are not present in CPD.

A general introduction to the SFOR devolatilization model usage is presented below, the implementation in OpenFOAM is discussed in Chapter 3, and our additions and modifications to the model are discussed in Chapter 4.

To use the SFOR model in a CFD simulation the initial volatile mass,  $m_v^0$ , and two rate constants; the pre-exponential factor,  $A$ , and the activation energy,  $E$ , must be known before hand. They can be determined either from experiments or coal chemistry software, e.g. PCCL. Then a differential equation can be formed to describe the volatile mass loss of

the particle due to devolatilization as

$$\frac{dm_v}{dt} = -A \cdot \exp\left(\frac{-E}{RT_p}\right) \cdot m_v \quad (1.1)$$

where  $m_v$  is the mass of volatile gases remaining in the particle, yet to be devolatilized,  $R$  is the universal gas constant and  $T_p$  is the particle temperature. Initially  $m_v = m_v^0$  when the particle is injected into the simulation. After the particle is injected it is heated by the hot gases and devolatilization occurs until the volatile gases are completely released.

An alternative quantification of the mass loss due to devolatilization is the volatile mass fraction yielded,  $y_v$ . It should be thought of as the fraction of the initial particle mass that has been devolatilized. It can be calculated on either an ‘as received’ basis which includes the mass of water and ash present in the particle initially or a ‘dry ash free’ (DAF) basis which does not. It begins at zero and progresses to an ultimate yield,  $y_v^\infty$ . Note that when  $y_v^\infty$  is given on an as received basis that  $m_v^0/m_p^0 = y_v^\infty$  where  $m_p^0$  is the initial particle mass. As Equation 1.1 describes the mass loss of a particle it can be reformulated to also describe the mass fraction yielded using the same rate constants,  $A$  and  $E$ , as

$$\frac{dy_v}{dt} = A \cdot \exp\left(\frac{-E}{RT_p}\right) \cdot (y_v^\infty - y_v) \quad (1.2)$$

Using PCCL the ultimate mass fraction yield of volatiles,  $y_v^\infty$ , for one of the bituminous coals used in this research, Utah Hiawatha, with a prescribed linear heating rate of  $85,000 [K/s]$  from  $298 - 1830 [K]$ , is predicted as  $y_v^\infty = 0.60$  DAF. The proximate and ultimate analysis of this coal is taken from Rigby [15]. As an example of the effect that the heating rate can have on volatile yields the ultimate DAF volatile yield predicted by proximate analysis is only 43%. The trend predicted by PCCL analysis and the integrated SFOR rate equation fitted to the data by PCCL for the mass fraction yield evolution over time is presented Figure 1.2.

A slightly more sophisticated modeling approach involves representing each volatile species individually. Here a mass of a particular volatile species  $i$ ,  $m_{v,i}$ , can be evolved rather than the entire group of volatiles as above. To incorporate this approach into a simulation the user needs to know the ultimate yield of each species,  $m_{v,i}^0$  as well as the rate constants for each species,  $A_i$  and  $E_i$ . Then Equation 1.1 can be solved for each species and

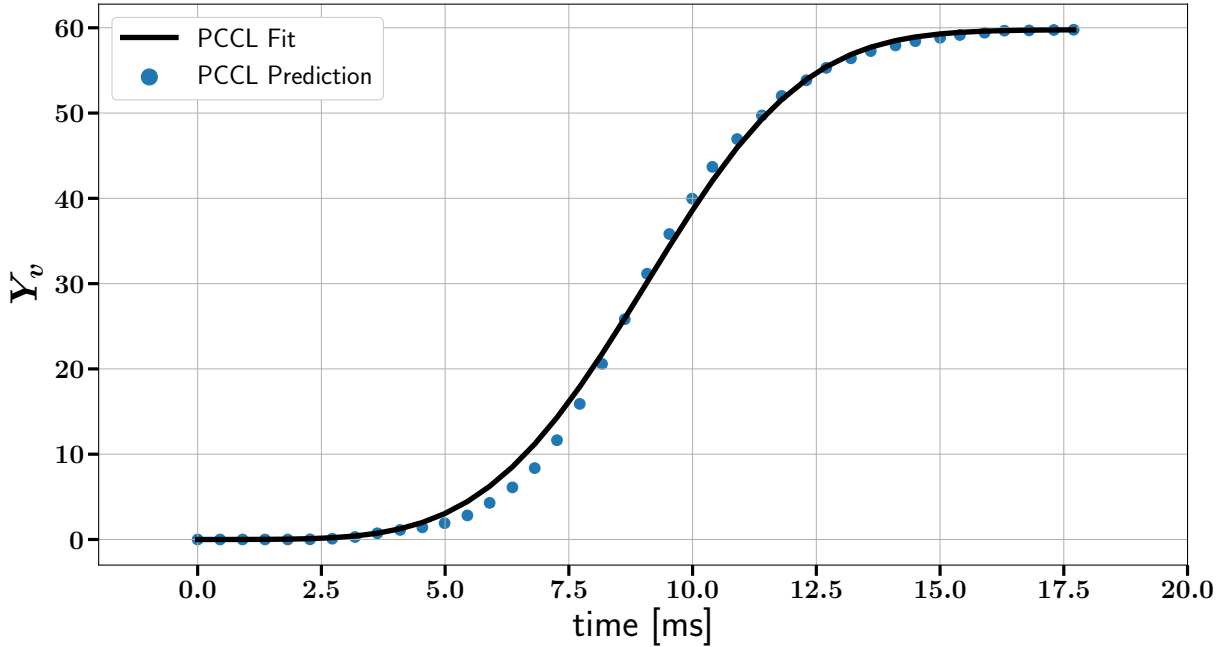


Figure 1.2: PCCL prediction and integrated fitted rate of volatile mass fraction yield ( $y_v$ ) for Utah Hiawatha coal on a DAF basis.

mass fraction yields as in Figure 1.2 can be determined for each species. This approach is referred to as speciated devolatilization.

It has been determined experimentally that the release rates of different volatile species can vary considerably and so speciating these rates in models is advantageous [16]. The speciated models also necessitate a description of the volatile composition. When the volatiles are grouped into a single mass and released at a single rate they can be described very simply, e.g. Smoot et al. [17] assumed that a lumped volatile species could be represented by a single  $C_nH_m$  species that eventually reacted to  $CO$  and  $H_2$ . This approach couples well with simple combustion models sometimes used in CFD simulations that are capable of representing only simple fuels.

These simplifications are unnecessary in the current work as finite rate chemistry is already included in the gas phase CFD simulation and can accurately evolve any volatile species, the light gases at least, in the gas phase following their devolatilization. An account of the devolatilization yields predicted by PCCL for the Utah Hiawatha coal used here

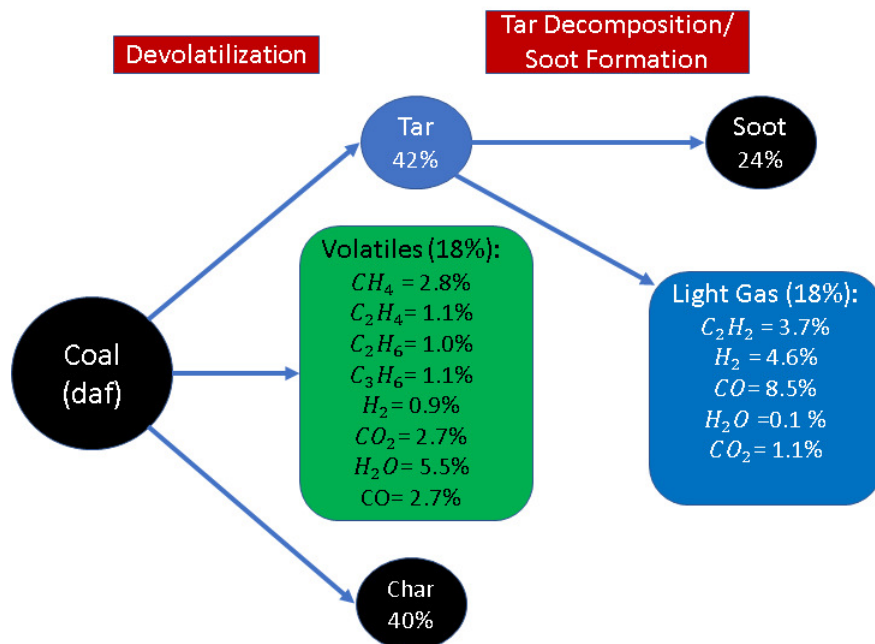


Figure 1.3: Diagram of devolatilization and tar breakdown pathways for Utah Hiawatha coal predicted by PCCL. All percentages are mass fractions of the initial DAF particle mass.

are presented in Figure 1.3. The figure describes the breakdown processes and resultant compositions in a fashion very similar to how they are modeled here. The composition of the primary volatiles is listed in a speciated manner and although separated in the figure tar is considered as an additional primary volatile species.

The very large fraction of the particle mass that is to be released as tar ( $\approx 42\%$  DAF) is of particular importance in soot modeling because tar serves as a precursor for soot formation. As illustrated in Figure 1.3 the tar is decomposed further following its devolatilization. It either breaks down to form more light gases, or joins with other tar molecules to form incipient soot particles.

### 1.2.2 Soot Formation Modeling

Soot formation and consumption is a complex process, highly dependent on chemistry and transport limitations. A good overview of the current understanding of soot formation and modeling of gas phase derived soot is provided by Dasgupta [1] and a more in depth review



is provided by Kennedy [18]. A summary of those reviews is provided here and then the modeling used in this work to describe coal derived soot formation is described.

Soot formation is thought to occur in four phases, nucleation, coagulation, surface growth and agglomeration. All four of these processes are illustrated in Figure 1.4. The process of soot particle nucleation or inception occurs when small hydrocarbon gaseous species combine to form larger polycyclic aromatic hydrocarbons (PAH) molecules. These PAH molecules subsequently combine to form small soot particles. These are the smallest detectable soot particles and generally have a diameter of  $\approx 1\text{[nm]}$  [18].

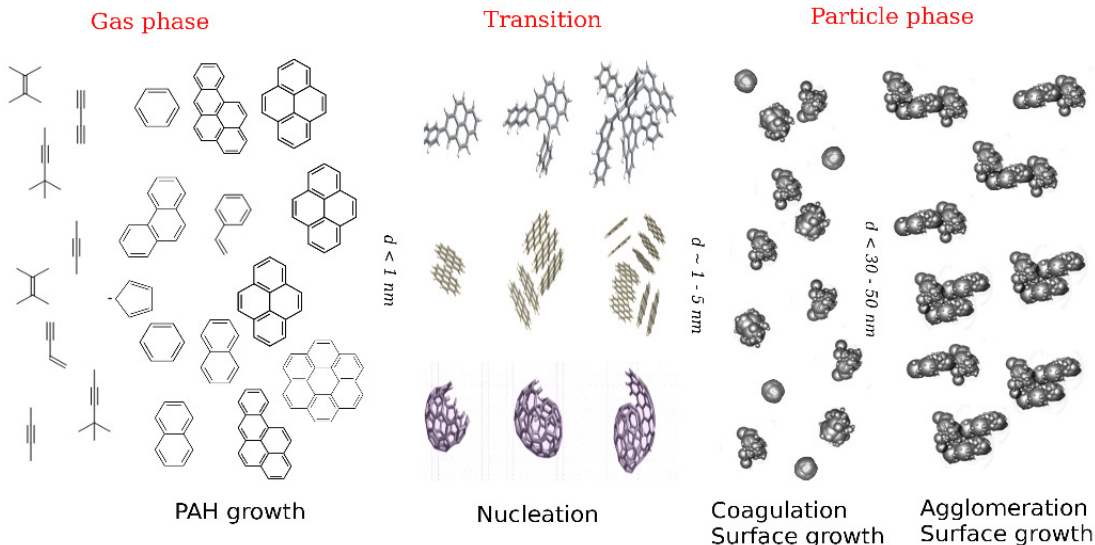


Figure 1.4: Overview of soot formation pathways. Taken from Dasgupta et al. [1].

Coagulation occurs when these small newly formed soot particles bond together after colliding to form larger particles. This process does not consume any soot mass but does decrease the number density of the soot particles as at least two particles are consumed to form a single larger particle. Soot surface growth occurs when gas phase hydrocarbons, primarily acetylene ( $C_2H_2$ ) [1], react with the soot particle surface to add to the mass of the particles. This process has no effect on the number of particles but does increase the total soot mass as the acetylene mass is added to the soot particles.

As the particles grow larger through coagulation and surface growth they retain a roughly spherical shape. Once a threshold size is reached they begin to form large chain-

like structures through combinations of individual particles. This process is referred to as agglomeration.

Models that attempt to describe the process of soot formation are generally described as one of three model classes [1, 18]

1. Empirical Models
2. Semi-Empirical Models
3. Detailed Models

Empirical models are the simplest to implement and often rely on flow variables that are already available in simulations. As they depend on empirical correlations to predict soot growth they need to be applied to problems similar to those for which they are calibrated. However, their simplicity makes them very computationally affordable and therefore an attractive option for incorporation into CFD simulations, particularly in the past.

The empirical model proposed by Calcote and Manos [19] involves a threshold sooting index (TSI) for the prediction of sooting in gas phase flames. The TSI provides a way to simplify the complex chemistry involved in soot formation to rely on a single flow parameter, the critical equivalence ratio  $\phi_c$ , and two calibration constants,  $a$  and  $b$  as

$$TSI = a - b\phi_c. \quad (1.3)$$

The calibration constants are determined from experiments and  $\phi_c$  is the minimum equivalence ratio at which sooting occurs. The TSI represents a measure of the propensity of a particular fuel to soot.

Semi-empirical models attempt to incorporate some more detailed knowledge of soot chemistry while still relying enough on empirical relationships to retain computational tractability. One of the most commonly used semi-empirical soot models is the two equation soot model [20–23]. Here two additional transport equations are solved, one for the soot mass fraction

$$\frac{\partial \rho Y_S}{\partial t} + \frac{\partial \rho U Y_S}{\partial x} = \frac{\partial}{\partial x} \left( \rho D_S \frac{\partial Y_S}{\partial x} \right) + S_{Y_S} \quad (1.4)$$

and one for the soot particle number density

$$\frac{\partial \rho N_S}{\partial t} + \frac{\partial \rho U N_S}{\partial x} = \frac{\partial}{\partial x} \left( \rho D_S \frac{\partial N_S}{\partial x} \right) + S_{N_S}. \quad (1.5)$$

The source terms in both equations,  $S_{Y_S}$  and  $S_{N_S}$ , are dependent on models of the processes discussed above, i.e. nucleation, coagulation, surface growth and agglomeration. These source terms were extended to include soot consumption via oxidation by Kennedy [24]. These semi-empirical methods allow for the soot formation processes to be modeled more accurately than in empirical models but still do not attempt to accurately resolve the complex chemical reactions involved like detailed models do. Another important limitation of this approach is its inability to describe particle size distributions in more detail than a mean diameter and particle number density. This is an important limitation as some of the source terms depend not just on the soot mass fraction but the available surface area.

The most relevant detailed soot model is the Method of Moments with Interpolative Closure (MOMIC) [25]. Here the evolution of soot from gas phase hydrocarbons like  $C_2H_2$  to large PAH molecules is described in detail by chemical mechanisms, e.g. the HACA mechanism. The size distribution of the larger PAH molecules is described by the moments of a particle size distribution. Models are then developed to describe how the surface growth, coagulation, agglomeration and surface consumption processes affect the soot particle size distribution. This approach results in a much richer description of the particle size distribution but is also much more computationally expensive than semi-empirical models. Additionally, they are advantageous in that they are capable of providing a description of tar dynamics and a more detailed description of the chemistry involved.

The research discussed above was only used to predict sooting characteristics in gaseous flames where soot was formed from gas phase hydrocarbons, primarily from acetylene. The progression of modeling flows in which soot is derived from coal particles has followed a similar pathway and repurposes the gas derived soot models. The main difference between the two modeling approaches being that PAH molecules are already available in the form of coal tar that is devolatilized. Therefore, in studies that investigate soot formed from coal the precursor considered is usually tar rather than acetylene.

Some of the earliest attempts in modeling soot derived from coal focused on the role

that soot can play in radiative heat transfer [26]. The goals of these studies was not to have a detailed or mechanistic description of soot formation but rather to develop a method that enabled the efficient determination of local soot volume fraction that could be used to determine radiative effects. The approach assumed that the soot volume fraction was a strong function of the local volatile fuel mass fraction and that a specific fraction, e.g. 10 %, of the carbon from that fuel would produce soot. This type of modeling neglects some of the more nuanced effects of soot formation and destruction that are accounted for in more complex models.

The semi-empirical two equation soot model techniques used for gas derived soot flows were extended by Brown and Fletcher [14] and Ma [2] for use in modeling soot in multiphase coal flows. The commonly accepted pathway for the production of soot in these flows is through the volatile tar which is released from the coal particles. Brown and Fletcher therefore formed transport equations not for just the soot mass fraction and the soot particle number density, as done in previous work, but for the coal derived tar mass fraction as well [14]. As mentioned by Brown and Fletcher, several previous studies have found that the sum of tar and soot mass fractions is very nearly conserved. Furthermore acetylene is not produced in significant amounts by coal devolatilization. This suggests that almost all of the soot formed in coal combustion is derived from tar rather than other likely gas phase hydrocarbon sources. It is therefore common in coal combustion modeling to neglect the relatively low levels of soot formed by nucleation from acetylene and to focus instead on the soot derived from coal tars.

Ma's work was primarily experimental. A flat flame burner was used to entrain coal particles into a laminar methane flame co-flow. The data from this experiment are also used to validate the models developed in this work and a more detailed description of the experimental set up is given in Chapter 5. A one dimensional model of the experimental flow coupled with a system of ordinary differential equations to describe coal particle devolatilization, soot formation and tar cracking was developed by Ma in an attempt to elucidate some of the underlying mechanics of soot formation and consumption. A finite rate chemistry model was used to evolve the chemical species based on an experimental temperature pro-

file. In a one dimensional simulation the soot and tar transport equations referred to above degenerate to a set of ordinary differential equations. Rate equations describing soot formation and agglomeration as well as tar gasification were implemented within the model. The rate parameters for those equations were determined through optimizing the match between experimental and simulation results. Soot and tar oxidation were not considered, likely because of the fuel-rich environment of the co-flow.

Brown and Fletcher’s work utilized the same experimental data from Ma to validate their model, in addition to some other turbulent experiments [14]. Brown and Fletcher extended the simple model used by Ma to a three dimensional framework. A mixture fraction and equilibrium based chemistry modeling approach was taken. The simulations of the flat flame burner again neglected soot oxidation, though a soot oxidation reaction was used in comparison to other experiments, and the rates for soot formation, agglomeration and tar gasification were taken from Ma. An extension of the model developed by Brown and Fletcher is developed in this work and described in Section 4.2.

### 1.3 Thesis Organization

The remainder of this thesis is organized as follows. Chapters 2 and 3 discuss the relevant tools and models implemented in OpenFOAM and used in this work. Chapter 2 introduces the relevant continuous phase modeling framework while Chapter 3 does the same for dispersed solid particle modeling. Many of the models discussed in these two chapters have been modified in this work. Those modified parts of OpenFOAM and any new models that have been implemented are described in Chapter 4.

Chapter 5 describes the settings and boundary conditions for the simulations used to validate the models developed here against experimental results. Chapter 6 presents the results of the validation simulations and compares them to results from both previous computational studies and experiments. A conclusion and suggestions for further work are provided in Chapter 7.

# Chapter 2

## Continuous Phase Modeling in OpenFOAM

### 2.1 Overview

Pulverized coal combustion is a complicated process to model for several reasons. One of the most important complicating features of these flows is their multiphase nature. We make a distinction, in both the theoretical treatment and model implementation, between the solid coal particles and the gaseous continuous phase. The two phases constantly interact and the evolution of one phase has a significant effect on the other. Special considerations are made in this work to capture this interaction in modeling. We follow the framework of modeling both phases in a segregated fashion while coupling them with shared source terms. In this chapter the built-in OpenFOAM implementation of the continuous phase models used in this work are described. Furthermore, where relevant, the theory behind this modeling is discussed in greater detail.

The flow is taken as a low Mach number variable density flow. This is an important distinction from general compressible flows. The density is variable but is not considered to be a function of the Mach number. Rather it depends on the temperature and species composition. The transport equations for mass continuity, momentum, species and sensible enthalpy transport are shown, respectively, below with Einstein's summation notation over

repeated indices adopted.

$$\frac{\partial \rho}{\partial t} + \frac{\partial \rho u_i}{\partial x_i} = S_{p,m} \quad (2.1)$$

$$\frac{\partial \rho u_i}{\partial t} + \frac{\partial \rho u_i u_j}{\partial x_j} = -\frac{\partial P}{\partial x_j} + \rho g_j + \frac{\partial}{\partial x_j} \left[ \rho \nu \left\{ e_{ij} - \frac{2}{3} \left( \frac{\partial u_k}{\partial x_k} \delta_{ij} \right) \right\} \right] + S_{p,u} \quad (2.2)$$

$$\frac{\partial \rho Y_\alpha}{\partial t} + \frac{\partial \rho u_j Y_\alpha}{\partial x_j} - \frac{\partial}{\partial x_i} \left( \rho \alpha \frac{\partial Y_\alpha}{\partial x_i} \right) = S_{p,y} + S_{c,y} \quad (2.3)$$

$$\frac{\partial \rho h}{\partial t} + \frac{\partial \rho u_i h}{\partial x_i} - \frac{\partial P}{\partial t} - \frac{\partial}{\partial x_i} \left( \rho \alpha \frac{\partial h}{\partial x_i} \right) = \rho (u_i g_i) + S_{p,h} + S_{c,h} + S_{r,h} \quad (2.4)$$

In these equations  $u$ ,  $\rho$ ,  $\nu$ ,  $\alpha$  and  $P$  represent the gas phase velocity, density, kinematic viscosity, thermal diffusivity and pressure respectively. In the momentum equation  $g_j$  represents the gravity force vector,  $e_{i,j}$  represents the strain rate tensor and  $\delta_{i,j}$  the Kronecker delta. In the species transport equation  $Y_\alpha$  represents the mass fraction of species  $\alpha$ . The sensible enthalpy is represented as  $h$ .

Each equation has additional source terms, the first index indicates their origin, the second indicates their equation. There are three potential origins for the source terms: the Lagrangian particles, the combustion model, and the radiation model. Each is represented, respectively, by ‘p’, ‘c’ and ‘r’ first indices. The second indices, ‘m’, ‘u’, ‘y’ and ‘h’ indicate that a source term belongs to the mass, momentum, species or enthalpy equation respectively. The particle source terms are discussed further in Chapter 3. The source terms from combustion and radiation are discussed below in this chapter.

The source terms that derive from the interaction with particles can be further decomposed depending on the process they represent. All of the particle derived source terms resulting from particle mass transfer from the dispersed phase to the gas phase are dependent on two distinct processes, devolatilization and evaporation. Additionally two of the equations, momentum and enthalpy, have source terms that result directly from the interaction between particles and the gas phase, regardless of mass transfer. They are the convective heat transfer,  $S_{p,h}^{conv}$  and the reaction to the particle drag force,  $S_{p,u}^{drag}$ . Accordingly each of

these source terms can be decomposed as

$$S_{p,m} = S_{p,m}^{dev} + S_{p,m}^{evap} \quad (2.5)$$

$$S_{p,u} = S_{p,u}^{dev} + S_{p,u}^{evap} + S_{p,u}^{drag} \quad (2.6)$$

$$S_{p,y} = S_{p,y}^{dev} + S_{p,y}^{evap} \quad (2.7)$$

$$S_{p,h} = S_{p,h}^{dev} + S_{p,h}^{evap} + S_{p,h}^{conv} \quad (2.8)$$

The continuous phase transport equations are solved by forming a Poisson pressure equation and using the PISO algorithm, as implemented in OpenFOAM to solve for pressure and velocity fields. A good description of how this pressure-velocity coupling featuring compressibility based thermodynamics is handled in OpenFOAM is provided by Christ [27].

## 2.2 Laminar Combustion Modeling

Only laminar flows are considered in this work. This allows focus to be placed on the processes of interest, i.e. particle devolatilization and volatile chemistry, while circumventing the need to model complex turbulence/chemistry interactions. In light of this restriction the primary combustion modeling used here is relatively simple. We use the built-in laminar combustion model from OpenFOAM.

Chemical reactions represent an important source term in solving species transport Equation 2.3. The non-linearity of the source term necessitates utilizing operator splitting to allow for solution of the discretized transport equations as a linear system of equations. As an example of how the specie transport equation is solved a one dimensional example is given here for cell C on the mesh pictured in Figure 2.1. This example will illustrate why the chemical reaction source term can not be readily included in the normal solution of the species transport equation and an explicit calculation of the source term is used instead. The formulation and treatment of that source term used in the current work is then discussed.

The finite volume method first integrates the differential equation of interest, in this case the species transport Equation 2.3, over the control volume, here just the one dimensional line. Then the Gauss divergence theorem is applied to transform the volume integrals into



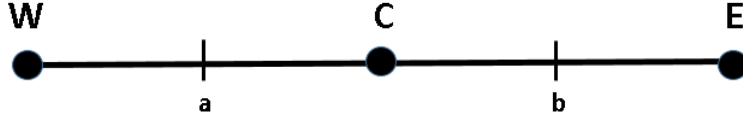


Figure 2.1: One dimensional mesh composed of three cells, W,C and E. The faces between the two cells are named a and b.

a surface integrals of fluxes. This leads to the following form of the equation for the one dimensional case where the divergence theorem is equivalent to the fundamental theorem of calculus and the volume integrals of the source term and time derivative are approximated

$$\Delta x \cdot \frac{\partial \rho Y}{\partial t} = -(\rho_b U_b Y_b - \rho_a U_a Y_a) + \left( \rho_b \nu_b \frac{\partial Y}{\partial x} |_b - \rho_a \nu_a \frac{\partial Y}{\partial x} |_a \right) + \Delta x \cdot S_r(\mathbf{Y}, T). \quad (2.9)$$

Here  $S_r$  is the chemical reaction source term that depends on the species concentrations  $\mathbf{Y}$  and temperature  $T$ .  $\Delta x$  is the spacing between adjacent cell centers. In general, the chemical source term of one species depends on many other species and thus the bold face symbol is used to refer to the vector of species mass fractions. The subscripted field variables indicate the evaluation of that field at the cell or face location the subscript corresponds to in Figure 2.1, e.g.  $\rho_a$  is the density evaluated at the face between cells W and C. In the finite volume method the values are stored at the cell centers so those values, at least from the current time step, are available and the face values must be determined from the cell center values. The field values at the faces are determined from simply averaging the cell center values since the spacing is assumed constants here, e.g.

$$Y_a = \frac{Y_W + Y_C}{2}. \quad (2.10)$$

Similarly the spatial derivative at the face can be determined with a finite difference

$$\frac{\partial Y}{\partial x} |_b = \frac{Y_E - Y_C}{\Delta x} \quad (2.11)$$

Then rewriting Equation 2.9, substituting the values of  $Y$  at the face for the known values

at the cell centers yields

$$\begin{aligned} \frac{\partial \rho Y_C}{\partial t} = \frac{1}{\Delta x} \left[ \left( \rho_a U_a \cdot \frac{Y_C + Y_W}{2} - \rho_b U_b \cdot \frac{Y_E + Y_C}{2} \right) + \left( \rho_b \nu_b \frac{Y_E - Y_C}{\Delta x} - \rho_a \nu_a \frac{Y_C - Y_W}{\Delta x} \right) \right] \\ + S_r(\mathbf{Y}_C, T). \end{aligned} \quad (2.12)$$

The next step is to form a linear equation to solve for  $Y_C$ . This is in general difficult because  $\rho$  and  $U$  vary in time and space just as  $Y$  does and so should be solved in a coupled fashion along with  $Y$ . A common technique used to simplify the solution is to segregate the solutions of the various transport equations. In this case that means that we take  $\rho$  and  $U$  as constants, having already been determined by the solution of their corresponding transport equations. Then they can be incorporated into constant coefficients which multiply the variable of interest,  $Y$ , in a linear equation. This approach is taken in OpenFOAM. Grouping the constants together yields

$$\begin{aligned} \frac{\partial \rho Y}{\partial t} = \frac{1}{\Delta x} \left( \frac{\rho_a U_a - \rho_b U_b}{2\Delta x} - \frac{\rho_a \nu_a + \rho_b \nu_b}{\Delta x^2} \right) \cdot Y_C + \\ \left( \frac{\rho_a U_a}{2\Delta x} + \frac{\rho_a \nu_a}{\Delta x^2} \right) \cdot Y_W + \left( \frac{-\rho_b U_b}{2\Delta x} + \frac{\rho_b \nu_b}{\Delta x^2} \right) \cdot Y_E + S_r(\mathbf{Y}_C, T). \end{aligned} \quad (2.13)$$

For numerical stability implicit time discretization methods are typically employed, using the simple Euler implicit time discretization leads to

$$(\rho_C - C_C) \cdot Y_C^{n+1} - C_W \cdot Y_W^{n+1} - C_E \cdot Y_E^{n+1} = \rho_C Y_C^n + \Delta t \cdot S_r(\mathbf{Y}_C^{n+1}, T^{n+1}) \quad (2.14)$$

where  $Y_C^{n+1}$  is the unknown mass fraction in cell  $C$  at the new time step  $\Delta t$  and  $Y_C^n$  is the current cell mass fraction value which is known. The constants are defined as

$$C_C = \Delta t \cdot \left( \frac{\rho_a U_a - \rho_b U_b}{2\Delta x} - \frac{\rho_a \nu_a + \rho_b \nu_b}{\Delta x^2} \right) \quad (2.15)$$

$$C_W = \Delta t \cdot \left( \frac{\rho_a U_a}{2\Delta x} + \frac{\rho_a \nu_a}{\Delta x^2} \right) \quad (2.16)$$

$$C_E = \Delta t \cdot \left( \frac{-\rho_b U_b}{2\Delta x} + \frac{\rho_b \nu_b}{\Delta x^2} \right). \quad (2.17)$$

With the exception of  $S_r$  this is a linear equation that describes the mass fraction in cell  $C$  at the next time step,  $Y_C^{n+1}$ , depending on the unknown neighbor mass fraction values

at the next time step,  $Y_W^{n+1}$  and  $Y_E^{n+1}$ . Disregarding  $S_r$ , similar equations could be formed for each cell in the domain which, when combined, would form a solvable linear system to advance the mass fractions in time. However, the chemical source term depends non-linearly on  $\mathbf{Y}_C^{n+1}$  and  $T^{n+1}$ . Therefore, the discretization process would result in a large system of coupled non-linear equations (number of equations equal to number of control volumes  $N_V$ ). Moreover, since the chemical source term for one species mass fraction can depend on the mass fractions of all other species we would have to solve a system of  $N_V \cdot (N_{species} + 1)$  non-linear equations at each time step e.g. using Newton's method. This is computationally too expensive and a different approach is utilized in which the chemical source term is calculated first without any consideration of advection or diffusion and then added back into the discretized equations as a constant source term.

To calculate the reaction source term, the laminar combustion model makes use of the mesh discretization used by the main CFD solvers to evaluate the chemical reactions. It treats each of these cells as a perfectly stirred reactor (PSR). This type of reactor effectively assumes that there are no spatial variations within a computational cell and neglects any species or heat transfer limitations within reactor. The contents of each of these reactors is evolved over the time step  $\Delta t$ . The evolution of the reactor contents provides source terms for both the species and enthalpy transport equations.

A combustion mechanism that is distinct from the CFD combustion model is also needed to perform calculations. A combustion mechanism contains two important pieces of information. First it provides the thermodynamic data for each reactive species considered that is needed in the combustion calculations. Secondly it provides a list of the relevant reactions for those species and the necessary information for their kinetics. Here we utilize a well known C-2 mechanism, the DRM-22 [28] which is provided in Appendix A.

There are several ways to evolve the state of a PSR. The simplest method, that has been often employed in other multiphase pulverized coal simulations, is to assume that the time scale of the chemical reactions is much smaller than those of advection and diffusion and thus chemical equilibrium can be assumed. Given the thermo-chemical state of the contents of a PSR the equilibrium state of the mixture can be calculated efficiently [29].

Unfortunately, the chemical equilibrium assumption is locally often violated e.g. when rapid devolatilization forms regions that are very fuel rich. In these fuel rich regions the timescales associated with chemical reactions become so large that they can become comparable to those of advection and diffusion. In these situations chemical reactions may not proceed to a state near equilibrium.

An alternative approach, which is adopted here, is to use a finite rate combustion mechanism that is capable of capturing the reaction kinetics. The individual chemical reactions are modeled as ordinary differential equations (ODEs). Their rates depend on the temperature and species concentrations of the mixture within the PSR. The combination of these ODEs forms a stiff system of coupled ODEs that need to be solved together. A stiff system of ODEs is one which features rapid changes in variables, here species concentrations, such that computational solutions with traditional solvers require prohibitively small time steps. Stiff equation solvers have been developed to enable the solution of systems like these. OpenFOAM offers a number of general ODE integrators in addition to a solver that has been specifically developed for the integration of reacting chemical systems like these called the `EulerImplicit` solver. In this work we use the `SeuLex` stiff ODE solver [30], as implemented in OpenFOAM to integrate the reaction rates and advance the chemical state.

As an example of how the system of ODEs can be formulated for a reactive species a brief overview of that formation is shown here for  $CH_4$ . First consider a single reaction and its corresponding rate equation containing  $CH_4$  from the DRM-22 mechanism



Which has the associated forward rate law

$$r = [H][CH_4] \left( A \cdot \exp \frac{-E}{RT} \right). \quad (2.19)$$

The constants,  $A$  and  $E$ , for this reaction are specified in the combustion mechanism and the square brackets represent a molar concentration of the species which are calculated from the known species mass fractions within the cell or PSR.  $R$  and  $T$  are the universal gas constant and the local gas temperature respectively. This rate,  $r$ , indicates how quickly the reaction will proceed.

In general this reaction rate can be used to determine the production and consumption rates of the species involved in the reaction through multiplication with the corresponding stoichiometric coefficient, e.g.  $r_{p,\alpha} = \nu_\alpha \cdot r$  where  $r_{p,\alpha}$  is the production rate of product species  $\alpha$  which has stoichiometric coefficient  $\nu_\alpha$ . Similarly, for reactant species a rate of consumption is determined as  $r_{r,\alpha} = \nu_\alpha \cdot r$ . For example if we only consider the effect of this reaction, since  $CH_4$  has a unity stoichiometric coefficient and is a reactant in Equation 2.18  $\Rightarrow \nu_{CH_4} = 1$ , its consumption rate is simply  $r_{r,CH_4} = r [kmol/(m^3s)]$ .

There are many reactions, dozens in the DRM-22 mechanism, that feature  $CH_4$  as either a reactant, as in Equation 2.18, or a product. Since the evaluation of the combustion model is segregated from the species transport equations, the production and consumption rates of a every reaction,  $i$ , featuring  $CH_4$ ,  $r_{p,i}$  and  $r_{r,i}$  respectively, can be calculated explicitly using the last known values of species concentrations and local temperature. Then an ODE for the concentration of  $CH_4$  can be formulated as

$$\frac{d[CH_4]}{dt} = \sum_i^{np} (r_{p,i}) - \sum_i^{nr} (r_{r,i}). \quad (2.20)$$

Where  $np$  and  $nr$  are the total number of reactions containing  $CH_4$  as a product and a reactant respectively. An analogous ODE can be formed for the concentration of all reactive species, forming a system of coupled ODEs. The coupling is effected through the dependence of the rate laws on other species concentrations, e.g. Equation 2.19 depends not just on  $[CH_4]$  but on  $[H]$  as well.

As mentioned above this coupled system of equations is solved over the time step  $\Delta t$  for each computational cell using the Seulex stiff ODE integrator [30] that is incorporated into OpenFOAM . It is important to note that the Seulex ODE integrator typically splits the overall fluid time step  $\Delta t$  into many smaller time steps to more accurately capture the fast chemical kinetics.

Once these calculations are complete the source terms for the species and sensible enthalpy transport equations can be formed. The source term for the species  $\alpha$  transport equation,  $S_{c,y,\alpha}$ , is formed from comparing the mass fraction of species  $\alpha$  in every cell before

and after its chemical evolution, respectively  $Y_{CH_4}^0$  and  $Y_{CH_4}^1$  as

$$S_{c,y,\alpha} = \frac{Y_{\alpha}^1 - Y_{\alpha}^0}{\Delta t} \cdot \rho \quad (2.21)$$

The sensible enthalpy source term is calculated for a particular cell by summing over the enthalpy of combustion for all species, given by

$$S_{c,h} = \sum_{\alpha} -h_{f,\alpha} \cdot S_{c,y,\alpha}. \quad (2.22)$$

## 2.3 Radiation Modeling

The Radiative Transfer Equation (RTE) for a gray absorbing, emitting and scattering medium consisting of gas, soot and coal particles [31–33] at position  $\vec{x}$  and along direction  $\vec{s}$  is given by

$$\begin{aligned} \frac{dI(\vec{x}, \vec{s})}{ds} = & -(a_{gs} + a_p + \sigma_p) I(\vec{x}, \vec{s}) + a_{gs} \frac{\sigma T^4}{\pi} + \frac{E_p(\vec{x})}{\pi} \\ & + \frac{\sigma_p}{4\pi} \int_0^{4\pi} I(\vec{x}, \vec{s}') \phi(\vec{s}', \vec{s}) d\Omega, \end{aligned} \quad (2.23)$$

where  $I(\vec{x}, \vec{s})$  is the radiative intensity,  $\phi(\vec{s}', \vec{s})$  is the scattering phase function,  $T$  is the local gas temperature and  $\sigma = 5.67e^{-8} [W/(m^2 K^4)]$  is the Stefan Boltzmann constant. This equation describes the rate of change of the radiation intensity at position  $\vec{x}$  for a differential path length  $ds$  along the direction  $\vec{s}$ . The first term on the right hand side is the absorption of the thermal radiation by the gas, soot and coal particle mixture. The second and third terms describe emission from the gas/soot mixture and the coal particles respectively. The fourth term is the scattering contribution from the coal particles (isotropic scattering). Here, it has been assumed that the gas and the soot are in thermal equilibrium and  $a_{gs} = a_g + a_s$  is the combined absorption coefficient from gas and soot. The emission contribution of the hot coal particles  $E_p(\vec{x})$ , the coal particle absorption coefficient and the particle scattering coefficient,  $\sigma_p$ , are given in Section 3.5.

In this work the P1 radiation model is used to approximately solve the RTE. The P1 radiation model is the lowest order case when using spherical harmonics to transform the

integro-differential RTE into a set of coupled partial differential equations [32]. The P1 model relies on solving for the incident radiation intensity  $G$

$$\nabla \cdot \frac{1}{3a + \sigma_{eff}} \nabla G - aG = -4a_{gs}\sigma T^4 - 4E_p, \quad (2.24)$$

where we introduced the overall absorption coefficient of the gas/soot and particle mixture  $a = a_{gs} + a_p = a_g + a_s + a_p$ . The OpenFOAM implementation of the P1 model is used unmodified but the absorption/emission model has been modified to include the effects of soot.

The effect of the thermal radiation heat exchange on the gas phase in the simulation is represented by a source term in the gas phase enthalpy equation  $S_{r,h}$ .

$$S_{r,h} = a_{gs}G - 4a_{gs}\sigma T^4. \quad (2.25)$$

### 2.3.1 Absorption Models

In order to evaluate Equations 2.24 and 2.25 the absorption coefficients for gas, soot and coal particles must first be determined. They depend on the gas phase properties but are also dependent on the Lagrangian phase particles. OpenFOAM provides the `BinaryAbsorptionEmission` model class to accommodate the calculation of the coefficients in multiphase flows by allowing the user to select an absorption model for two phases, here one for the gas phase and one for the particle phase. The coefficients calculated in each of the two models are summed to provide an overall absorption and emission coefficient. An extension of this model to accommodate the radiative effect of soot, which, due to other modeling constraints is not captured in this approach, is detailed in Chapter 4. The dispersed phase absorption coefficient contributions are discussed in section 3.5.

The built-in `greyMeanAbsorptionEmission` model is used to determine the gas phase contribution for every specie except soot. The model allows users to select up to five gas phase species most relevant to radiative heat transfer that are then used to calculate an absorption coefficient in each cell. For each computational cell the model iterates through each of the selected species. First the species mole fraction,  $X_i$ , is determined and used to find the partial pressure of the species  $\alpha$  as  $P_\alpha = X_\alpha \cdot P$ . The species mole fraction is

assumed to be equal to the species volume fraction,  $f_\alpha$ , since the gas is considered ideal, i.e.  $X_\alpha = f_\alpha$ . The volume fraction can be calculated based on the species mass fractions,  $Y_\gamma$ , and the species densities,  $\rho_\gamma$ , which are determined with the ideal gas law at the local temperature and pressure, as

$$f_\alpha = \left( \frac{Y_\alpha}{\rho_\alpha} \right) / \sum_\gamma \left( \frac{Y_\gamma}{\rho_\gamma} \right) \quad (2.26)$$

where the sum is over all species in the local mixture. The model then assumes that the species absorption coefficient contribution,  $a_\alpha$ , can be described as a function of the partial pressure and a polynomial of either the local temperature itself or its inverse, indicated with the plus/minus symbol in the exponents, as

$$a_\alpha = P_\alpha \cdot (b_0 + b_1 T^{\pm 1} + b_2 T^{\pm 2} + b_3 T^{\pm 3} + b_4 T^{\pm 4} + b_5 T^{\pm 5}). \quad (2.27)$$

The polynomial coefficients,  $b_i$ , are determined from fits to experimental data and must be provided by the user for each species and two different sets can be specified: one to be used in high temperature evaluations and the other for low temperatures. The temperature thresholds for determining these ranges are also specified by the user in an input dictionary.

Generally there will be more than one species considered and so the individual species absorption coefficient contributions,  $a_\alpha$ , will be summed to produce an overall gas phase contribution  $a_g$ .



# Chapter 3

## Dispersed Phase Modeling in OpenFOAM

### 3.1 Overview

OpenFOAM provides a framework for not only Lagrangian parcel injection and tracking but mass, species, enthalpy and momentum transfer between those parcels and the continuous gas phase. For all of the work in this thesis the OpenFOAM parcel class `ReactingMultiphaseParcel` and parcel cloud class `ReactingMultiphaseCloud` were utilized as base classes. In this Chapter an overview of the built-in OpenFOAM Lagrangian particle modeling is presented, the models and modifications implemented in this work are detailed in Chapter 4.

In OpenFOAM a Lagrangian framework is used to model the dispersed phase, in contrast to the Eulerian framework used to model the continuous phase fields described in Chapter 2. The basic approach is to track individual particles instead of assuming a continuum. Tracking individual physical particles, particularly in large simulations where there can easily be hundreds of billions of particles quickly becomes too computationally expensive. OpenFOAM utilizes computational objects called parcels to decrease this burden. A parcel is a computational representation of multiple physical particles.

In turn, an additional object oriented abstraction is made and these parcels are collected

by a cloud object, here of the class `ReactingMultiphaseCloud` or its derivatives. All of the parcels in the simulations performed here belong to a single cloud instantiation named `coalCloud`. The cloud object then contains information on all of the individual parcels as well as the information that doesn't vary between parcels, e.g. their initial composition, temperature and velocity.

Parcels can represent as many physical particles as desired by the user but each of the particles within a parcel must be of the same diameter and type. The user specifies how many particles should be represented by a parcel and that selection is stored in the parcel class variable `n_p`. This variable is used frequently in calculating source terms, e.g. the parcel mass loss over a time step can be calculated as though for a single particle, that particle mass loss is then multiplied by `n_p` to determine the total mass loss of the parcel. Throughout the rest of this and following chapters the term particle will reference a single physical particle, specifically a single pulverized coal particle, and parcel will refer to the computational object that collects particles.

When discussing the formation of source terms and evaluation of mass loss processes we will often describe only single particles. This makes the theoretical discussions simpler. Instead of describing the processes for a parcel and then multiplying the results, e.g. mass loss, by `n_p` we just describe the process for a single particle and sum over all relevant particles.

OpenFOAM evolves the parcels in a fashion very similar to that which would be used for single particles. Differential equations are solved at each main gas phase timestep for each parcel to determine its properties, e.g. its velocity, temperature and mass. There are often terms in these equations that depend on the environment surrounding the particle. These terms are determined from the concomitant continuous phase solution that evolves the gas surrounding the particles, e.g. to calculate a convection heat transfer term in the particle temperature equation the gas temperature, velocity and other properties surrounding the particle must be known. Likewise the parcels affect the solution of the gas phase through the particle source terms in the gas phase equations described in Section 2.1. Since the continuous phase equations are solved using the finite volume method on a discretized mesh

a convenient way to include the particle sources is to sum all of the particle sources within a particular cell and add that sum to the cell's source term. A visual representation of the interaction of particles with the computational mesh is provided in Figure 3.1.

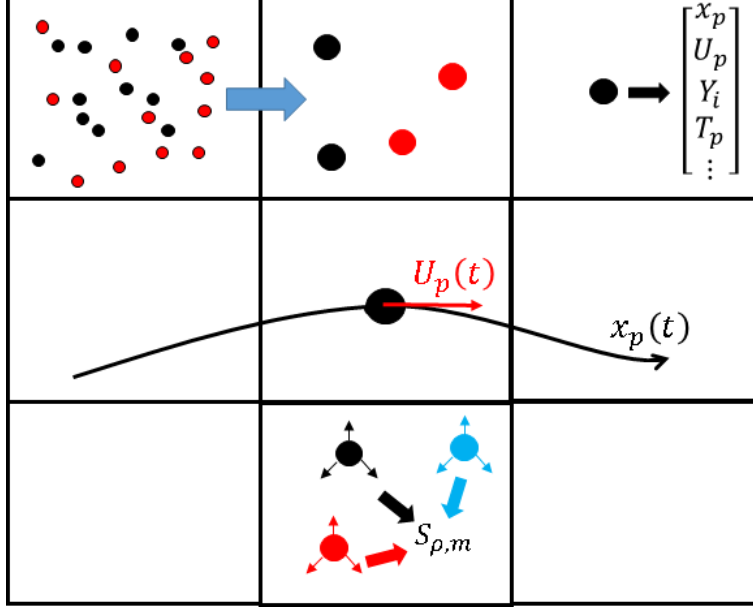


Figure 3.1: A representation of various parcel properties within a two dimensional mesh. In the two leftmost cells of the top row the representation of two different diameter coal particles (distinguished by color) by parcels is illustrated. On the middle row of cells the trajectory of a parcel  $x_p(t)$  through several cells is represented by a black line. The instantaneous parcel velocity  $U_p(t)$  is represented by the attached red arrow. In the bottom center cell the contributions of three parcels to the density transport equation source term is depicted.

For example, a simplified version of the formulation of the mass source term due to parcel devolatilization in the continuity equation 2.1 is developed here (a much more thorough treatment on this process is available in Section 3.3). We will consider the single linear discretized equation for a cell,  $C$ , in isolation from the entire system formed by the finite volume method discretization of the continuity equation. It will have the form

$$a_C \rho_C + \sum_{i=1}^6 a_i \rho_i = S_C. \quad (3.1)$$

Here  $a_C$  and  $a_i$  are the constant coefficients of the cell  $C$  and its 6 neighbor cells respectively, assuming a structured three dimensional mesh.  $\rho_C$  is the gas phase fluid density in cell  $C$

which is being solved for and  $\rho_i$  are the densities of the neighboring cells. The sum is over all 6 neighbor cells and  $S_C$  is the constant source term. In single phase flows there is no source of mass and  $S_C = 0$ , here we consider a multiphase flow and the gases released from particles are subsumed into the gas phase, therefore a non-zero mass source is possible here. Considering only the particle devolatilization mass source the source term can be determined as

$$S_C = \frac{\sum_i^{\text{parcels}} (dm_{i,\text{vol}})}{V_C \cdot dt}. \quad (3.2)$$

Where  $dm_{i,\text{vol}}$  is the mass loss of a single parcel due to devolatilization over the relevant timestep  $dt$ , i.e. that which is used to formulate the finite volume equation, and  $V_C$  is the cell volume. The sum is taken over all of the parcels within the cell C. This parcel mass loss is calculated with an Arrhenius rate equation depending on the volatile availability within the parcel as well as the parcel temperature. The rate equation can be given as

$$\frac{dm_v}{dt} = -A \cdot \exp\left(\frac{-E}{RT_p}\right) \cdot m_v \quad (3.3)$$

where again  $m_v$  is the volatile mass remaining within the parcel. This equation is integrated over the same timestep,  $dt$ , mentioned above to determine the devolatilization mass loss of a single particle,  $dm_p$ . The total parcel mass loss for parcel  $i$  in Equation 3.2 is then determined as  $dm_{i,\text{vol}} = n_p \cdot dm_p$ , where  $n_p$  is the number of particles represented by this parcel, i.e. `n_p`.

A central focus of this work is placed on devolatilization and other inter-phase transfer processes. The framework used to describe the internal multiphase composition of a parcel in `ReactingMultiphaseParcel` is now described and will be used throughout the rest of this thesis in describing models. Physical coal particles are porous solid particles and depending on the pre-treatment they often contain some mass percentage of liquid water. As they are heated in a reactor they undergo the processes of evaporation, devolatilization and surface reaction. All three of these transfer mass from the particle to the carrier gas and all three, particularly devolatilization and surface reactions, are dependent on the geometry of the particle and complex coal chemistry reactions that breakdown the solid structure of the coal to release gases.

This level of detail is not utilized in OpenFOAM multiphase particle/parcel modeling. Instead, the fraction of the particle mass that is to be lost to a certain phase exchange

process, e.g. devolatilization, is specified at the beginning of the simulation by the user. The primary delineation is of the phases contained within the particle themselves. Three particle phase mass fractions must be specified by the user.

1.  $Y_{p,gas}$ : The mass fraction of the particle that can eventually be released through devolatilization.
2.  $Y_{p,solid}$ : The particle mass fraction that contains solid carbon (char) and ash. The char mass can be consumed by surface reactions but the ash mass remains with the particle throughout its lifetime.
3.  $Y_{p,liquid}$ : The particle mass fraction that can be released through evaporation. Here this entire fraction is composed of water.

These three phase fractions sum to one. Each of these phase mass fractions can be further decomposed to describe the species that compose them. As mentioned earlier, the solid fraction is composed of char and ash. Because the total solid phase fraction is already stored in  $Y_{p,solid}$  these species fractions are user specified as fractions within the solid fraction, i.e.  $Y_{p,char}^{solid}$  and  $Y_{p,ash}^{solid}$  where  $Y_{p,char}^{solid} + Y_{p,ash}^{solid} = 1.0$ . The ratio of char to ash needs to be determined either from experiments or coal analysis software like Chemical Percolation Devolatilization (CPD) [11] or P.C. Coal Lab (PCCL) [12]. The liquid fraction can be decomposed similarly but the only liquid present in these simulations is water so  $Y_{p,H_2O}^{liquid} = 1.0$ .

The decomposition of the gas phase fraction is often much more complex. The gas phase fraction itself, as well as its species composition, are dependent on a variety of factors including the coal type and the heating environment. Again these fractions can be determined from experiment or by using coal chemistry analysis software. Regardless of the method used to determine them the volatile species mass fractions are specified by the user in terms of their fraction within the total gas phase fraction, just as is done for the solid and liquid fractions so that  $\sum_i Y_{p,i}^{gas} = 1.0$ . An example of the composition for the Utah Hiawatha coal used in this work from C3M/CPD is presented in Figure 3.2.

The equations for parcel velocity, temperature and mass are described in Section 3.2 below. These equations are solved and used to update the properties of the parcel prior

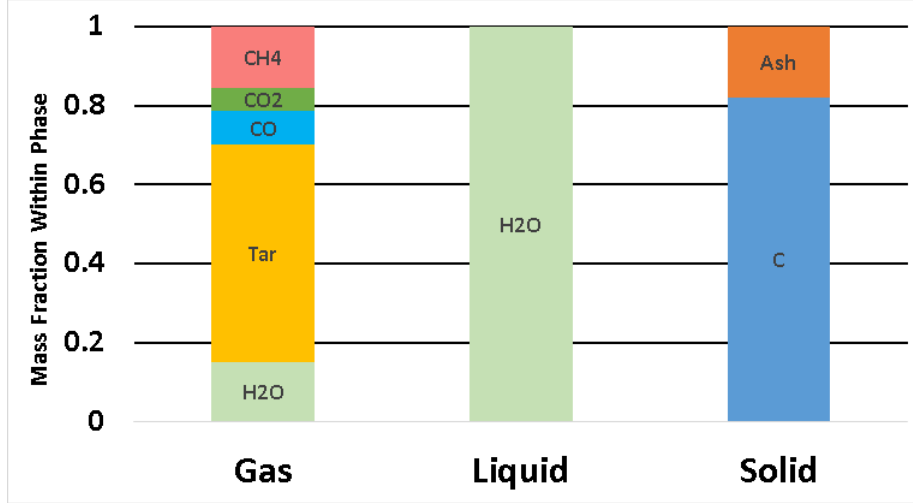


Figure 3.2: Species mass fraction breakdown within each phase of Utah Hiawatha coal predicted by C3M/CPD on an as received basis.

to every continuous phase time step. These three equations, in turn, depend on source terms that are calculated in separate submodels. In this work three parcel submodels are used, devolatilization, evaporation and radiation. These submodels are described in detail in Sections 3.3 - 3.5 respectively. Surface reactions are neglected here as they occur downstream of the processes of the greatest interest, devolatilization and soot formation. The source terms to continuous phase equations that depend on these mass transfer processes are discussed within each corresponding section. The continuous phase source terms that are not mass transfer based, the convective enthalpy source and the drag reaction momentum source, are described in Section 3.6.

The overall solution algorithm, i.e. the segregated solution for both dispersed and continuous phase, proceeds as follows at each simulation time step:

1. Each of the parcel submodels are evaluated to provide transfer source terms between the dispersed and continuous phase. These evaluations are based on the previous time step solution for both gas phase and dispersed phase properties.
2. The three parcel equations from Section 3.2 are solved with the newly formed parcel source terms and used to update the parcel properties. Further continuous phase source

terms are calculated as a result of the integration of the parcel equations.

3. The continuous phase transport equations described in Chapter 2 are solved relying on the sources determined by the parcel submodels as well as the updated parcel properties.

## 3.2 Particle Velocity, Temperature and Mass Conservation Equations

### 3.2.1 Particle Velocity Equation

Each particle is tracked through the flow field with velocity  $\mathbf{U}_p$  determined by Newton's second law

$$m_p \cdot \frac{d\mathbf{U}_p}{dt} = \mathbf{F}_{\text{drag}} + \mathbf{F}_{\text{gravity}}. \quad (3.4)$$

Where the gravity force is calculated as

$$\mathbf{F}_{\text{gravity}} = m_p \cdot \mathbf{g}, \quad (3.5)$$

with particle mass  $m_p$  and the force of gravity vector,  $\mathbf{g}$ .

A spherical drag approximation is used to model the drag force as

$$\mathbf{F}_{\text{drag}} = \mathbf{U}_{diff} \cdot \frac{0.75 \cdot m_p \cdot \mu_c \cdot C_d}{\rho D_p^2} \quad (3.6)$$

where is defined as  $\mathbf{U}_{diff} = \mathbf{U} - \mathbf{U}_p$  for local gas velocity  $\mathbf{U}$ . Here the drag coefficient,  $C_d$ , is a function of the particle surface Reynolds number, defined as

$$Re_s = \frac{\rho_s \cdot \|\mathbf{U}_{diff}\| \cdot D_p}{\mu_s} \quad (3.7)$$

The subscript 's' on  $\mu_s$  and  $\rho_s$  indicate these properties are evaluated at the particle surface. In OpenFOAM these surface properties are approximated using the "two thirds rule" to determine the particle surface temperature and then assuming linear property variations with temperature within small temperature ranges. For example the particle surface density  $\rho_s$  is calculated as follows where  $\rho_c$  is the gas phase density interpolated to the particle

position, while  $T_p$ ,  $T_s$  and  $T_c$  are, respectively the particle, particle surface and interpolated gas phase temperatures.

First  $T_s$  and  $T_{ratio}$  are determined using the “two thirds rule”.

$$T_s = \frac{2T_p + T_c}{3}; \quad T_{ratio} = \frac{T_c}{T_s} \quad (3.8)$$

then  $\rho_s$  can be determined

$$\Rightarrow \rho_s = \rho_c \cdot T_{ratio}. \quad (3.9)$$

$\mu_s$  is calculated similarly but with the inverse of  $T_{ratio}$

$$\mu_s = \frac{\mu_p}{T_{ratio}} \quad (3.10)$$

With  $Re_s$  known,  $C_d$  is then determined

$$C_d = \begin{cases} 0.424(Re_s) & Re_s > 1000 \\ 24 \cdot \left(1 + 6 \cdot Re_s^{-\frac{2}{3}}\right) & Re_s \leq 1000. \end{cases}$$

### 3.2.2 Particle Temperature Equation

The particles considered in this work are sufficiently small that the temperature of a particle is assumed to be uniform. Its evolution is determined by

$$m_p c_{p,p} \frac{d(T_p)}{dt} = \dot{h}_p^{dev} + \dot{h}_p^{evap} + \dot{h}_p^{rad} + \dot{h}_p^{conv} \quad (3.11)$$

Here,  $c_{p,p}$  is the coal's specific heat capacity, it is determined from the thermodynamic properties of the constituents in the particle, scaled by their mass fractions, as well as the current particle temperature. The enthalpy source terms that are dependent on coal particle submodels,  $\dot{h}_p^{dev}$  and  $\dot{h}_p^{evap}$  are detailed in their respective subsections 3.3.1 and 3.4.

The third source term in Equation 3.11,  $\dot{h}_p^{rad}$  is the particle radiation enthalpy source and is determined as

$$\dot{h}_p^{rad} = A_s \cdot a_p \left( \frac{G_p}{4} - \sigma T_p^4 \right).$$



Here  $G_p$  is the incident radiation interpolated to the particle position,  $A_s$  the surface area of the spherical coal particle and the other variables are consistent with their definition in Section 3.5.

The final term in Equation 3.11,

$$\dot{h}_p^{conv} = h (T_c - T_p) \cdot A_s$$

represents the convective heat transfer from the gas phase to the particle. Here  $A_s$  is the particle surface area and the heat transfer coefficient,  $h$ , is determined from the particle Nusselt number,  $Nu_p$ , as

$$h = \frac{\kappa_s \cdot Nu_p}{D_p}. \quad (3.12)$$

Where  $\kappa_s$  is the thermal conductivity evaluated at the particle surface temperature, it is calculated just as  $\mu_s$  above.  $D_p$  is the coal particle diameter. The particle Nusselt number is determined from the Ranz-Marshall correlation [34,35] as

$$Nu_p = 2.0 + 0.6 \sqrt{Re_s} \sqrt[3]{Pr_s} \quad (3.13)$$

where  $Pr_s$  is the Prandtl number determined from the surface values of viscosity and thermal diffusivity, as well as the fluid specific heat capacity,  $c_p$ , interpolated to the particle location

$$Pr_s = \frac{c_p \mu_s}{\kappa_s}$$

and  $Re_s$  is the particle surface Reynolds number of the particle as discussed above.

### 3.2.3 Particle Mass Equation

Equation 3.14, governs the evolution of the particle mass

$$\frac{dm_p}{dt} = \dot{m}_p^{dev} + \dot{m}_p^{evap}. \quad (3.14)$$

The relevant mass transfer source terms are devolatilization,  $\dot{m}_p^{dev}$ , and liquid evaporation  $\dot{m}_p^{evap}$ . The calculation of these mass source terms is discussed in Sections 3.3 and 3.4 respectively.

### 3.2.4 Integration of Particle Equations

All three of the equations are evaluated with frozen coefficients at each time step. The submodel source terms are evaluated prior to the integration of the particle equations and those sources are considered constant. With the coefficients frozen, all three of the particle evolution equations can be cast into a linear, first order ordinary differential equation (ode) form

$$\frac{d\phi}{dt} = -\beta\phi + \alpha \quad (3.15)$$

where  $\phi$  is a the variable of interest and  $\beta$  and  $\alpha$  are constant coefficients. OpenFOAM offers two ode integrators, apparently developed specifically to integrate these particle equations, but that can be used for any equations in this form.

Both of the integrators are implemented as classes that inherit from a base class `IntegrationScheme`. The base class defines a pure virtual function `integrate` to be overridden and used to perform the integration in the derived classes. It has the following pseudo-code function definition and argument list

```
integrateResult integrate(phi, dt, alphaBeta, beta)
```

Here the first argument, `phi`, is the initial value for the variable of interest,  $\phi(t_0)$ . `dt` is the time step to integrate over; `alphaBeta` is the constant source term of the equation,  $\alpha$  in Equation 3.15; and `beta` is the multiplicative constant,  $\beta$  in Equation 3.15. The return type, `integrateResult`, is another helper class. In addition to some access functionality it just holds an array with two values, the integrated solution at time  $t_0 + dt$ , i.e.  $\phi_1 = \phi(t + dt)$ , and an average of the value of  $\phi$ ,  $\phi_{av}$ , throughout the integrated time interval  $dt$ .

The first derived integrator class is named “Analytical”. Since the source terms are frozen and the ode becomes a linear first order one and an analytical solution is available, for the example of Equation 3.15 that solution is

$$\phi(t) = \frac{\alpha}{\beta} + \left( \phi_0 - \frac{\alpha}{\beta} \right) \exp^{-\beta t} \quad (3.16)$$

Correspondingly the solution returned from the `integrate` function, again in pseudo-code, is

```
alpha = alphaBeta/beta
```

```
phi_1 = alpha + (phi - alpha) * exp(-beta * dt)
```

and the value of phi averaged over the integration time interval is

```
phi_av = alpha + (phi - alpha)*(1 - exp(-beta * dt))/(beta*dt)
```

.

The other integrator class offered is named “Euler”. It employs an implicit Euler method for the integration. Since the ode considered is linear in  $\phi$  this implicit treatment does not necessitate an iterative solution approach. The solution of Equation 3.15 at time  $t + dt$ , i.e.  $\phi_1 = \phi(t + dt)$  using an implicit Euler method is given by

$$\phi_1 = \frac{\phi_0 + \alpha dt}{1 + \beta dt}. \quad (3.17)$$

The computational counterpart to this solution is

```
phi_1 = (phi + alphaBeta*dt)/(1 + beta*dt)
```

and once `phi_1` is calculated the averaged value of phi over the time step `dt` is calculated as the arithmetic mean

```
phi_av = 0.5*(phi + phi_1)
```

The Euler integrator is used to solve the velocity equation and the Analytical integrator is used for the particle temperature equation. This is the default setting in OpenFOAM. The particle mass equation is handled entirely explicitly and neither of these integration schemes is used.

### 3.3 Devolatilization

Before the main particle equations are solved the devolatilization sub-model is used to determine source terms for the transfer of mass, species, enthalpy and momentum between phases. These transfer source terms are needed to solve both the continuous phase transport equations and the particle equations.

OpenFOAM implements the SFOR model in its `SingleKineticRateDevolatilization` class. The mathematical equivalent form of that equation used in OpenFOAM is

$$\frac{dm_\alpha}{dt} = -k(T_p) \cdot m_\alpha \quad (3.18)$$

where  $m_\alpha$  is the mass of a volatile species  $\alpha$  that remains within the particle. The Arrhenius rate,  $k(T_p)$ , is a function of the parcel temperature as

$$k(T_p) = A \cdot \exp\left(\frac{-E}{RT_p}\right) \quad (3.19)$$

where  $R$  is the universal gas constant,  $T_p$  is the particle temperature,  $A$  is the pre-exponential factor and  $E$  is the activation energy.

The evaluation of the SFOR devolatilization submodel depends on four of the particle properties and the current main gas phase time step  $dt$ . The current and initial parcel mass,  $m_p^0$  and  $m_p$ ; a list of the current mass fractions of volatile species within the parcel,  $Y_{p,\alpha}$ ; and the parcel temperature,  $T_p$ . The submodel then calculates and returns a list of mass increments yielded for every volatile specie  $\alpha$  over the current timestep from devolatilization,  $dm_{dev,\alpha}$ . The initial volatile mass fractions, initial particle mass and initial particle temperature are specified by the user in input files. The current particle mass, current volatile mass fractions and the current particle temperature vary throughout the simulation and are determined during the previous time step.

The SFOR model stores the rate constants,  $A$  and  $E$ , for each volatile species itself. They are specified by the user for each volatile species individually in an input file and are constant throughout the simulation unless updated by the user. It also stores a record of the initial volatile species mass fractions  $Y_{p,\alpha}^0$ ; these are specified by the user but after the first time step the particle no longer retains this information and so it needs to be store with the submodel. The submodel also stores a user specified variable that is used to decide when devolatilization is completed called the residual coefficient,  $r_c$ .

When the SFOR devolatilization submodel is evaluated it loops through each of the volatile species individually to determine mass loss. Before any equations are solved the model compares the current mass of the volatile with the initial mass scaled by the residual

coefficient. This is necessary because the mass yield determined by Equation 3.18 only asymptotically approaches the ultimate yield and the surface reaction model, though not utilized in this work, only becomes active after all of the volatile mass is yielded. If the current mass of a particular volatile remaining in the particle,  $Y_{p,\alpha} \cdot m_p = m_{p,\alpha}$  is less than the threshold determined as  $r_c \cdot (Y_{p,\alpha}^0 \cdot m_p^0) = r_c \cdot m_{p,\alpha}^0$ , then the devolatilization of this volatile species is considered to be completed and a local switch variable **done** is changed from **false** to **true** to indicate that. When all of the volatile species yields exceed this threshold the surface reaction model is activated and the devolatilization model is no longer evaluated.

Regardless of whether the yield has reached the **done** threshold the mass loss calculation proceeds afterwards. First the Arrhenius rate,  $k(T_p)$ , is calculated with Equation 3.19 using the rate constants,  $A_\alpha$  and  $E_\alpha$ , for the volatile species  $\alpha$  under consideration and the particle temperature. Then the SFOR equation 3.18 is explicitly integrated to determine the mass yielded for this species,  $dm_\alpha^{dev}$ , over the current time step,  $dt$ .

$$dm_\alpha^{dev} = dt \cdot k(T_p) \cdot m_{p,\alpha} \quad (3.20)$$

### 3.3.1 Dispersed Phase Source Terms

Once  $dm_\alpha^{dev}$  has been determined for every species the list of these mass yields is returned to the parcel class to determine transfer source terms. The explicit source term for particle mass equation, Equation 3.14, over a time step  $dt$ , is

$$\dot{m}_p^{dev} = -\frac{\sum_i (dm_\alpha^{dev})}{dt}. \quad (3.21)$$

Since the latent heat of devolatilization, i.e. the heat of reaction related to the coal breakdown to produce volatiles, is typically small its contribution is neglected and so devolatilization has no effect of the particle temperature equation. Similarly the particle velocity equation is unaffected by devolatilization aside from the associated particle mass loss.

### 3.3.2 Continuous Phase Source Terms

Coal particle devolatilization directly affects all four continuous phase transport equations, Equations 2.1 - 2.4 through transfer source terms. The particle source terms for each of the continuous phase transport equations is further decomposed as shown in Equations 2.5 - 2.8. Here we are concerned with only the devolatilization particle source contribution,  $S_{p,\beta}^{dev}$  where  $\beta$  represents one of the four transport equations. Each of the following source terms in this sub-section are based on the mass transfer from particles to the continuous phase. The total mass transfer for a particular particle is calculated by summing over all species mass losses from that particle. All of the particles within a cell must also be summed over to provide the total continuous phase source. To indicate the possession of the source mass loss increment,  $dm_{\alpha}^{dev}$ , by a particular particle a subscript,  $j$ , is added, i.e. the mass loss of species  $\alpha$  from particle  $j$  over the current time step  $dt$  is represented by  $dm_{\alpha,j}^{dev}$ .

The relevant source for the continuity equation, Equation 2.1, is  $S_{p,m}^{dev}$ . Which is calculated for a time step  $dt$  in a cell of volume  $V_C$  as

$$S_{p,m}^{dev} = \sum_j \left[ \frac{\sum_{\alpha} (dm_{\alpha,j}^{dev})}{V_C \cdot dt} \right] \quad (3.22)$$

where the summations are over all volatile species  $\alpha$  and all particles  $j$  within the cell.

$S_{p,h}^{dev}$  represents the particle devolatilization source term to the continuous phase sensible enthalpy equation. Though the heat of devolatilization is neglected the transfer of species from the particles to the continuous phase produces a source of sensible enthalpy. The sensible enthalpy source can be calculated as a function of the mass loss of species  $i$  from all particles  $j$  within a cell as

$$S_{p,h}^{dev} = \sum_j \left[ \frac{\sum_{\alpha} (dm_{\alpha,j}^{dev} \cdot h_{s,\alpha})}{V_C \cdot dt} \right] \quad (3.23)$$

where  $h_{s,\alpha}$  is the sensible enthalpy of the species  $\alpha$  evaluated at the continuous phase pressure interpolated to the particle location and the particle temperature.

The continuous phase momentum source is calculated very similarly. The injection of volatile species into the gas phase is assumed to occur at the particle velocity. The source

term can then be formed by summing the product of the particle mass release and velocity,  $\mathbf{U}_{p,j}$ , over all volatile species, and then summing all particles as

$$S_{p,u}^{dev} = \sum_j \left[ \frac{\sum_{\alpha} (dm_{\alpha,j}^{dev}) \mathbf{U}_{p,j}}{V_C \cdot dt} \right]. \quad (3.24)$$

Since continuous phase each species,  $\alpha$ , has its own transport equation, a corresponding source term,  $S_{p,y,\alpha}^{dev}$ , is also formed for each species. It is calculated from summing over each particle,  $j$ , the mass transfer of species  $\alpha$  in each time step  $dt$  for each cell of volume  $V_C$  as

$$S_{p,y,\alpha}^{dev} = \sum_j \left[ \frac{dm_{\alpha,j}^{dev}}{V_C \cdot dt} \right]. \quad (3.25)$$

### 3.4 Evaporation

To built-in `liquidEvaporation` class from OpenFOAM is used to model particle evaporation. Here the only liquid considered is water but the class provides a framework to evaporate a variable number of liquid species. This model was not modified and the evaporation process was not a focus of this research. Therefore only a brief description of the formation of the source terms for the particle and continuous phase equations is included. A detailed description of the mass loss calculations, as included for devolatilization and surface reactions, is not included. Those calculations involve modeling physics that are not relevant to this work.

The ultimate results of a call to the evaporation submodel are mass loss increments for any liquids evaporated over the time step  $dt$  for particle  $j$ , here just  $dm_{H_2O,j}^{evap}$ ; an enthalpy increment to describe the enthalpy of vaporization,  $dh_{vap}^{evap}$ ; and an enthalpy increment to describe the transfer of sensible enthalpy from the dispersed phase to the continuous phase,  $dh_s^{evap}$ .

The mass source term due to evaporation for the particle  $j$  mass Equation, 3.14, is calculated from the liquid mass loss increment as

$$\dot{m}_p^{evap} = - \frac{dm_{H_2O,j}^{evap}}{dt} \quad (3.26)$$

The enthalpy of vaporization is entirely consumed by the particle and the enthalpy of vaporization does not affect the gas phase directly. Therefore the particle enthalpy source

for Equation 3.11 is given by

$$\dot{h}_p^{evap} = \frac{dh_{vap}^{evap}}{dt} \quad (3.27)$$

The enthalpy transfer source term for the continuous phase is dependent on the sensible enthalpy transferred from the particle to the continuous phase during evaporation mass transfer. The source term depends on the summing, over all particle  $j$ , the mass transferred,  $dm_{H_2O,j}^{dev}$ , and the specific sensible enthalpy of water vapor at the particle surface temperature and interpolated cell pressure,  $h_{s,H_2O}$ , as

$$S_{p,h}^{evap} = \sum_j \left[ \frac{dm_{H_2O,j}^{evap} \cdot h_{s,H_2O}}{dt} \right] \quad (3.28)$$

## 3.5 Radiation

The dispersed phase plays an important role in the overall radiative heat exchange. The coal parcels affect the incident radiation transport Equation 2.24 through the coal particle absorption coefficient  $a_p$ , the scattering coefficient  $\sigma_p$ , and the parcel contribution to the emission of thermal radiation  $E_p$ . The parcel radiative effect is included through the `BinaryAbsorptionEmission` wrapper class that sums the dispersed and continuous phase contributions and coefficients that are calculated in separate modeling classes. The calculation of the continuous phase contribution is detailed in Section 2.3. The model class used to determine the dispersed phase effects is described below in this section. A new modeling class to incorporate the radiative effects of soot, `greyMeanSootAbsorptionEmission`, and a corresponding wrapper model, `ternaryAbsorptionEmission`, have been developed for this work and are described in Chapter 4.

The particle scattering factor is given by

$$\sigma_p = \frac{A_{sum} (1 - f) (1 - \epsilon_p)}{V_c} \quad (3.29)$$

where  $\epsilon_p = 1.0$  is the assumed emissivity of the coal particles,  $f = 0.5$  is the coal particle scattering factor (the OpenFOAM default value is used here) and  $V_c$  is the current cell volume in units of  $[m^3]$ .  $A_{sum}$  is the sum of projected particle areas in  $[m^2]$  and is defined



as a sum over the parcels in the current cell.

$$A_{sum} = \sum_p n_p \cdot A_p \quad (3.30)$$

Here  $n_p$  is the number of real coal particles represented by the parcel (see the beginning of this chapter for an explanation of relationship between physical particles and their computational representatives, parcels) and  $A_p = \pi D_p^2/4$  is the projected area of a single physical particle with diameter  $D_p$ .

The dispersed phase absorption coefficient and emission contribution are calculated within the particle cloud classes themselves. The `cloudAbsorptionEmission` class interfaces with the clouds in order to provide the main radiation model with access to the parcel dependent  $a_p$  and  $E_p$  values. The parcel absorption coefficient,  $a_p$  is calculated as

$$a_p = \frac{A_{sum}\epsilon_p}{V_c}. \quad (3.31)$$

$E_p$  is given by

$$E_p = \frac{\epsilon_p \sigma \sum_p (n_p A_p T_p^4)}{V_c} \quad (3.32)$$

where  $\sigma$  is the Steffan-Boltzmann constant. In both equations the sum  $\sum_p$  implies summation over all of the parcels in a cell.

## 3.6 Convection and Drag Force Reaction Source Terms

There are two sources in the continuous phase equations that couple them to the particle equations regardless of mass transfer. They are the convection source term in the specific enthalpy Equation 2.4, and the drag force reaction source term in the momentum Equation 2.2.

The convective heat transfer source,  $S_{p,h}^{conv}$ , mirrors the convective heating source term,  $\dot{h}_p^{conv}$ , in the particle temperature Equation 3.11. Any heat transfer to the particle through convection is lost from the gas phase surrounding it. The continuous phase source term for a particular cell can then be formulated by summing over all of the  $j$  particles present in

that cell

$$S_{p,h}^{conv} = - \sum_j \left( \frac{\dot{h}_{p,j}^{conv}}{V_C} \right) \quad (3.33)$$

with cell volume  $V_C$ .

Similarly the continuous phase reaction to the drag force source term can be formulated based on the particle equation drag force source term,  $\mathbf{F}_{\text{drag}}$ , from Equation 3.4. Any source of momentum for the particle is a sink in the gas phase momentum and vice versa. Again by summing over all of the particles in a particular cell the source term can be determined

$$S_{p,u}^{drag} = - \sum_j \left( \frac{\mathbf{F}_{\text{drag}} \mathbf{j}}{V_C} \right). \quad (3.34)$$

# Chapter 4

## Modifications and Additions

This work builds on previous pulverized coal modeling efforts [14, 36]. Its primary goal is to extend the previously developed coal tar and soot models to incorporate more detailed combustion chemistry coupling while implementing the improved models within the OpenFOAM framework. Here, the soot and tar reactions are fully coupled to a detailed chemistry reaction framework that enables a much more accurate accounting of species transfer and thereby further increases the accuracy of the combustion simulations. Furthermore all of the simulations here are performed in a transient fashion. This is in contrast to previous work which relied on steady state solutions [14, 36]. It is shown in Chapter 6 that in simulations with low particle loadings, as we investigate here, transient simulations capture important flow features that are not resolved in steady state solutions.

This work focuses on three subprocesses embedded within the larger framework of pulverized coal combustion: the primary devolatilization, tar formation and decomposition, and soot formation and consumption. These three subprocesses are closely linked as the products of one are the inputs for the next, e.g. in this work soot is only formed from tar decomposition. Furthermore, the focus here is not on the mechanistic or chemical modeling of these subprocesses but rather how they can be included into computational fluid dynamic (CFD) simulations to provide accurate results efficiently. An approach commonly used to achieve this end is to fit rate equations to experimental or complex computational model results and the latter approach is taken in this work.

The first subprocess considered is devolatilization. Two different primary devolatilization models have been implemented for this work. Both models represent primary devolatilization with an Arrhenius rate equation and differ based on the source of the rate constants. The first model is called the `AnalyticalSFORDevolatilization` model, and is very similar to the commonly used single kinetic rate models. This model is considered because it is used in the P.C. Coal Lab (PCCL) software to fit the detailed devolatilization predictions. The implementation is described in Section 4.1.1.

The second primary devolatilization model, here referred to as the `NthOrderDevolatilization` model, differs somewhat from the standard rate equation by using an additional exponential parameter. This model is considered because the C3M wrapper software for CPD [13] uses the `NthOrderDevolatilization` model to fit the CPD devolatilization predictions. The `NthOrderDevolatilization` model is described in Section 4.1.3.

Two distinct tar decomposition models have been developed for this study. The two tar decomposition models differ in their treatment of tar transport following its devolatilization and prior to its decomposition. They also differ in their predictions of tar decomposition product composition. The “Tracked Tar” (TT) model follows other work very closely, the tar is released from the parcel to the gas phase just as the other volatile species are. Tar decomposition then takes place within the continuous phase. The rate at which this decomposition occurs is dependent on rate equations that have been optimized by Ma [2] to match experimental results. The TT model can be paired with either devolatilization model and is described in more detail in Section 4.3.1.

The second tar decomposition model is a new model developed in this work. It is referred to as the PC model because it relies on PCCL as a ‘virtual experiment’ to predict tar decomposition rates and products which are then used to fit constants for the decomposition rate equations. In this model the tar evolved by a particular coal parcel is retained within that parent parcel as its decomposition proceeds. Obviously this unphysically limits the transport of tar which is in reality a gaseous species. The advantage of this approach is that it allows the PCCL rates for tar decomposition, which assume a discrete mass of tar, to be utilized. This is in contrast to other approaches like the TT model that require experiments

to optimize rate constants. The PC model necessarily includes its own devolatilization model that also uses rates based on PCCL predictions.

Additionally a novel framework to facilitate a modeling approach compromise between the two tar decomposition models has also been developed. It is referred to as the PCCL Conversion Framework (PCF). This framework enables PCCL tar decomposition predictions to inform the rate constants for the TT model, rather than experiments. This framework provides a way for PCCL determined tar decomposition rates to be utilized in gas phase reactions thus avoiding the assumption that tar is physically retained by its parent coal parcel. The PCF therefore results in a tar decomposition model that is identical to the TT model except for its tar decomposition reaction rate constants. The details of this framework are discussed in Section 4.3.3

A single soot formation/consumption model, the Two Equation soot model, has been implemented here and it closely follows other coal soot modeling efforts [2,14]. The rates for the equations are determined by Kronenburg, Bilger and Kent [37] and Josephson et al. [38]. Its implementation is described in Section 4.2.

Regardless of the models used in a particular simulation the relevant source terms are added to the continuous phase sensible enthalpy Equation 2.4 to account for soot and tar formation and decomposition. The modified equation is

$$\frac{\partial \rho h}{\partial t} + \frac{\partial \rho u_i h}{\partial x_i} - \frac{\partial P}{\partial t} - \frac{\partial}{\partial x_i} \left( \alpha \frac{\partial h}{\partial x_i} \right) = \rho (u_i g_i) + S_{p,h} + S_{c,h} + S_{r,h} + S_h^{\text{soot}} + S_h^{\text{tar}} \quad (4.1)$$

Where  $S_h^{\text{soot}}$  and  $S_h^{\text{tar}}$  are the source terms that derive from the soot and tar submodels. In addition to the enthalpy source terms, when the Two Equation soot model is used two more transport equations are solved, one for the soot particle number density and one for the soot mass fraction. When the tracked tar model is used an additional species transport equation is solved for the tar mass fraction.

## 4.1 Primary Devolatilization

### 4.1.1 AnalyticalSFORDevolatilization Model

The `SingleKineticRateDevolatilization` model, described in Section 3.3, has been modified for this work. As explained previously the built-in model implements an explicit Euler method to integrate the mass loss rate equation and thus determine the mass increment lost,  $dm_{dev,i}$ , over a time step  $dt$  for volatile species  $i$ . However, the rate equation is a first order linear ordinary differential equation for the volatile mass. Since the parcel temperature,  $T_p$ , is assumed to be constant during this evaluation, the coefficients of the equation are frozen, i.e.  $r \neq r(t)$ , and an analytical solution can be found. Using the analytical solution avoids the possibility of an overshoot when predicting mass loss which can potentially lead to predicting negative volatile mass.

The devolatilization mass loss equation,

$$\frac{dm_\alpha}{dt} = -k(T_p) \cdot m_\alpha; \quad k(T_p) = A \cdot \exp\left(\frac{-E}{RT_p}\right) \quad (4.2)$$

with Arrhenius rate  $k(T_p)$ , rate constants  $A$  and  $E$ , parcel temperature  $T_p$ , universal gas constant  $R$  and volatile species  $\alpha$  mass remaining in the parcel  $m_\alpha$ , can be solved analytically by separating the differential, integrating and exponentiating to yield

$$m_\alpha(t) = c_1 \exp(k \cdot t). \quad (4.3)$$

This approach still relies on solving the equation segregated from the particle temperature equation when calculating the Arrhenius rate  $k$ . That rate is updated at each time step and so this solution approach is not continuously used throughout the simulation but is instead used to describe the mass loss over a single time step. In addition to recomputing  $k$  the integration constant,  $c_1$ , must be determined for each time step. This can be done by considering a local time which is set to zero at the start of each mass loss calculation, i.e. at each overall time step. Then, given the initial volatile mass fraction  $m_{\alpha,0}$ , at the start of the time step we can determine  $c_1$  as

$$m_\alpha(0) = m_{\alpha,0} = c_1 \exp(k \cdot t) = c_1; \Rightarrow c_1 = m_{\alpha,0}. \quad (4.4)$$

Then the mass loss increment for each volatile species at each time step is calculated as

$$dm_{dev,i} = m_{i,0} \cdot \exp(k \cdot dt) \quad (4.5)$$

The mass loss increments are then treated exactly as described in Section 3.3 to form source terms for the particle and continuous phase equations.

#### 4.1.2 Using PCCL to Predict Rate Constants for the AnalyticalSFORDevolatilization Model

Two distinct tar decomposition/soot formation models have been developed in this work. For either model the primary devolatilization rates and yields can be determined with the commercial coal chemistry software P.C. Coal Lab (PCCL) [12]. In that case the AnalyticalSFORDevolatilization model will be used.

PCCL provides pseudo-speciated single first order rates (SFOR) which specify the primary devolatilization characteristics of coal particles. They are functions of the heating conditions and coal properties. The rates are referred to as pseudo-speciated because, while SFOR parameters are provided directly for some species, others are grouped into classes and share a set of SFOR parameters. The five of these species/species classes used in this study are tar, hydrocarbons, water, carbon monoxide and carbon dioxide.

It is not clear that it is appropriate to use the rate constants provided by PCCL directly in the OpenFOAM devolatilization model framework. PCCL performs a complex coal chemistry simulation that determines mass yield of volatile species as a fraction of the initial particle dry ash free (DAF) mass. PCCL then optimizes the pre-exponential and activation energy rate constants,  $A$  and  $E$  respectively, of a single first order rate equation to match the simulation. The rate equation fitted by PCCL is illustrated in Equation 4.6.

$$\frac{dy^{daf}}{dt} = A \cdot \exp\left(\frac{-E}{RT}\right) \cdot (y^{daf,\infty} - y^{daf}) \quad (4.6)$$

Here  $y^{daf}$  is the DAF mass yield of a particular volatile species. Importantly,  $y^{daf}$  is a mass fraction of the initial DAF particle mass in contrast to the variable current particle mass and mass fractions of this type will be referred to as ‘DAF initial mass fractions’ below.  $y^{daf,\infty}$

is the DAF ultimate yield for considered volatile species. The optimized rate constants of this equation, along with the ultimate DAF yield,  $y^{daf,\infty}$ , are an output from the PCCL simulation and are then used as an input to the OpenFOAM devolatilization model.

In contrast to the PCCL framework, in OpenFOAM the same rate constants are used in a different rate equation, the same as in Section 3.3 but reproduced here

$$\frac{dm}{dt} = -A \cdot \exp\left(\frac{-E}{RT}\right) \cdot m. \quad (4.7)$$

Here  $m$  is the mass of a particular volatile species that remains in the particle. Within the built-in devolatilization models of OpenFOAM this equation is integrated over a particle time step to determine the mass of a volatile species yielded. The goal of the rest of this subsection is to show that the rates fitted to Equation 4.6 can be used directly and meaningfully in Equation 4.7.

A naive approach to using the PCCL rate constants in OpenFOAM is to implement a new devolatilization model that integrates Equation 4.6 over a particle time step to calculate a species mass increment evolved. This allows the rate constants from PCCL to be used. For the sake of simplicity this argument will be based on the built-in OpenFOAM devolatilization model with explicit integration, as opposed to the analytical implementation discussed above in this section. Consider the discretized form of Equation 4.6

$$dy^{daf,\infty} = dt \cdot A \cdot \exp\left(\frac{-E}{RT}\right) \cdot (y^{daf,\infty} - y^{daf}). \quad (4.8)$$

Here  $dy^{daf}$  is the DAF initial mass fraction increment that is yielded over time step  $dt$ . The associated mass yield increment,  $dm$ , can be determined as a function of  $dy^{daf}$

$$dm = dy^{daf} \cdot (Y_{p,0}^{daf} \cdot m_0) \quad (4.9)$$

where  $Y_{p,0}^{daf}$  is the initial DAF fraction of the coal particle and  $m_0$  is the initial total mass of the particle so that  $(Y_{p,0}^{daf} \cdot m_0)$  is the initial DAF particle mass. We can then multiply both sides of Equation 4.8 by this factor

$$dm = dy^{daf} \cdot (Y_{p,0}^{daf} \cdot m_0) = \left[ dt \cdot A \cdot \exp\left(\frac{-E}{RT}\right) \cdot (y^{daf,\infty} - y^{daf}) \right] (Y_{p,0}^{daf} \cdot m_0). \quad (4.10)$$



The term  $(y^{daf,\infty} - y^{daf})$  is just the mass fraction of the initial DAF particle mass that has yet to evolve. If we multiply this fraction by the initial DAF mass of the particle,  $m_0^{daf}$ , we can determine the total current mass of a volatile within the particle, i.e.  $m$  as

$$m = (y^{daf,\infty} - y^{daf}) \cdot m_0^{daf} = (y^{daf,\infty} - y^{daf}) \cdot (Y_{p,0}^{daf} \cdot m_0) \quad (4.11)$$

Then substituting Equation 4.11 into Equation 4.10 we arrive at the explicit form of the equation used in the the built-in OpenFOAM model

$$dm = dt \cdot A \cdot \exp\left(\frac{-E}{RT}\right) \cdot m. \quad (4.12)$$

This illustrates that it is appropriate to use the rate constants  $A$  and  $E$  calculated by PCCL directly in the OpenFOAM devolatilization model. Care must be taken with the units of the gas constant and activation energy, however, since PCCL usually reports  $E$  in units of  $[kcal/(mol\ K)]$  and the default gas constant used in OpenFOAM for devolatilization calculations has units of  $[J/(kmol\ K)]$

### 4.1.3 NthOrderDevolatilization Model

The `NthOrderDevolatilization` model is again derived from the OpenFOAM built-in `SingleKineticRateDevolatilization` model. This model was developed because the C3M wrapper software for CPD [13], which is used when CPD is used to predict primary devolatilization, fits rate constants to a different rate equation than the standard SFOR equation one used in `SingleKineticRateDevolatilization`.

The total devolatilization mass loss equation in this model is given by

$$\frac{dm}{dt} = A \cdot \exp\left(\frac{-E}{RT_p}\right) \cdot (1 - X)^n. \quad (4.13)$$

Where  $X$  is the parcel conversion,  $R$  the universal gas constant and  $T_p$  the parcel temperature. This equation is integrated explicitly just as described in Section 3.3. The parcel conversion is calculated as

$$X = 1.0 - \frac{Y_{p,x} - Y_{p,x}^0}{1.0 - Y_{p,x}^0} \quad (4.14)$$

where  $Y_{p,x}$  is the mass fraction of the solid and gaseous products remaining in the particle normalized by the initial particle mass.  $Y_{p,x}^0$  is the same quantity calculated at the initial particle condition, i.e. before heating.  $A$ ,  $E$  and  $n$  are the rate constants predicted by C3M/CPD. The `NthOrderDevolatilization` as used in C3M is not speciated at all and thus the rate at which the volatiles are evolved is the same for all species.

## 4.2 Two Equation Soot Model

A semi-empirical Two Equation soot model based on previous studies [14, 36] is used. The transport equations for soot mass fraction,  $Y_s$ , and soot particle number density,  $N_s$ , are given by

$$\frac{\partial \rho Y_s}{\partial t} + \frac{\partial \rho U_i Y_s}{\partial x_i} = \frac{\partial}{\partial x_j} \left( \rho D_s \frac{\partial Y_s}{\partial x_j} \right) + S_{Y_s} \quad (4.15)$$

$$\frac{\partial \rho N_s}{\partial t} + \frac{\partial \rho U_i N_s}{\partial x_i} = \frac{\partial}{\partial x_j} \left( \rho D_s \frac{\partial N_s}{\partial x_j} \right) + S_{N_s}. \quad (4.16)$$

Here  $U_i$  are the fluid velocity components,  $\rho$  the fluid density and  $S_{Y_s}$  and  $S_{N_s}$  are the source terms for soot mass fraction and soot particle density respectively. The diffusivity of both variables,  $D_s$ , is determined from the fluid kinematic viscosity,  $\nu$ , and a soot Schimdt number,  $Sc_s = 700$  [14], as

$$D_s = \frac{\nu}{Sc_s}. \quad (4.17)$$

The soot mass fraction equation is analogous to the other species transport equations, c.f. Equations 2.3. In order to simplify the implementation of the model soot was included in the OpenFOAM thermodynamic database constructed for each simulation from the DRM-22 combustion mechanism. Only the thermodynamic data of soot was needed so the following entry for “SOOT” was appended to the mechanism thermodynamics file.

```
SOOT REF ELEMENT T 3/10C 1. 0. 0. 0.S 200.000 6000.000 1000. 1
1.59828070E+00 1.43065097E-03-5.09435105E-07 8.64401302E-11-5.34349530E-15 2
-7.45940284E+02-9.30332005E+00-3.03744539E-01 4.36036227E-03 1.98268825E-06 3
-6.43472598E-09 2.99601320E-12-1.09458288E+02 1.08301475E+00 0.00000000E+00 4
```

This entry is taken from the Burcat thermodynamic data file for the graphite [39]. Representing soot as graphite provides easy access to some of the requisite thermodynamic properties in the calculations detailed below in this section but also requires that special care be taken when calculating the gas density, an issue that is described in Section 4.2.1.

The soot mass fraction source term in Equation 4.15 can be further decomposed to

$$S_{Y_S} = S_{Y_S}^{TD} + S_{y,soot}^{soot}. \quad (4.18)$$

Similarly the soot particle number density source term in Equation 4.16 is decomposed as

$$S_{N_S} = S_{N_S}^{TD} + S_{N_S}^{soot}. \quad (4.19)$$

The term  $S_{Y_S}^{TD}$  represents the source of new soot particles derived from tar decomposition. Tar decomposition is the only pathway for new soot particle creation considered, e.g. acetylene derived soot nucleation is neglected. The calculation of  $S_{Y_S}^{TD}$  depends on the tar decomposition submodel used. The calculation of this source is discussed separately for each tar decomposition submodel, in Section 4.3.1 for the TT model and in Section 4.3.2 for the PC model.  $S_{N_S}^{TD}$  is the soot particle number density source due to soot particle creation. It depends on  $S_{Y_S}^{TD}$ , regardless of the tar decomposition model used and is given by

$$S_{N_S}^{TD} = S_{Y_S}^{TD} \cdot \frac{N_a}{M_S \cdot N_C}. \quad (4.20)$$

Where  $N_a = 6.023 \times 10^{26} [atoms/kmol]$  is Avagadro's number,  $M_S = 12.01 [kg/kmol]$  is the molar mass of soot and the number of carbon atoms per incipient soot particle  $N_C = 9 \times 10^4 [atoms/particle]$  is taken from Brown [3].

The source terms  $S_{y,soot}^{soot}$  and  $S_{N_S}^{soot}$  include models for the soot surface growth, agglomeration of soot particles and consumption of soot through oxidation and gasification and their calculation is detailed later in this section.

Overall, the Two Equation soot model contains five reactions that govern the growth and consumption of the gas phase soot and related species. These reactions and their rate equations constitute a system of coupled ordinary differential equations in a fashion very similar to the finite rate chemistry system used for the other reacting species in the main combustion model. The integration of the soot model system of ODEs is segregated from

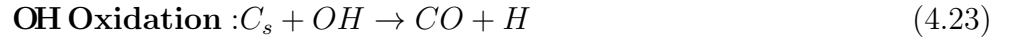
that of the main combustion model but the two systems are coupled by the several shared gas phase species mass fractions. The soot equations are not included in the main combustion system because the rate equation's dependence on several non-typical factors, e.g. soot surface area, makes them difficult to include in the OpenFOAM chemical reaction framework. The five reactions and their corresponding rate equations are listed below:



$$r_g = A_g \cdot [C_2H_2] \cdot \exp\left(\frac{-T_g}{T_C}\right) \cdot A_s$$



$$r_{ox,O_2} = T_C^{-0.5} \cdot A_{O_2} \cdot P_{O_2} \cdot \exp\left(\frac{-E_{O_2}}{RT_C}\right) \cdot \frac{A_s}{M_s}$$



$$r_{ox,OH} = T_C^{-0.5} \cdot A_{OH} \cdot P_{OH} \cdot \frac{A_s}{M_s}$$



$$r_{gas,OH} = T_C^2 \cdot A_{CO_2} \cdot P_{CO_2}^{0.5} \exp\left(\frac{-E_{CO_2}}{RT_C}\right) \cdot \frac{A_s}{M_s}$$



$$r_{gas,H_2O} = T_C^{-0.5} \cdot A_{H_2O} \cdot P_{H_2O}^n \exp\left(\frac{-E_{H_2O}}{RT_C}\right) \cdot \frac{A_s}{M_s}$$

The rates for each reaction  $r_i$  have unit  $\left[\frac{kmol}{m^3s}\right]$ ,  $P_i$  represents the partial pressure of species  $i$ ,  $[X]$  represents the molar concentration of species  $X$  in  $\left[\frac{kmol}{m^3}\right]$ ,  $T_c$  is the fluid temperature,  $A_s$  is the volumetric surface area of soot in  $\left[\frac{m_{soot}^2}{m^3}\right]$  and  $M_S = 12.01 \left[\frac{kg}{kmol}\right]$  is the molar mass of carbon. In each of the above equations  $C_s$  represents solid carbon which is the gas phase soot species used. The growth rate reaction and the two rate constants,  $A_g$  and  $T_g$ , are taken from Kronenburg, Bilger and Kent [37]. The two oxidation and two

gasification reactions and their corresponding constants are taken from Josephson et al. [38].

In addition to the reactions for soot and related species mass fractions the soot model contains a single term that governs the agglomeration of soot particles. Particle agglomeration provides a sink for the soot particle number density but does not affect the soot mass fraction. The soot particle agglomeration equation is

$$\frac{dN_s}{dt} = -2C_a\rho^2 \left(\frac{6\sigma T}{\rho_s}\right)^{0.5} \left(\frac{6}{\pi\rho_s\rho}\right)^{2/3} Y_S^{2/3} N_S^{11/6} \quad (4.26)$$

where  $C_a = 9.0$  is the agglomeration constant,  $\rho$  and  $\rho_s = 2000[kg/m^3]$  are the fluid and soot density [1] respectively and  $\sigma = 1.38 \times 10^{-23} [\frac{J}{K}]$  is the Boltzmann constant. The agglomeration equation and its constants, except soot density, are taken from Kronenburg [37]. This equation is explicitly integrated along with the other five and used to determine the particle number density source term

$$S_{N_s}^{soot} = \rho \cdot \frac{dN_s}{dt}. \quad (4.27)$$

in Equation 4.19.

At each continuous phase time step the system of equations is integrated in order to calculate source terms for the two soot variables and the related gas phase species. The five equations are integrated with an Euler explicit method over a sub time step that is a fraction of the main time step, it is user specified but the default is a third of the overall time step. Care is taken to prevent the over consumption of reactant species while integrating. The sources are calculated by first explicitly integrating the reaction rates over the sub time step,  $dt_s$ , to determine the final species mass fractions. For example the soot mass fraction at the end of the time step,  $Y_S^1$ , is calculated as

$$Y_S^1 = Y_S^0 + M_s \cdot (r_g - r_{ox,O_2} - r_{ox,OH} - r_{gas,OH} - r_{gas,H_2O}) \cdot \frac{dt_s}{\rho} \quad (4.28)$$

where  $Y_S^0$  is the initial soot mass fraction and  $M_s$  is the molecular weight of soot. The final mass fraction for the other 8 species involved in the model;  $C_2H_2$ ,  $H_2$ ,  $O_2$ ,  $CO_2$ ,  $CO$ ,  $OH$ ,  $H$  and  $H_2O$ ; are calculated the same way. If all of the relevant mass fractions are non-negative following the integration over the sub time step then the algorithm proceeds to the next sub

time step and repeats the process there, setting a new initial value  $Y_i^{new,0}$  to the final value of the previous time step  $Y_i^1$ . If the equations are successfully integrated over all of the sub time steps, avoiding negative mass fractions, then an overall final value is determined  $Y_i^f$  for the overall time step. That overall final value along with the initial mass fraction,  $Y_i^0$ , from the start of the overall time step, can then be used to formulate a source term for the relevant species  $i$  transport equation, including the soot mass fraction transport equation itself, as

$$S_{y,i}^{\text{soot}} = \left( Y_i^f - Y_i^0 \right) \cdot \frac{\rho}{dt} \quad (4.29)$$

It is possible that the integration over a sub time step leads to the over consumption of reactant species and therefore negative mass fractions, in that case it is corrected before the transport equation source terms are formed. First the problematic species mass fraction, i.e. the first species mass fraction to become negative, is identified. Then the fraction of its total change over the time step that takes place before the mass fraction becomes negative is determined as  $(Y_i^0 / (Y_i^0 - Y_i^1))$ . This fraction is used to linearly interpolate the other species mass fractions as well as the time step. The following pseudo-code illustrates this process.

```
// Variables:
// Array of final mass fractions: Y_f
// Array of initial mass fractions: Y_0
// Index of the problematic species: i
// Current sub time step: subdt
// Note that Y_f[i] is necessarily negative and Y_0 is necessarily positive

// First determine fraction of mass change in
// problematic species that is acceptable
scalar f = Y_0[i]/(Y_0[i] - Y_f[i])

// Use the fraction to interpolate other mass fractions and find remaining time
// Note that this results in Y_f[i] = 0.0
Y_f = f * (Y_0 - Y_f)
scalar time_remaining = (1.0 - f)*sub_dt
```

---

The integration over the now decreased sub time step, `time_remaining`, can then be repeated, after resetting `Y_0 = Y_f`. The problematic species mass fraction will be zero and any reactions that include it as a reactant will not proceed as the corresponding rate equation will necessarily include that mass fraction as a factor, this prevents continued over consumption.

In addition to the species transport equation source terms from the soot submodel,  $S_{y,i}^{\text{soot}}$ , the enthalpy of reaction is also considered and used to form a source term in the enthalpy transport equation. The soot submodel enthalpy source is given by

$$S_h^{\text{soot}} = \sum (-h_{f,i} \cdot S_{y,i}^{\text{soot}}). \quad (4.30)$$

Here  $h_{f,i}$  is the enthalpy of formation for species  $i$  and  $S_{y,i}^{\text{soot}}$  is the species equation source term for species  $i$  as discussed above.

### 4.2.1 Density Calculation Modifications for Soot

The use of the Two Equation soot model described above within the framework of a CFD simulation is very natural. It only requires the solution of an additional two transport equations when at least a dozen or more are already being evaluated and can describe soot yields quite accurately. However, by describing soot evolution with transport equations we essentially treat the soot as a continuous gas phase species. The validity of this assumption is debatable even though many of the smallest soot particles are barely larger than true gas phase species molecules. As the soot particles grow, their discrete nature become more relevant. An important consequence of this fact is evident in the calculation of the gas density.

OpenFOAM, at least within the solvers used here that are based on the built-in `coalChemistryFoam` solver, calculates the density twice during each time step. First it solves a continuity equation the solution of which is used in the pressure/velocity coupling algorithms. After the pressure, velocity, enthalpy, species and other equations are solved the density is recalculated using the ideal gas law based on the fluid compressibility,  $\psi$ , and

pressure,  $P$ , in each cell as

$$\rho = \psi \cdot P. \quad (4.31)$$

The compressibility is calculated as a mass based average of the local species compressibilities which are calculated for species  $i$  as

$$\psi_i = \frac{M_i}{RT} \quad (4.32)$$

where  $M_i$  is the species molar mass,  $T$  is the local fluid temperature and  $R$  is the universal gas constant. Since soot is included in the thermodynamic database as graphite its compressibility is also used in this calculation.

If the carbon contained within the soot particles was in reality present in the domain as individual carbon atoms this would be an accurate approach to determining the mixture density. Instead, we know that the carbon is stored in discrete particles and should contribute to the density calculation in a proper multiphase fashion. To apply that multiphase treatment the volumetric solid phase fraction, i.e. the volume fraction of soot particles,  $f_s$ , is determined as shown Equation 2.26, using the known soot density,  $\rho_{soot} = 2000 [kg/m^3]$  [1].  $f_s$  is then used to scale the densities as

$$\rho = (1 - f_s) \cdot (\psi^* \cdot P) + f_s \cdot \rho_{soot}. \quad (4.33)$$

Here the  $\rho$  is the corrected density, and  $\psi^*$  is the gas mixture compressibility calculated by excluding soot.

All of the solvers in this work have been modified to use Equation 4.33 instead of the original implementation when calculating gas densities from the ideal gas law.

### 4.2.2 Radiation Contribution of Soot

The soot plays an important role in the gas phase radiation modeling by making a significant contribution,  $a_s$ , to the total gas phase absorption coefficient,  $a_{gs}$ , (see Section 2.3). The relationship between the soot volume fraction,  $f_s$ , and the soot absorption coefficient contribution used by Xu et al. [36] is also adopted here

$$a_s = C_s f_s T. \quad (4.34)$$



Where  $C_s = 700$  [36] is a model constant and  $T$  is the local gas temperature. The soot volume fraction is calculated as described in Section 4.2.1.

## 4.3 Tar Decomposition Modeling

### 4.3.1 Tar Tracking Model

The Tar Tracking (TT) model follows the tar decomposition modeling from previous work closely [14, 36, 40]. Figure 4.1 shows a sketch of the devolatilization and tar decomposition pathways used in the TT tar decomposition model. The tar is treated as the rest of the volatile species are and is released from the coal particle to the gas phase immediately upon its primary devolatilization.

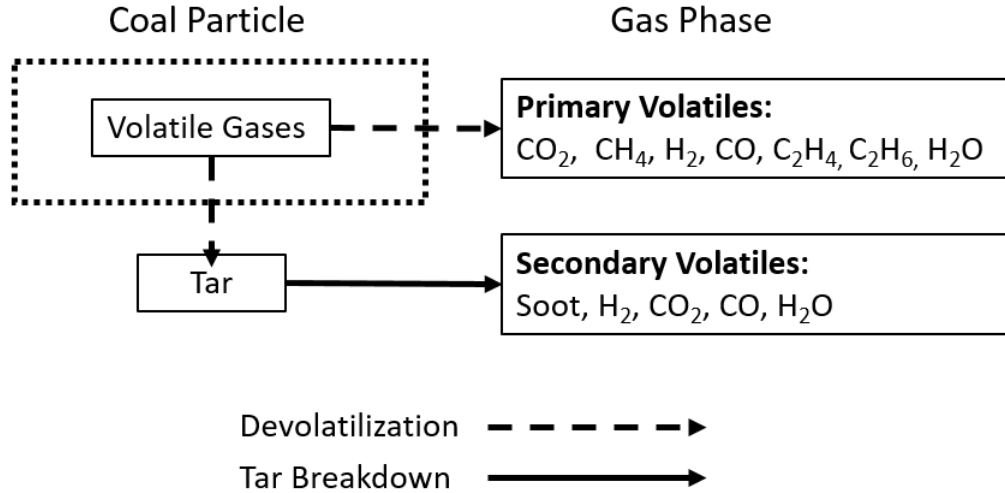


Figure 4.1: Diagram of devolatilization and tar breakdown pathways within the TT model.

The tar mass fraction is then tracked with the the tar species transport equation

$$\frac{\partial \rho Y_t}{\partial t} + \frac{\partial \rho U_i Y_t}{\partial x_i} = \frac{\partial}{\partial x_j} \left( \rho D_t \frac{\partial Y_t}{\partial x_j} \right) + S_{Y_t} \quad (4.35)$$

where  $U_i$  are the fluid velocity components,  $\rho$  the fluid density,  $Y_t$  the tar mass fraction and  $D_t$  the tar diffusivity. The tar diffusivity is calculated as

$$D_t = \frac{\nu}{Sc_{tar}} \quad (4.36)$$

where  $\nu$  is the fluid kinematic viscosity and  $Sc_{tar} = 0.7$  is the tar Schmidt number [14].

The source term,  $S_{Y_t}$ , can be further broken down as

$$S_{Y_t} = S_{p,y,TAR}^{dev} + S_{Y_t}^{TM} \quad (4.37)$$

where  $S_{p,y,TAR}^{dev}$  is the devolatilization source term for tar as described in Section 3.3 and  $S_{Y_t}^{TM}$  is the source term due to the tar decomposition gas phase reactions that are described below in this section.

In the TT model tar is represented as pyrene ( $C_{16}H_{10}$ ) within the OpenFOAM thermodynamic database by its thermodynamic data, shown below, to the DRM-22 combustion mechanism under the name “TAR”.

TAR	C	16	H	10	G	300.00	3500.00	1430.00	1
3.55205969e+01	2.97059226e-02	-5.18577408e-06	-7.74976601e-10	2.05764301e-13	2				
1.13998034e+04	-1.72584653e+02	-1.43149515e+01	1.69106058e-01	-1.51409692e-04	3				
6.73946823e-08	-1.17120082e-11	2.56527702e+04	8.56679628e+01		4				

Pyrene was selected because it is a polycyclic aromatic hydrocarbon (PAH) and has a relatively large molecular weight, 202  $[kg/kmol]$ , that is near the tar molecular weight predicted by PCCL,  $\approx 170 - 360 [kg/kmol]$ . This representation of tar as a single species within the thermodynamic database enables it to be easily devolatilized from coal parcels using the built-in OpenFOAM framework.

Tar is excluded from the main combustion solver and all reactions that involve tar are handled exclusively in this submodel. There are three reactions that govern consumption of gas phase tar, and constitute the tar model source term  $S_{Y_t}^{TM}$ .

$$\textbf{Soot Formation: } C_{16}H_{10} \rightarrow 16.85 C_s \quad (4.38)$$

$$r_{fs} = \rho \cdot Y_t \cdot A_{fs} \cdot \exp\left(\frac{-E_{fs}}{RT}\right) \frac{1}{M_s}$$

$$\textbf{Oxidation: } C_{16}H_{10} + 16 O_2 \rightarrow 16 CO_2 + 5 H_2 \quad (4.39)$$

$$r_{ox} = \rho \cdot (Y_t + Y_{O_2}) \cdot A_{ox} \cdot \exp\left(\frac{-E_{ox}}{RT}\right) \frac{1}{M_s}$$

$$\textbf{Cracking: } C_{16}H_{10} \rightarrow 7.065 CO + 2.208 H_2 \quad (4.40)$$

$$r_{cr} = \rho \cdot Y_t \cdot A_{cr} \cdot \exp\left(\frac{-E_{cr}}{RT}\right) \frac{1}{M_s}$$

Here  $\rho$  is the fluid density,  $Y_i$  are species mass fractions,  $R$  is the universal gas constant and  $T$  is the fluid temperature. The rate constants in each equation,  $A_x$  and  $E_x$ , and the rate equations, are taken from Josephson et. al [41]. The unit of the reaction rates,  $r_i$ , is  $[kmol/(m^3s)]$

Clearly two of the three chemical equations presented above do not maintain elemental consistency. This inconsistency is caused by neglecting some of the complex chemistry involved in the tar decomposition process in an effort to simplify the model. Instead, other constraints are considered to specify the stoichiometric coefficients. In the soot formation reaction the mass of the reactant and product species is conserved. The tar oxidation reaction maintains both elemental and mass consistency. In the cracking reaction the product coefficients are selected such that mass and C/H ratio is conserved.

These three reactions are used to calculate source terms for the main gas phase species and sensible enthalpy transport equations. Care is taken when calculating the source terms to not over-consume the reactant species. These equations are integrated explicitly over a time step  $dt$ . The integration follows the algorithm laid out in Section 4.2 in order to prevent the over consumption of reactant species leading to negative mass fractions.

Upon the successful integration of the tar and the five related species;  $C_s$ ,  $C_{16}H_{10}$ ,  $O_2$ ,  $CO_2$ ,  $H_2$  and  $CO$ ; the mass fraction at the end of the time step,  $Y_i^1$ , is determined and can

be used to calculate the sources for the species transport equations, including the soot and tar equations,

$$S_{y,i}^{\text{tar}} = (Y_i^1 - Y_i^0) \cdot \frac{\rho}{dt}. \quad (4.41)$$

Once the species sources are formed they are used to calculate the enthalpy equation sources

$$S_h^{TD} = \sum (-h_{f,i} \cdot S_{y,i}^{\text{tar}}) \quad (4.42)$$

where  $h_{f,i}$  is the standard enthalpy of formation of the species  $i$ .

### 4.3.2 PC Tar Decomposition Model

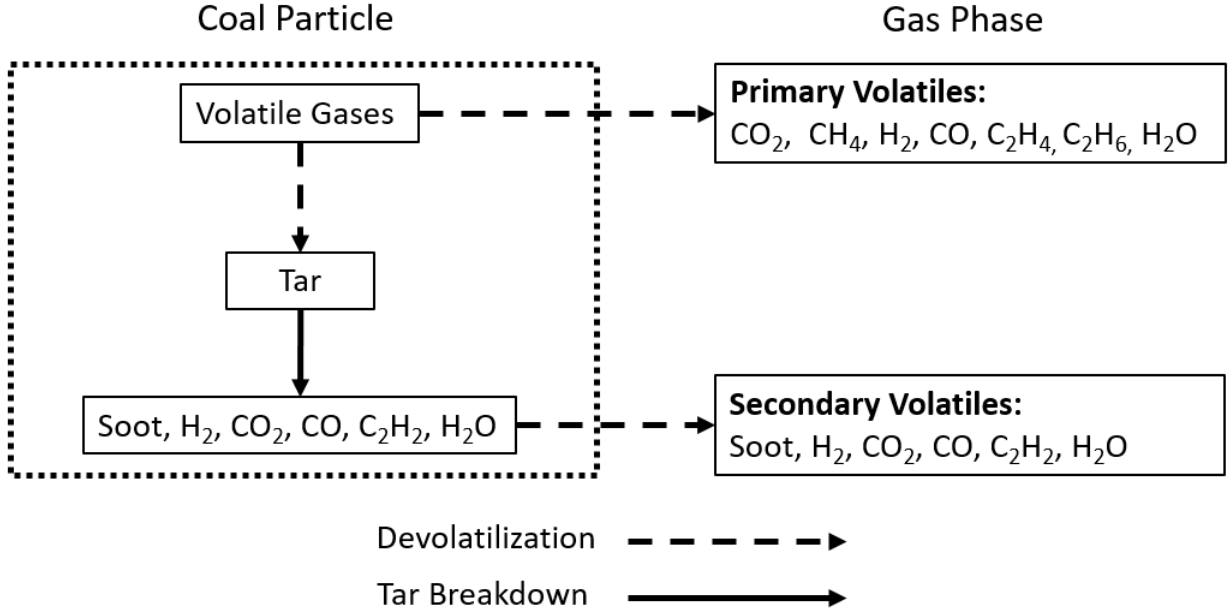


Figure 4.2: Diagram of devolatilization and tar breakdown pathways within the PC model.

Because PCCL is used to predict tar breakdown instead of experiments there are two differences between the current model and others which rely on different coal chemistry analysis or experiments. First, although PCCL provides rates for tar breakdown they are based on a discrete mass of tar, specifically the amount released by a single coal particle.

This is a disadvantage compared to the concentration based rates used to describe tar decomposition in other approaches that permit the breakdown of tar to be incorporated into continuous transport equations, e.g. the models in [14, 36] and the TT model in this work. Secondly, PCCL specifies the composition of the tar breakdown products by relying on its coal chemistry analysis algorithms to predict tar breakdown. This is a significant advantage over other approaches which typically assume the resultant species and perform elemental or energetic balances based on the proximate/ultimate analyses and heating value of the coal to determine the composition [36].

Figure 4.2 illustrates the devolatilization and tar decomposition pathways used in this model. Tar is represented in this model by naphthalene,  $C_{10}H_8$ . That species was selected because it is a large aromatic hydrocarbon that should be similar to physical tars. The selection of a tar surrogate in this model based on molecular weights is not as important as in the TT model because it is entirely consumed before reaching the gas phase and its transport is therefore unimportant. Naphthalene was added to the OpenFOAM thermodynamic database for by appending the following entry to the DRM-22 mechanism thermodynamics file used for the simulation.

TAR	C	10H	8	G	300.00	3500.00	1370.00	1
1.51184828e+01	3.89675576e-02	-1.78248659e-05	3.92092279e-09	-3.39215689e-13	2			
1.01121562e+04	-6.09041102e+01	-8.71832426e+00	1.08564074e-01	-9.40254318e-05	3			
4.10014902e-08	-7.10574258e-12	1.66434413e+04	6.15987876e+01					4

As described above in Section 4.1, the primary volatile gases (except tar in this case) are evolved from the coal particle and immediately released to the gas phase. In this model the mass of tar evolved during primary devolatilization is retained in the Lagrangian phase particle. While this retention limits, perhaps unphysically, the spatial transport of tar between its creation and decomposition, it also allows the rates calculated by PCCL to govern its decomposition as a discrete mass. This in turn permits the use of the PCCL predicted tar decomposition product composition and assumptions about the chemical form of tar and its decomposition products can be avoided.

The tar is initially treated just as any other volatile species within the coal particle. The primary devolatilization rate from PCCL is used to determine the mass of tar,  $dm_t$ , evolved over a particle time step.  $dm_t$  is then retained within the particle and the source terms for the continuous phase transport equations, Equations 2.1 - 2.4, are not affected by the primary devolatilization of tar. The mass of tar that has undergone primary devolatilization and accumulates in the particle is referred to as secondary tar,  $Y_{st}$ .

This secondary tar undergoes decomposition into simpler molecules and soot. The rate at which it decomposes is given in Equation 4.43

$$\frac{dY_{st}}{dt} = A_{st} \cdot \exp\left(\frac{E_{st}}{RT}\right) \cdot (Y_{\infty} - Y_{st}). \quad (4.43)$$

Where the subscript ‘ $st$ ’ refers to secondary tar and  $Y_{\infty}$  is the ultimate tar yield on a DAF basis. Any secondary tar that accumulates from primary devolatilization is available for decomposition immediately. When there is tar decomposition the mass of the product species are released to the gas phase just as the other volatile gases are released during primary devolatilization. Equation 4.43 is integrated explicitly over a continuous phase time step  $dt$  to form a mass increment of secondary tar to be decomposed from particle  $j$ ,  $dm_{st}^j$ .

The product species of tar decomposition are listed in Figure 4.2. The amount of a particular product species  $i$  produced per mass of tar decomposed is specified by PCCL as a mass fraction,  $f_i$ . Those fractions are used when tar decomposition takes place in order to form continuous phase species transport equation source terms by summing over the particles,  $j$ , in a cell

$$S_{y,i}^{\text{tar}} = \sum_j \left[ \frac{dm_{st}^j \cdot f_i}{V_c \cdot dt} \right] \quad (4.44)$$

where  $V_c$  is the volume of the local cell. These source terms are then completely analogous to the primary devolatilization source terms described in Section 3.3.

### 4.3.3 PCCL Conversion Framework (PCF)

The TT tar decomposition model relies on experimental data for the determination of its rate constants. The rate equations used in that model permit rate evaluation based on the

knowledge of the local tar mass fraction thermodynamic properties from a simulation, e.g. if those fields are known in a computational cell the tar decomposition rates can be determined and used for the corresponding transport equations.

In contrast the rate equation used in the PC model relies on tracking the amount of tar released by a particular particle/parcel. PCCL fits the following rate equation to its coal analysis results

$$\frac{d \Delta Y_{tar}(t)}{dt} = k_{tar} \cdot (\Delta Y_{tar}^{\infty} - \Delta Y_{tar}(t)). \quad (4.45)$$

Where  $k_{tar}$  is the Arrhenius rate in which rate constants are fit.  $\Delta Y_{tar}$  is a measure of the amount of tar that has been decomposed. It is a mass fraction of the DAF particle initial mass. Its initial value is zero and its ultimate value is  $\Delta Y_{tar}^{\infty}$ .  $\Delta Y_{tar}^{\infty}$  is also equal to the fraction of the total initial DAF particle mass that is ultimately released as tar, assuming primary devolatilization is completed. The knowledge of the local tar mass fraction and thermodynamic properties in a given computational cell of a simulation are not sufficient for the evaluation of this rate equation. Rather than knowledge of the tar mass fraction in a cell these rates require information about the initial mass of the particle that produced the tar and how much of it has already been decomposed. That is why it is necessary to retain the tar within the parcel in simulations utilizing the PC model. Effectively PCCL treats the tar as a smaller second coal particle and performs a similar analysis on it. That treatment is not consistent with most attempts to incorporate tar decomposition modeling into CFD simulations.

The goal of the PCCL Conversion Framework (PCF) is to avoid this inconsistency by utilizing the raw output data of PCCL, in contrast to the fitted rate constants used in the PC model, in the place of traditional experiments. The PCCL output data from a devolatilization and tar decomposition simulation is reformatted in such a way that a rate constant optimization, e.g. as performed by Ma [2] to generate the rates that are used in the TT model, can be performed. Assuming the coal analysis/tar decomposition algorithms of PCCL are accurate this approach has the added benefit of reducing the need for experiments to determine tar decomposition rates.

The raw outputs of PCCL used for this method are always reported as a DAF initial

particle mass fraction yields. That is to say that any mass yield considered is normalized against the initial DAF mass of the particle. Mass fractions of this form will be referred to as 'DAF initial mass fractions' below and will be represented with an over-tilde to distinguish them from other mass fractions. A time series of these DAF initial mass fractions is produced by PCCL for every primary volatile species, including primary and secondary tar, as well as any light gas species that result from tar decomposition. Secondary tar is a term used by the PCCL manual to describe the actual amount of tar present. In contrast primary tar measures the total amount of tar released, without regard for tar decomposition. The primary tar DAF initial mass fraction yield therefore increases monotonically in time while in actuality the tar mass fraction will tend to zero as it is decomposed which is represented by the secondary tar mass fraction yield, see Figure 4.3. The purpose of defining these two distinct tar quantities is to enable the calculation of the DAF initial mass fraction of tar that has been decomposed, it is given by

$$\Delta\tilde{Y}_{tar} = \tilde{Y}_{tar}^p - \tilde{Y}_{tar}^s \quad (4.46)$$

where  $\tilde{Y}_{tar}^p$  and  $\tilde{Y}_{tar}^s$  are the primary and secondary tar DAF initial mass fractions respectively.

These outputs are used in PCF to populate an idealized zero dimensional reactor that is representative of the thermophysical state surrounding the coal particle. The state of the reactor progresses as the PCCL devolatilization/tar decomposition wire grid simulation advances. At time zero no devolatilization has taken place and the zero dimensional reactor is assumed to contain only a fixed mass of nitrogen, here half of the initial DAF particle mass. Nitrogen is selected because it is used as the inert carrier gas in the PCCL simulations. In subsequent time steps, as primary devolatilization begins, the DAF initial mass fraction yields of volatile species are reported. These volatile DAF mass fraction yields are combined with the nitrogen already present in the reactor to determine mass fractions within the zero dimensional reactor. For example the mass fraction, the traditional mass fraction of a mixture not the DAF initial mass fraction, of a volatile species  $i$  within the zero dimensional reactor at time  $t$  is given by

$$Y_i = \frac{\tilde{Y}_i}{\tilde{Y}_{N_2} + \sum_j \tilde{Y}_j}. \quad (4.47)$$



Here  $\tilde{Y}_i$  represent the DAF initial mass fraction yield at a particular time for species  $i$ . The fixed amount of nitrogen within the reactor is represented by  $\tilde{Y}_{N_2}$  which is equal to 0.5 since it is assumed the mass of nitrogen equals half the DAF initial particle mass. The sum in the denominator is over all volatile and tar decomposition species, including species  $i$ .

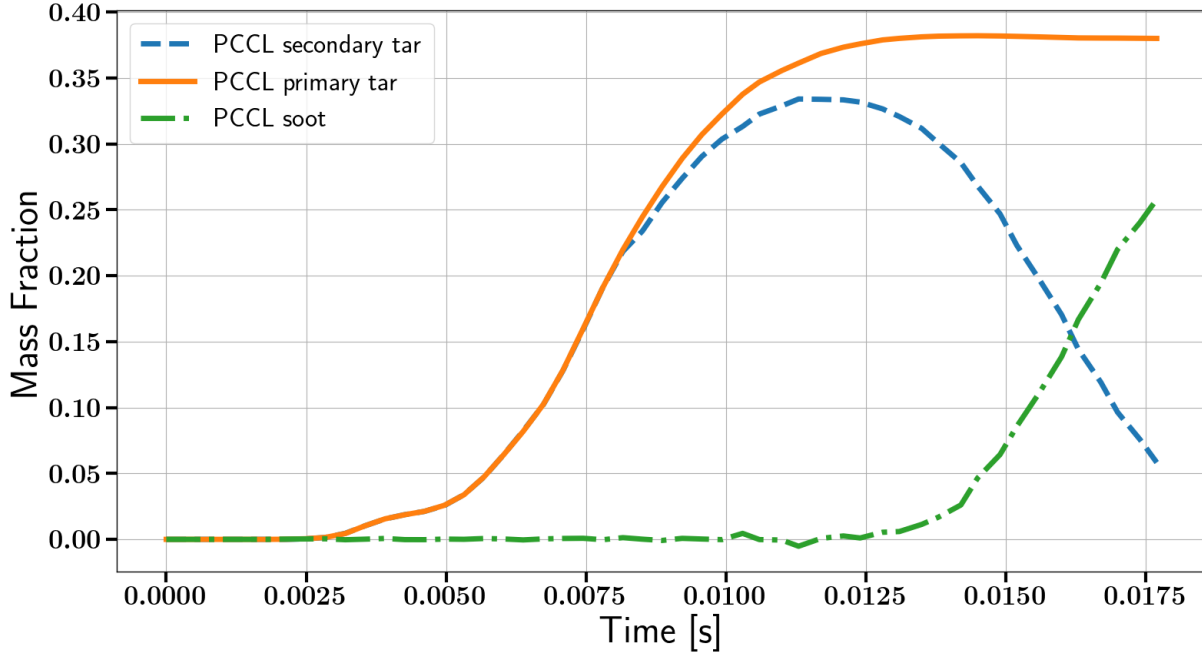


Figure 4.3: Mass fractions of primary tar, secondary tar and soot in the zero dimensional reactor representing the particle environment.

This transformation from a DAF initial mass fraction framework, that is dependent on a particle, to a more CFD friendly zero dimensional reactor is the key step in the PCF. With Equation 4.47 the DAF initial mass fraction yield time series reported from the PCCL analysis can be converted to more traditional mass fraction time series. These time series are calculated for all volatile species as well as primary and secondary tar. An example of the mass fractions within the reactor as the PCCL simulation proceeds for the secondary tar, primary tar and soot is given in Figure 4.3.

These trends then become the goal for the optimization of rate constants in rate equations identical to those used in the TT model. The mass fraction of secondary tar within

the reactor,  $Y_{star}$  can be predicted by integrating the rate equation

$$\frac{dY_{star}}{dt} = \frac{dY_{ptar}}{dt} - R_{sf} - R_{cr}. \quad (4.48)$$

Where  $\frac{dY_{ptar}}{dt}$  is the rate of primary tar formation from devolatilization.  $R_{sf}$  and  $R_{cr}$  are the rates of soot formation and tar cracking/decomposition respectively, both are processes that consume tar. The rate  $\frac{dY_{ptar}}{dt}$  is determined directly from the PCCL data numerically. The rates of soot formation and tar cracking are functions of the amount of secondary tar available and are given by the equations

$$R_{sf} = Y_{star} \cdot A_{sf} \cdot \exp\left(\frac{-E_{sf}}{RT}\right) \quad (4.49)$$

and

$$R_{cr} = Y_{star} \cdot A_{cr} \cdot \exp\left(\frac{-E_{cr}}{RT}\right). \quad (4.50)$$

This system then forms a single ODE with  $Y_{star}(0) = 0$  initial condition that can be integrated to determine the secondary tar mass fraction within the reactor. The problem is fully specified except for the soot formation and cracking rate constants,  $(A_{sf}, E_{sf}, A_{cr}, E_{cr})$ .

The set of these constants that can force the PCF differential Equation 4.48 to match the secondary tar trends predicted by PCCL is not unique however. Therefore another constraint is considered. As pictured in Figure 4.3 the soot mass fraction trend can also be determined from PCCL. This trend is used to first optimize only the soot formation parameters,  $(A_{sf}, E_{sf})$ . This is done by minimizing the difference in the PCCL trend and the result of the integration of Equation 4.49. During this optimization the cracking rate constants,  $A_{cr}$  and  $E_{cr}$ , are held constant at their values prescribed by Ma as an initial assumed value. The result of this optimization is pictured in Figure 4.4

Once the soot formation rate constants are determined the cracking rate constants can be optimized similarly. This second optimization is performed to force the PCF model secondary tar mass fraction, determined from integrating Equation 4.48, to match the secondary tar mass fraction trend predicted by PCCL. The result of the sequential optimizations is pictured in Figure 4.5.

The optimized rate constants provided by this procedure are then used directly in a

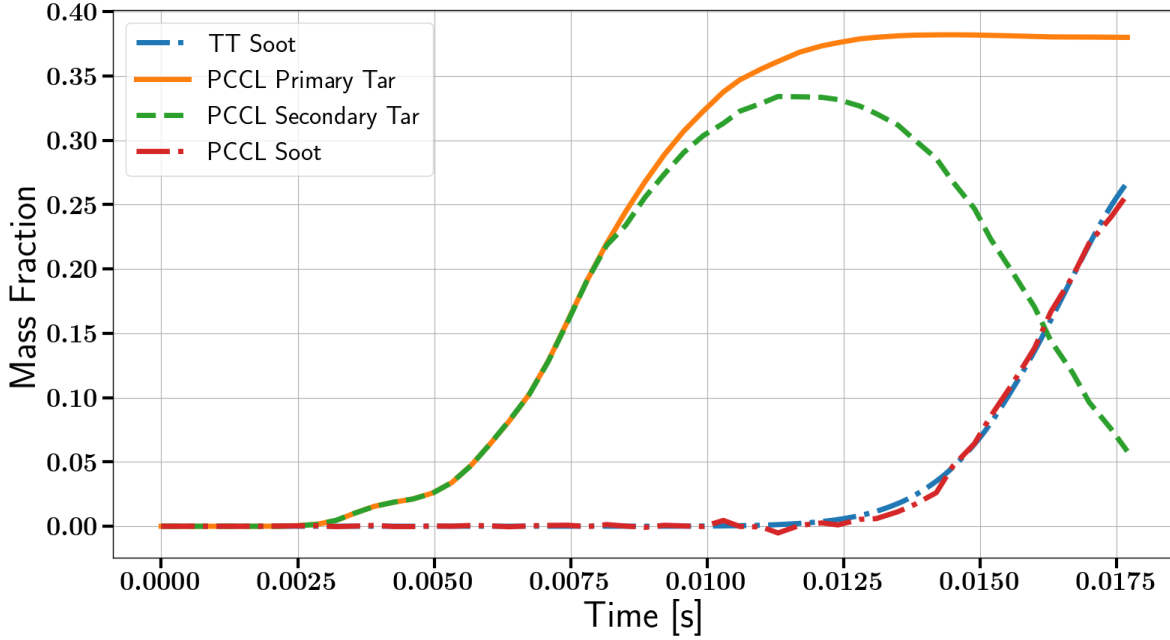


Figure 4.4: Result of soot formation rate constant optimization.

Table 4.1: Comparison of the Arrhenius rate constants for soot formation (sf) and tar cracking (cr) calculated through the PCCL Conversion Framework and those determined from experimental data by Ma [2]. Activation energies have units of [kJ/mol] and pre-exponential factors have units of [1/s].

	$A_{sf}$	$E_{sf}$	$A_{cr}$	$E_{cr}$
<b>Ma</b>	$5.02e^8$	198.9	$9.77e^{10}$	286.9
<b>PCF</b>	$4.97e^8$	191.82	27.9	0.796

copy of the TT model, now called the PCF model, for CFD simulations. The rate constants generated are compared with those determined by Ma from experiments in Table 4.1

#### 4.3.4 Note on Model Nomenclature

In Chapters 5 and 6 the setup and results of simulations using the devolatilization and tar decomposition models presented above is discussed. There is a wide array of possible model combinations that can be used to perform these simulations. Some naming conventions for these combinations are now presented and will be used through the following sections.

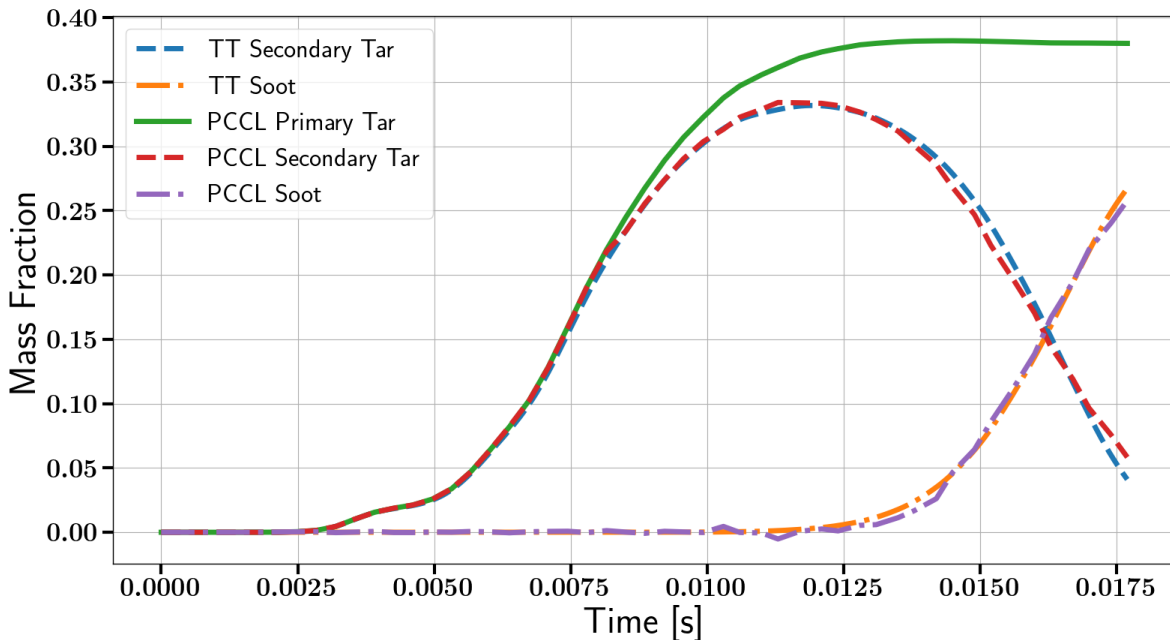


Figure 4.5: Result of soot formation and cracking rate constant optimization.

The TT model can be used with either the `AnalyticalSFORDevolatilization` or the `NthOrderDevolatilization` models depending on whether PCCL or CPD is the desired coal chemistry software. For the sake of brevity and to clarify which coal analysis software is used the models are lumped together as either 'CPD/TT' or 'PCCL/TT'. It should be remembered though that technically CPD and PCCL are the coal analysis programs used as virtual experiments to fit the rate constants for the two devolatilization models and PCCL or CPD are not used directly in the simulations.

Similarly, the PCF is not truly a tar decomposition model but it is referred to in subsequent chapters as though it is. When simulations are mentioned to have been performed with 'PCCL/PCF' or 'CPD/PCF' it means that the TT model is used with rates determined by the PCF and then coupled to the `AnalyticalSFORDevolatilization` or `NthOrderDevolatilization` devolatilization model respectively.

Finally the PC model is not as flexible as the other two tar decomposition models. Its design necessitates an incorporated devolatilization model. That model uses rates that are determined by PCCL and are evaluated in the same way as for the `AnalyticalSFORDevolatilization`

model. Any simulations performed with the PC tar decomposition model are therefore referred to having used the 'PCCL/PC' model.

# Chapter 5

## Validation

The Brigham Young University (BYU) flat flame burner experiment performed by Ma [2] is the only experiment used to validate the models in this study. It is selected because it is amenable to simulation with CFD and other coal flow experiments that measured fields of interest are not, e.g. Chen et al. [42,43]. The burner entrains pulverized coal particles in a central flow that is surrounded by a methane and hydrogen co-flow. The co-flow provides heat to the entrained coal particles to drive the coal decomposition processes of interest. A schematic of the burner is shown in Figure 5.1.

Although some particle free simulations are performed, most of the BYU flat flame burner simulations feature coal particles that are transported in a Lagrangian fashion as described in Chapter 3. Due to the discrete nature of the coal particles the simulations that include them are necessarily transient and will not converge in a traditional sense. References to a converged solution below refer to a flow state in which a windowed temporal average, with a window of 0.5 [s], of the velocity and temperature fields has converged fully. To distinguish this state from a traditional converged state it is referred to as a pseudo convergence. Any simulations that do not include particles can and do attain a traditional converged solution.

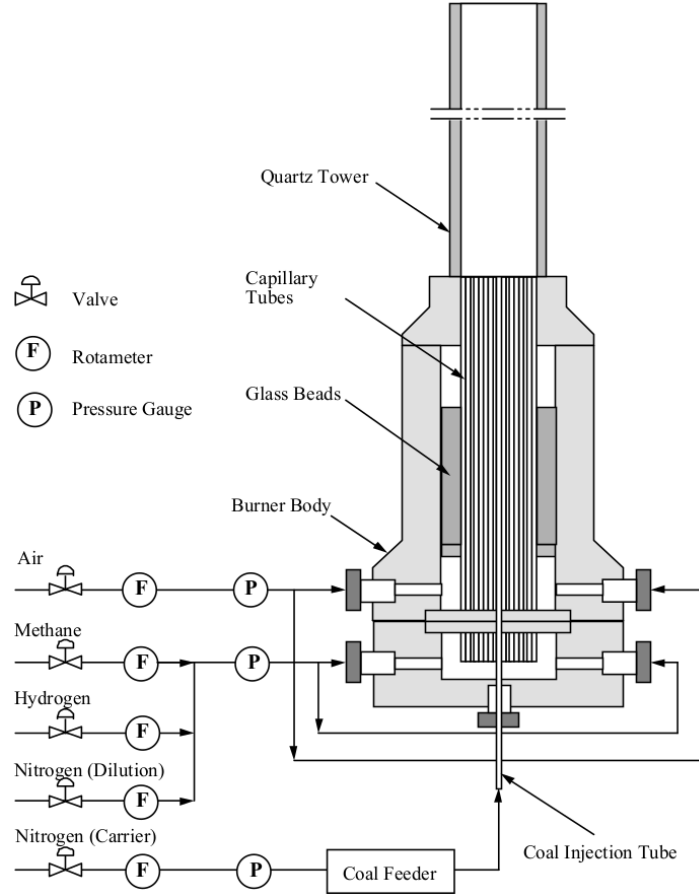


Figure 5.1: Schematic of the flat flame Hencken style burner used by Ma. Figure taken from Ma [2].

## 5.1 BYU Flat Flame Burner Case Setup

The experimental data from Ma's thesis [2] is used to validate the current models. This experiment is particularly useful for pulverized coal modeling studies as it reports soot and volatile gas yields as a DAF mass fraction of the coal injected. The flat flame burner is described in detail in the thesis. The burner is constructed from a central small tube, of diameter  $3.0\text{[mm]}$  [3], surrounded by a  $51\text{[mm]} \times 51\text{[mm]}$  square array of capillary tubes. The end of the central entrainment tube extends  $2\text{[mm]}$  above the co-flow burner surface. The central tube flows a carrier gas, here nitrogen, used to entrain the solid particles. The co-flow fuel flows inside about capillary tubes while the oxidizer flows around them. Depending on the sampling procedure being used by the experimenters, see the thesis for details, either a

round Pyrex tower or a square quartz tower was used to isolate the flow from its surroundings.

The burner geometry is modeled as an axisymmetric wedge here rather than the real square shape. This modeling approach decreases the computational cost considerably. The entire numerical domain is a  $30^\circ$  wedge as pictured in Figure 5.2 and the inlet plane is shown in Figure 5.3. The inflow areas of the coal entrainment flow and co-flow are appropriately scaled to represent their experimental counterparts (with a correction for the co-flow to account for the area taken by the honeycomb structures). The axial length of the domain is  $0.25[m]$  this length was selected based on earlier experimental results that suggested devolatilization, combustion of volatiles and soot formation all occurred within this range.

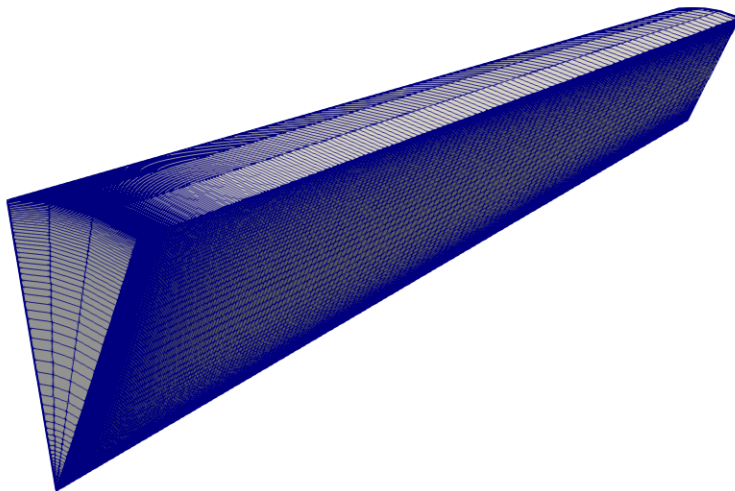


Figure 5.2: Simulation geometry.

A structured mesh is used with significant stretching to accommodate the strong shear layers between inlet streams near the entrance. The use of axisymmetric cyclic boundary conditions on the azimuthal sides of the geometry dictates a minimum of three cells in the azimuthal direction and three azimuthal cells are used here.



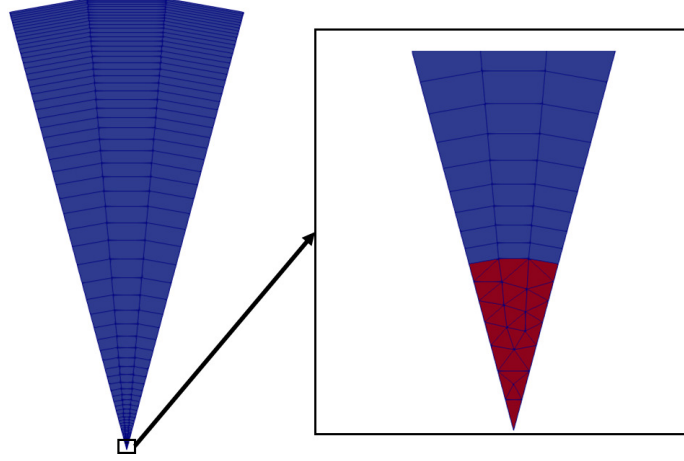


Figure 5.3: On the left the entire inlet plane of the axisymmetric simulation is pictured. On the right a magnified image of the bottom tip of the inlet plane is shown. In both images the blue regions represent the co-flow inlet while the red region represents the coal entrainment inlet. The thin interior black lines represent cell faces.

### 5.1.1 Boundary Conditions

With this co-flow burner surface design there are many small diffusion flames that result from the mixing of oxidizer and fuel, as reported by Ma the flames are lifted from the burner surface by approximately  $2\text{ [mm]}$ . Ma used three different co-flow inlet compositions, all three are rich mixtures and the species flow rates are presented in Table 5.1. Each of the three co-flow compositions is referred to by its maximum downstream temperature when operated and measured without particle injection. In this study we only compare results to the two leanest cases, i.e. to  $\phi = 1.26$  and  $\phi = 1.30$ .

Table 5.1: BYU flat flame burner experiment co-flow inlet conditions adapted from Table 3.1 in Ma [2]. All species flow rates are given in units of standard liters per minute with the standard conditions of  $298\text{ [K]}$  and  $1.0\text{ [atm]}$ .

Temperature [K]	CH4	H2	N2	O2	$\phi$
1900	5.64	0.0	33.8	8.97	1.26
1800	5.47	0.0	33.7	8.44	1.30
1650	5.12	2.91	35.1	7.93	1.48

The coal entrainment gas which flowed through the central tube was composed entirely

of  $N_2$  and had a flow rate of  $39.7e^{-3}$  [SLPM], regardless of the co-flow composition selected.

In modeling the co-flow it was assumed that the many small diffusion flames, resulting from the mixing of oxidizer and fuel above the burner surface, could be represented by a single premixed flame over the entire burner surface. To further decrease the modeling complexity an equilibrated mixture, rather than a mixture of fuel and oxidizer, was injected through the co-flow inlet boundary face. The equilibration of the inlet gases, see Table 5.1 for the initial mixtures, was performed adiabatically. This lead to unphysically high temperatures throughout the domain as in reality some heat is lost through conduction to the burner. The co-flow inlet temperature was corrected to account for this heat loss and that procedure is described in Section 5.1.2.

The co-flow was equilibrated with Cantera [44] with the same DRM-22 mechanism used in the CFD simulations. Following the equilibration almost all of the species in the DRM-22 mechanism were predicted to be present in non-zero mass fractions, and a threshold mass fraction of  $Y_{th} = 1e^{-6}$  was selected as a cutoff for species consideration. Any species present in the equilibrated mixture with a mass fraction lower than  $Y_{th}$  were neglected. The equilibrated species mass fractions that exceeded  $Y_{th}$  and were injected into the co-flow boundary of the simulation are provided in Table 5.2.

Table 5.2: Summary of flat flame burner simulation co-flow inlet species boundary conditions. The inlet conditions are given as mass fractions following equilibration.

<b>Equiv. Ratio</b>	<b>CO</b>	<b>CO<sub>2</sub></b>	<b>H</b>	<b>H<sub>2</sub></b>	<b>H<sub>2</sub>O</b>	<b>OH</b>	<b>O<sub>2</sub></b>	<b>N<sub>2</sub></b>
1.26	5.7e-2	9.8e-2	1.1e-5	2.9e-3	1.3e-1	9.1e-3	-	7.2e-1
1.30	6.2e-2	8.8e-2	1.4e-5	3.3e-3	1.2e-1	-	2.1e-6	7.3e-1

A summary of other important boundary conditions is provided in Table 5.3 for the two co-flow equivalence cases simulated here. The co-flow velocities  $U_{cf}$  were determined from the known experimental mass flow rate  $\dot{m}_{cf}$ , the equilibrated density  $\rho_{cf}$  at the corrected temperature from the particle free case simulation, and the known co-flow area  $A_{cf}$  as

$$U_{cf} = \frac{\dot{m}_{cf}}{\rho_{cf} \cdot A_{cf}}. \quad (5.1)$$

The incident radiation field,  $G$ , needs to have boundary conditions specified by the user as well. It is omitted from Table 5.3 because the OpenFOAM built-in `MarshakRadiation` boundary condition is applied to all boundary patches listed in the table.

The fixed temperatures along the exterior wall/stack of the burner were determined from radial temperature data provided by Ma. Radial temperature profiles were provided at several axial locations. Though they did not extend to the wall itself the two most distal temperature data points were used to linearly extrapolate a temperature at the wall. That process provided a coarse wall temperature profile that was then interpolated to determine the wall temperature boundary condition.

Table 5.3: Flat flame burner simulation boundary conditions.

Field	Boundary Face	$\phi = 1.26$ B.C	$\phi = 1.30$ B.C
T [K]	Entrainment	295	295
	Co-Flow	1975	1900
	Wall	Fixed	Fixed
	Exit	Zero Grad	Zero Grad
U [m/s]	Entrainment	(1.899, 0, 0)	(1.899, 0, 0)
	Co-Flow	(2.772, 0, 0)	(2.41, 0, 0)
	Wall	No Slip	No Slip
	Exit	Zero Grad	Zero Grad
Y [-]	Entrainment	$Y_{N_2} = 1.0$	$Y_{N_2} = 1.0$
	Co-Flow	Fixed	Fixed
	Wall	Zero Grad	Zero Grad
	Exit	Zero Grad	Zero Grad
P [Pa]	Entrainment	Zero Grad	Zero Grad
	Co-Flow	Zero Grad	Zero Grad
	Wall	Zero Grad	Zero Grad
	Exit	86,000	86,000

### 5.1.2 Particle Free Comparison

The purpose of the particle free simulations was to approximate the heat loss to the burner from the co-flow and adjust the co-flow inlet temperature appropriately. Initially a simulation was performed with the adiabatic temperature that was determined from the Cantera

equilibration for the co-flow inlet. The inlet temperature was then iteratively decreased and the simulation run to convergence until good agreement was achieved between the simulation centerline temperature profile and the experimental centerline profile provided by Ma, which was measured in the absence of particles as well. The resulting centerline temperature plots for the  $\phi = 1.30$  and  $\phi = 1.26$  no particle cases are presented in Chapter 6. The co-flow inlet temperatures eventually selected as a result of this procedure for the two cases are presented in Table 5.3

### 5.1.3 Comparison with Coal Particles

The comparisons in Ma’s thesis used 6 different types of coal. Here we use the results of only two bituminous coals, the Utah Hiawatha and the Pittsburgh #8, in two different heating conditions, i.e. co-flow equivalence ratios,  $\phi = 1.26$  and  $\phi = 1.30$ , to compare experimental results to our simulation. The experimental coal loading was so low that here each computational parcel represents approximately a single physical coal particle.

Two softwares are used in this work to calculate primary devolatilization characteristics. The first is the chemical percolation devolatilization (CPD) model [11]. In Ma’s own simulations, to compare with their experiments, CPD is utilized to determine the primary devolatilization rates. Here the C3M [13] wrapper program for CPD is utilized instead of the CPD code itself. The chemical structure parameters specified by Ma are not utilized in C3M and instead a proximate and ultimate analysis is required. The proximate/ultimate analyses for both coals used here is taken from Rigby [15]. The second coal chemistry software used is PCCL [12]. The algorithms used in PCCL have been validated for modeling devolatilization and tar decomposition for bituminous coals at atmospheric pressures within the temperature ranges used here.

In addition to the proximate and ultimate analysis of the coal, the devolatilization softwares require the user to specify a heating environment. C3M/CPD only permits linear temperature trends to be specified. PCCL allows arbitrary temperature time series to be specified but in order to maintain a consistent approach the same linear temperature profile was imposed on both simulations. The appropriate temperature trends were determined

by performing preliminary CFD flow simulations while injecting particles and recording their temperatures. After a large number of particles were tracked their heating rates were averaged and analyzed to provide a linear heating profile for use in the devolatilization programs. A constant heating rate of  $85,000[K/s]$  was prescribed from an initial temperature of  $298[K]$  to a final temperature of  $1803[K]$ . This results in the entire devolatilization simulation persisting for  $1.77e^{-2}[s]$ . For the Utah Hiawatha coal simulations are performed at two different co-flow equivalence ratios,  $\phi = 1.26$  and  $\phi = 1.30$ . The particle heating profile used to determine the devolatilization temperature trend for these two cases is assumed to be the same.

For the Utah Hiawatha coal the tar yields predicted by the two CPD models only vary within a few percent and are considered to be in good agreement, see Table 5.4. The total volatile yield predictions between the two versions of CPD somewhat disagree but this does not have a large effect on the soot yields which are strongly dependent on the tar yields only. Though the heating conditions that are used for C3M are also applied for PCCL there is some disagreement in total volatile yield as well as tar yield. As is discussed in Chapter 6, this discrepancy in primary devolatilization yields is apparent in the final burner simulation results. The differences in volatile and tar yields are balanced by additional char or light gas predictions respectively.

The predictions of the same three softwares regarding Pittsburgh #8 coal are presented in Table 5.5. Here the C3M/CPD model predicts much lower tar yields than the other two. This is shown in Section 6.4 to lead to a lower soot yields that agree well with experimental data when C3M/CPD is used for devolatilization. PCCL again predicts the highest tar yield which is also reflected in the soot yield results presented later.

Table 5.4: Primary devolatilization yields for Utah Hiawatha Coal.

Code	$Y_{vol}$ (DAF)	$Y_{tar}$ (DAF)
PCCL	0.60	0.43
CPD(C3M)	0.54	0.30
CPD(Ma) [2]	0.59	0.32

Table 5.5: Primary devolatilization yields for Pittsburgh #8 Coal.

Code	$Y_{\text{vol}}$ (DAF)	$Y_{\text{tar}}$ (DAF)
PCCL	0.60	0.47
CPD(C3M)	0.53	0.31
CPD(Ma) [2]	0.61	0.37

For further coal property settings see the OpenFOAM input file `coalCloudProperties` attached in Appendix B.

The most valuable experimental information is related to the soot yield. Ma developed a system to extract the flow from the within the quartz tower and separate the soot particles from the rest of the gases. First the flow is collected and quenched by a  $25.5 [mm]$  diameter suction probe that envelopes the entire volatile gas cloud at a particular height above the burner. Then the soot and char particles are separated through two aerodynamic filters, a virtual impactor and a cyclone. Eventually the soot particles are captured in solid soot filters. With the known DAF mass flow rate of coal injection known the total soot DAF mass yield was then calculated.

In the corresponding simulations performed in this work a similar analysis is performed to enable a comparison. To perform this comparison an additional field that records the mass flux of soot  $\phi_S$  is formed from the density, velocity and soot mass fraction fields as

$$\phi_S = \mathbf{U} \cdot \rho \cdot Y_S \quad (5.2)$$

at each time step for each cell. Once the simulation has reached a pseudo converged state this field is averaged over time until the average of  $\phi_S$  itself has converged. This flux field can then be numerically integrated over a surface,  $A$ , to yield a mass flow rate over,  $\dot{m}_S$ , given by

$$\dot{m}_A = \int_S \phi_S \cdot \mathbf{n}_A dA. \quad (5.3)$$

Where  $\mathbf{n}_A$  represents the normal vector to surface  $A$ , and the ‘ $\cdot$ ’ operator represents a dot product between two vectors. The surface  $A$  is perpendicular to the central axis of the burner flow. This enables the axial soot mass flow rate  $\dot{m}_{axial}$  to be calculated as a function of the

axial location. Since the coal mass injection rate,  $\dot{m}_{coal}$  is constant we can use these axial soot mass flow rates to determine the soot yield percentage. Specifically the DAF soot yield is calculated as

$$y_S^{daf}(x) = \frac{\dot{m}_{axial}(x)}{\dot{m}_{coal}^{daf}}. \quad (5.4)$$

This enables the comparison of simulation soot yields to those determined experimentally which are recorded for a number of axial locations.

# Chapter 6

## Results

The thesis of Ma [2] provides a wide array of experimental data obtained from the BYU flat flame burner. A total of six different coals were used in three different heating conditions. Data on total soot yields is available for three of those coals in all three heating conditions. Here the results of the Utah Hiawatha and Pittsburgh #8 coal experiments in two different heating conditions are compared to simulation results. There is also a number of simulation model combinations that are investigated.

The flat flame burner experimental cases and the corresponding simulations ran in comparison are summarized in Table 6.1. First the results of the cases performed without particle injection are discussed then each subsequent section below compares the experimental and simulation results for a single coal type at a single heating condition with a variety of simulation model combinations.

Following the validation results, in Section 6.5, some additional simulation results are shown, a plot of the predicted tar mass fraction and another of the predicted soot mass fraction. These results illustrate the potential that these simulations have for predicting the location of devolatilization and soot formation.



Table 6.1: Experimental case and simulation comparison matrix. The three experimental cases investigated are Utah Hiawtha at 1800 and 1900 heating conditions, UH 1900 and UH 1800; as well as the Pittsburgh #8 coal at the 1800 heating condition, P8 1800. The simulation models used are specified by the primary devolatilization model used, CPD or PCCL and the tar decomposition model used TT, PC or PCF. When the TT tar decomposition model was employed the activation of the soot model is indicated by ‘ng’ for no soot growth reaction and g for when the soot growth reaction is considered.

<b>Case \ Models</b>	<b>CPD TT/ng</b>	<b>CPD TT/g</b>	<b>PCCL TT/ng</b>	<b>CPD PCF</b>	<b>PCCL PC</b>
<b>UH 1900</b>	X		X		X
<b>UH 1800</b>	X	X	X	X	X
<b>P8 1800</b>	X		X		

## 6.1 Particle Free Simulations

Two particle free simulations were performed, one for each of the co-flow equivalence ratios used,  $\phi = 1.26$  and  $\phi = 1.30$ . The centerline axial temperature profile results of both simulations are presented in Figures 6.1 and 6.2 respectively. The iterative process through which the appropriate co-flow inlet temperature was selected is illustrated in Figure 6.1. The adiabatic temperature calculated from the Cantera isobaric and isenthalpic equilibration simulation was taken as an initial co-flow temperature guess. That simulation is represented by the  $T_{ad} = 2086[K]$  trend in the figure which clearly results in an over prediction of the centerline temperature. The necessary heat loss correction was approximated by guessing another lower inlet temperature of  $T_{eq} = 1900[K]$ , this resulted in the under prediction illustrated. Finally a co-flow inlet temperature of  $T_{eq} = 1975[K]$  was selected and good agreement in the centerline temperature profile was found. This temperature was then used in the coal particle simulations performed at  $\phi = 1.26$ . A similar process was used to determine an appropriate temperature for the  $\phi = 1.30$  case, only the final result is shown in Figure 6.2.

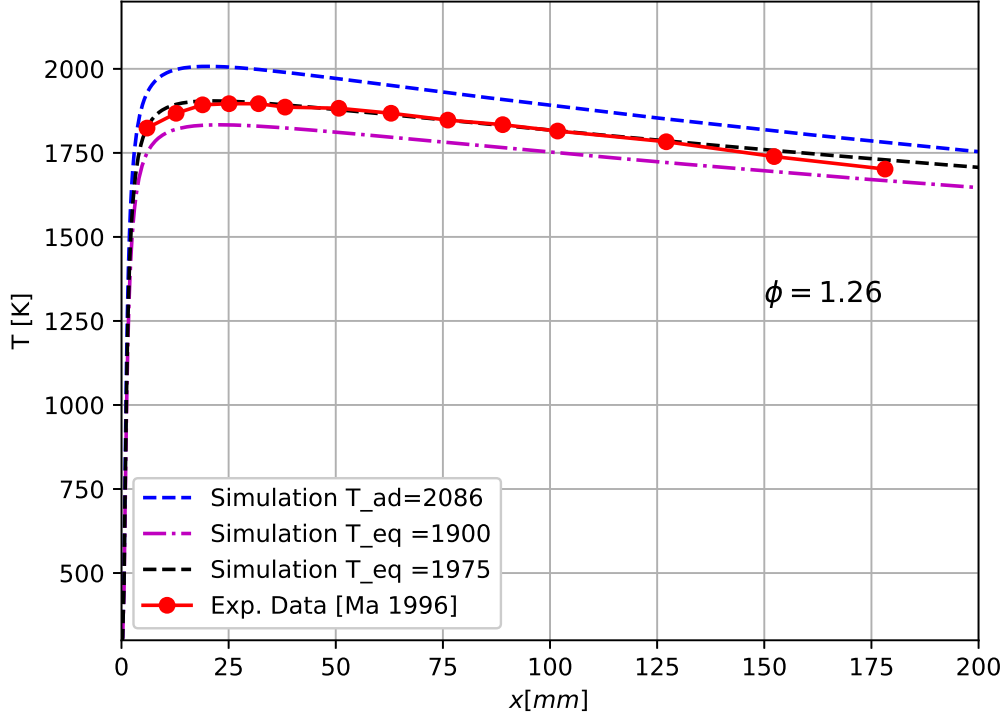


Figure 6.1: Centerline temperature plot of a particle free simulation compared to the corresponding experimental data from Ma [2] for a co-flow equivalence ratio  $\phi = 1.26$ . Temperatures are in Kelvin.

## 6.2 Utah Hiawatha with Co-flow Equivalence Ratio 1.30

See Table 5.1 for a summary of the co-flow compositions used by Ma. In this sub-section we consider the middle case with a co-flow equivalence ratio of 1.30. This is referred to in Ma's thesis as the  $T = 1800[K]$  case because that is approximately the maximum temperature reached by the particle free central axis experimental temperature profile. This equivalence ratio is more important than the other two because Brown [3, 14] also used it to validate the soot and tar decomposition models that the current work is largely based on. Therefore this data set, coupled with Brown's results, represents a useful test for the current model. We can compare with Ma's experimental results to gauge the accuracy of the model and with Brown's simulation to determine what effects the changes made in the current models have

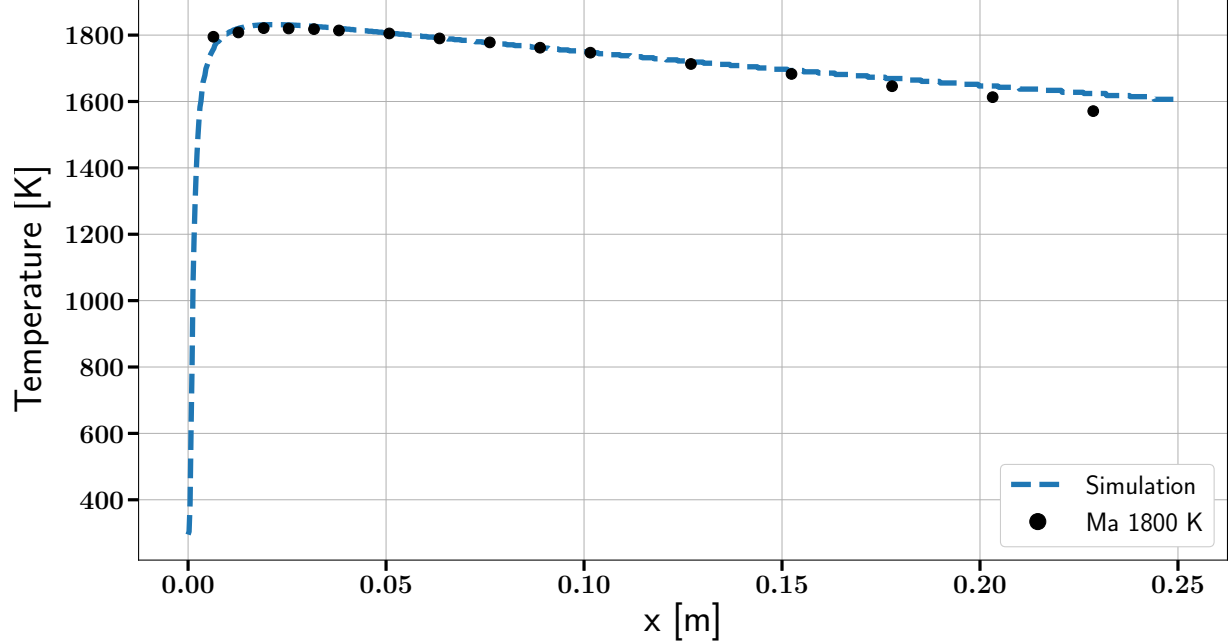


Figure 6.2: Centerline temperature plot of a particle free simulation compared to the corresponding experimental data from Ma [2] for co-flow equivalence ratio  $\phi = 1.30$ .

on the results.

First the significance of the soot growth reaction is investigated by comparing two simulations that vary only in that regard. This first result is also useful to compare the difference between results from Brown's modeling and the current model. The rest of the results in this sub-section are then separated based on the primary devolatilization model used, PCCL or CPD. The cases are divided this way because the two devolatilization models predict significantly different tar yields which directly affects the ultimate soot yield. By varying the tar decomposition models with these two groups their effect can be better understood.

The addition of a soot growth reaction from Kronenburg [37] was not expected to play a large role in these simulations. The reaction models the growth of soot particles already present in the flow through the addition of gas phase acetylene ( $C_2H_2$ ). Because the mass fraction of acetylene was low throughout the simulation domain the effect of this reaction was expected to be minimal. It is included because this framework is intended to be applicable at other experimental operating conditions where the concentrations of acetylene

may be high enough to make this soot growth mechanism relevant. In order to confirm this suspicion two simulations were performed that varied only in their inclusion of the soot growth reaction. The two otherwise identical simulations utilized CPD (via C3M) to determine primary devolatilization yields and compositions and the TT model to model tar decomposition. The soot yield results are compared to Ma's experimental results in Figure 6.3.

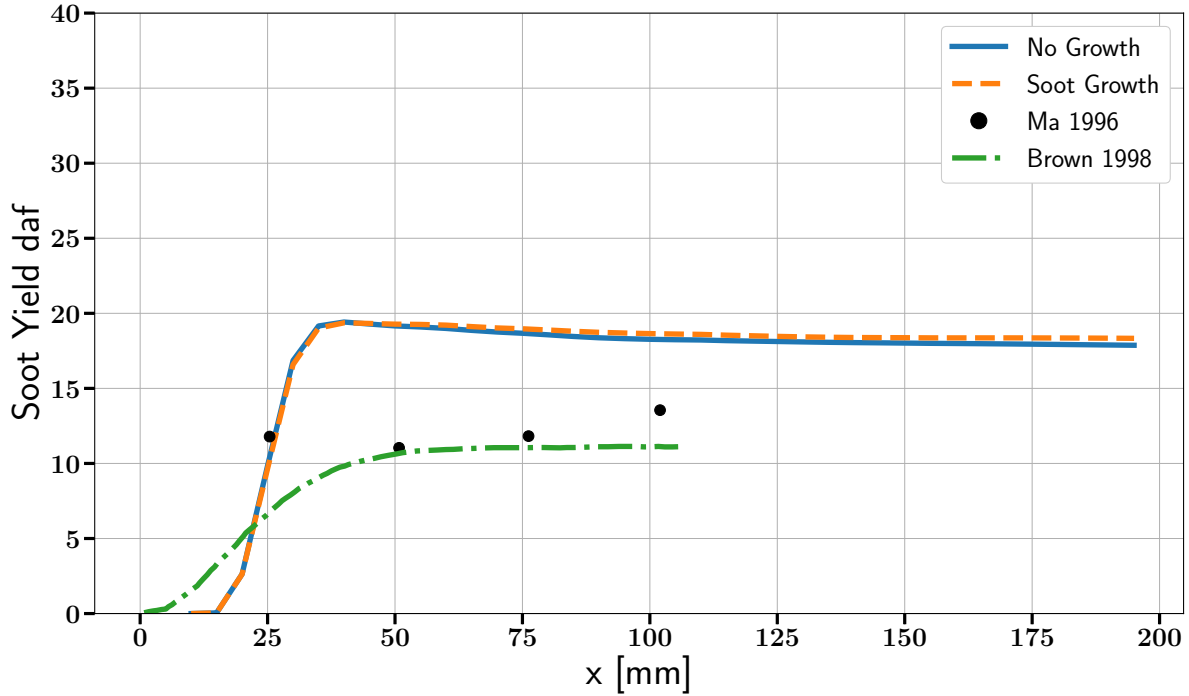


Figure 6.3: Simulated soot yield compared with experimental data, illustrating the effect of the soot growth reaction. The Utah Hiawatha coal is used at a co-flow equivalence ratio of  $\phi = 1.30$ .

As illustrated by Figure 6.3 the soot growth reaction plays a very minor role in the total soot yield profile at these operating conditions. It is therefore neglected for the rest of the presented results and only the simulation without soot growth are shown. Beyond the similarity of the two simulation results it can be seen that although slightly over predicted the simulated soot yield prediction is in relatively good agreement with the available data.

Figure 6.3 is also useful in comparing the results of our model with Brown's. The current implementation of the TT model results in different predictions. There are subtle differences

in the modeling techniques that explain this discrepancy. The TT model was developed to implement the basic modeling techniques used in Brown’s model into the OpenFOAM framework, see Section 4.3.1 for further details. Brown’s model consists primarily of three rates, tar oxidation, tar cracking and soot formation from tar breakdown. All three of these rates are included in the TT model and the rate constants used are taken directly from Brown’s papers.

The discrepancy in the results between the two simulations can be explained by two factors of the simulation that indirectly affect the tar decomposition model. First, the computational meshes used are very different. Though Brown’s simulation models the entire 3-D burner domain the mesh resolution is very course. Only 2-3 cells were used to represent the coal entrainment inlet. This lead to the particles, and entrainment gas, experiencing a different heating environment than they do in the current simulation. All three of the tar decomposition rates depend strongly on temperature and so even with the same rate equations the reactions will progress differently in different heating environments.

Second, our simulations are performed transiently while Brown’s were performed in a steady state fashion. This lead to the parcels in each simulation again experiencing different heating environments which leads ultimately to different soot yields. The difference in these two approaches is discussed in more detail in Section 6.5.

Two tar decomposition models were coupled with the C3M/CPD primary devolatilization, the TT and the PCF models. The results of those simulations are presented in Figure 6.4. These results illustrate that even with the same primary devolatilization characteristics the soot yields can vary widely. The only difference between the two simulations that lead to the results pictured is their tar gasification and soot formation rate constants.

The PCF decomposition model predicts much higher soot yields than the other tar decomposition models. Figure 6.4 shows that it predicts a much higher soot yield than the normal TT model and its shown below in Figure 6.7 that it also predicts higher yields than the PC model, even with the same devolatilization.

The high soot yield predictions of the PCF model can be explained by considering the context of the model’s formulation as described in Section 4.3.3. The PCF model uses the

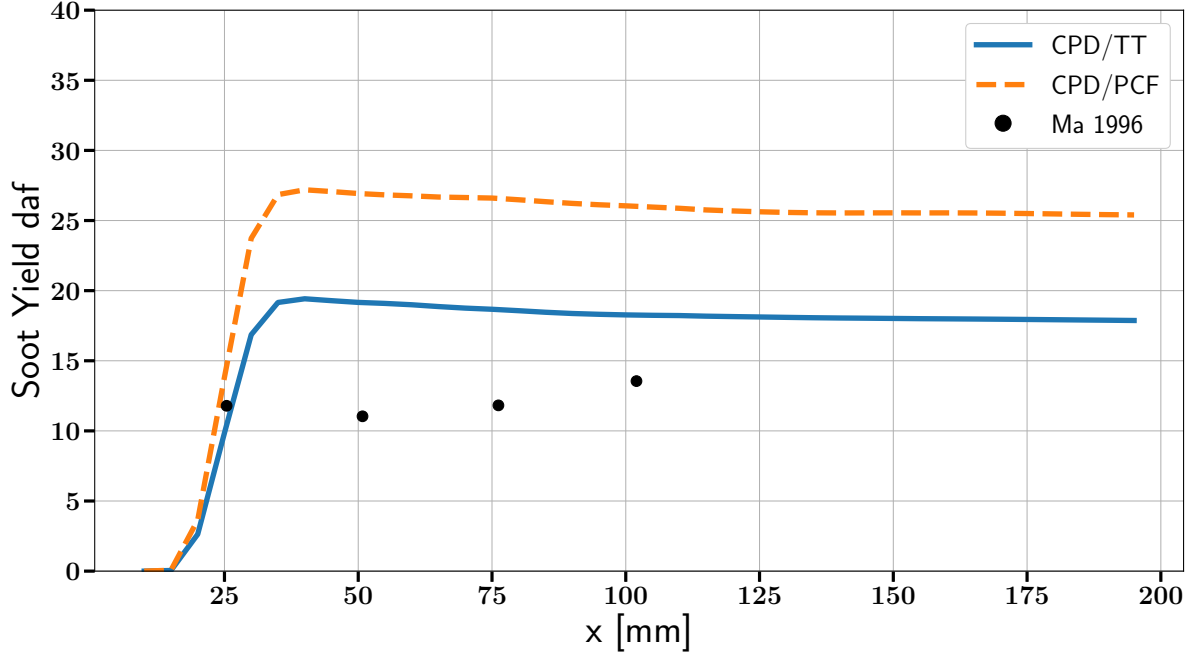


Figure 6.4: Simulated soot yield compared with experimental data with the TT and PCF model both utilizing the CPD model for primary devolatilization. The Utah Hiawatha coal is used at a co-flow equivalence ratio of  $\phi = 1.30$ .

same three tar decomposition reactions as the TT model but the rate constants are determined by fitting predicted soot yields to PCCL tar decomposition predictions. The PCCL simulation used to fit the PCF model rate constants was the same that was used to calculate inputs for the other PCCL reliant simulations, e.g. the PCCL/PC model combination. But PCCL provides several outputs regarding tar decomposition and different outputs are used for fitting the PCF model than are used in the PC model. While the output used for the PC model specifies a mass based breakdown of tar into light gases and soot that remains constant with temperature, the output used for the PCF model gives time series of light gases and soot evolved to form a zero dimensional reactor that approximates the environment surrounding the particle. These time series are strongly dependent on the heating environment specified in PCCL inputs.

Figure 6.5 illustrates the mass fraction time series for tar and the tar decomposition products, i.e. soot and light gases, referred to as 'PCCL secondary gases' in the figure. In this particular PCCL simulation the light gases resulting from tar cracking are formed much

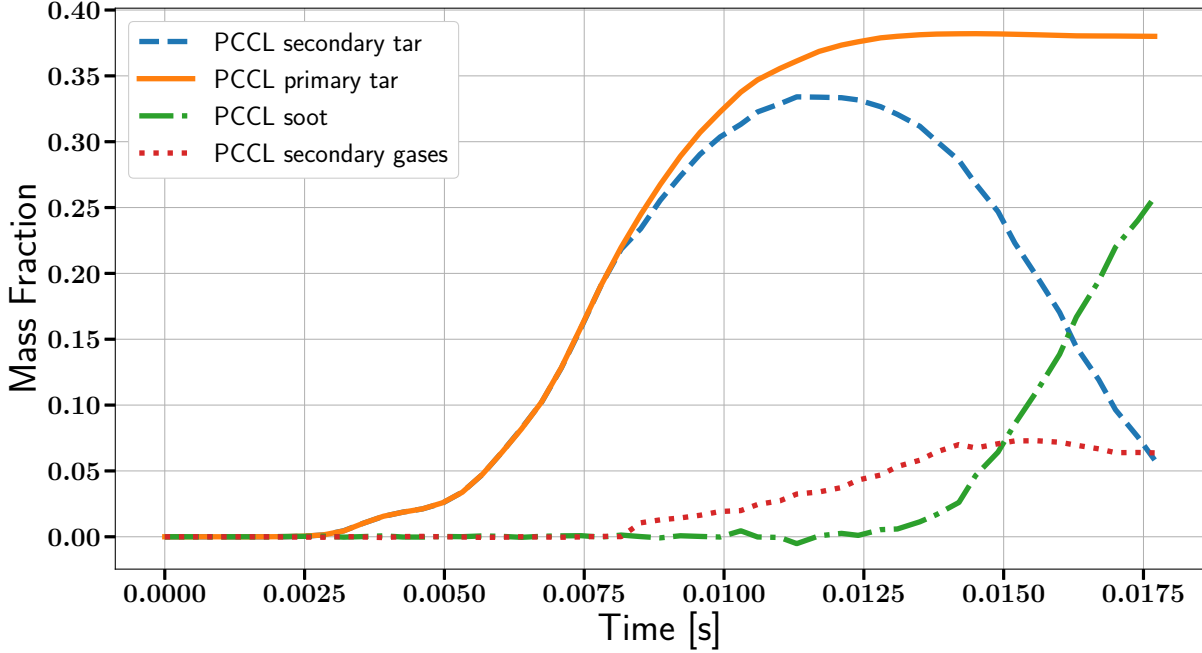


Figure 6.5: Mass fractions of primary tar, secondary tar, soot and secondary gases in the zero dimensional reactor representing the particle environment.

earlier than the soot. When the PCF fits rate constants to these trends the level profile of the light gas trend in Figure 6.5 forces the rates to become low at the later simulation times. Since a linear heating profile was prescribed in PCCL these later simulation times correspond to the high end of the temperature range used,  $298 - 1803[K]$ . The temperature dependence of the soot formation and tar cracking rates using rate constants determined by the PCF are compared with rates that use the constants determined by Ma in Figure 6.6. This illustrates that beyond  $\approx 1500[K]$  the soot formation rate determined by the PCF will overpower the tar cracking rate.

This becomes a problem in the CFD simulation because the heating profile experienced by the tar is not linear and the majority of tar decomposition occurs at high temperatures. Instead of integrating the rates over the entire particle temperature range used in PCCL the tar is instead subjected to the higher gas temperature, albeit somewhat attenuated by the particle's presence, of the flow during its decomposition. This decomposition at high temperatures results in the soot formation reaction being over represented and a larger

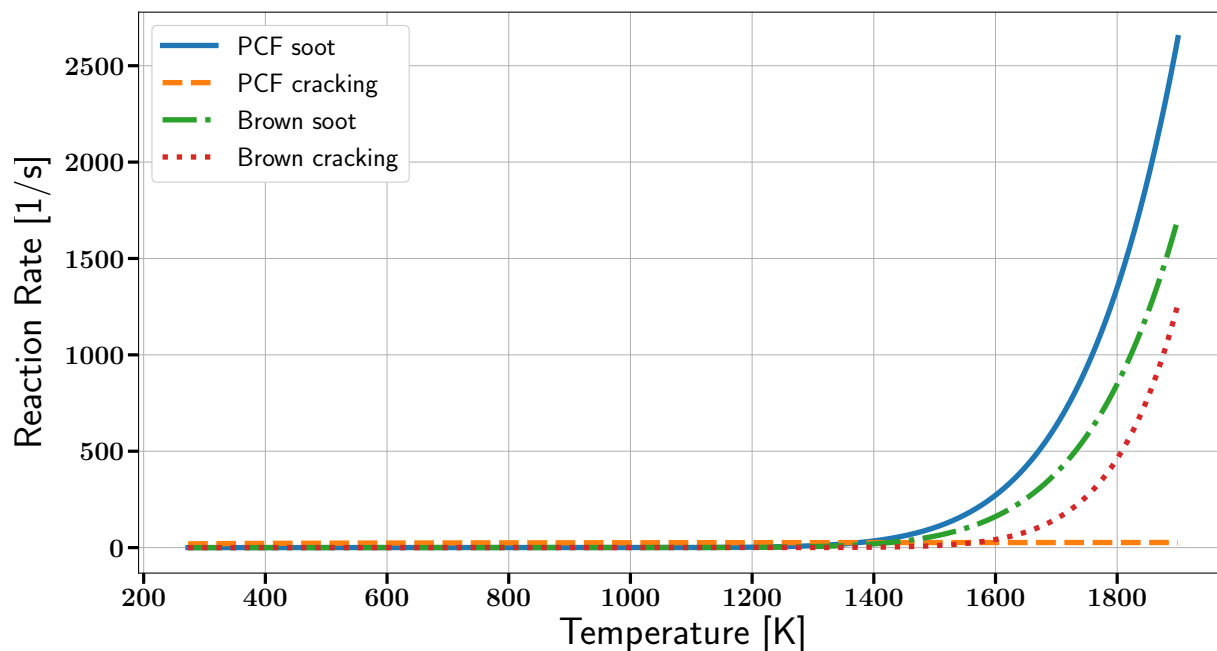


Figure 6.6: Comparison of the Arrhenius rates determined with the PCF to those from Brown and Ma [2,3]

fraction of tar being converted to soot, as opposed to cracked into light gas, than should be. If the heating trend used for PCCL were a better match for the heating trend experienced by the tar in the CFD simulations then the correct proportions may be predicted. This and some other potential solutions for this discrepancy are discussed in Chapter 7.

Three different tar decomposition models are coupled with the PCCL primary devolatilization model, they are the TT, PCF and PC models. The predicted soot yield results of these three simulations are compared to experimental results in Figure 6.7.

Devolatilization yields are a strong predictor of the soot yield which is evident when Figures 6.4 and 6.7 are compared. When more tar is predicted it directly affects how much soot will be produced. From Table 5.4 it is clear that the PCCL model predicts much more tar release than the CPD model does for Utah Hiawatha at this co-flow equivalence ratio,  $\phi = 1.30$ . This corresponds to the ultimately higher soot yields shown in Figure 6.7.

The strong relationship between tar yield and soot yield was exacerbated in the flow conditions of these experiments/simulations. First the co-flow is itself rich and therefore



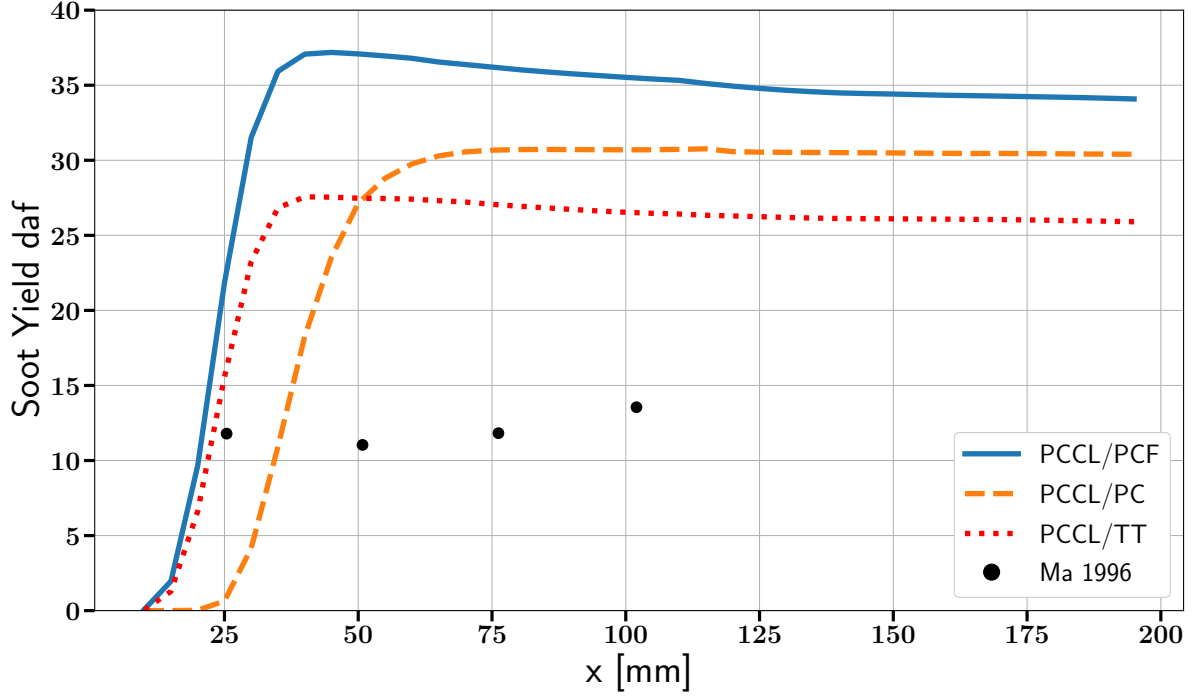


Figure 6.7: Simulated soot yield compared with experimental data with the TT, PC and PCF model utilizing the PCCL model for primary devolatilization. The Utah Hiawatha coal is used at a co-flow equivalence ratio of  $\phi = 1.30$ .

deprived of oxygen. The global equivalence ratio is only increased by the addition of the coal derived gaseous fuels, including tar. This prevents any significant tar oxidation, which has the potential to decrease soot formation by competitively consuming tar, from occurring.

Figure 6.7 also shows that when the PC decomposition model is used the onset of soot formation is delayed. This is caused by the retention of tar within the coal particle. The particles are almost always cooler than the surrounding gas and the rates for both soot formation and tar cracking are therefore decreased.

Finally Figures 6.3, 6.4 and 6.7 suggest that soot gasification is present regardless of the tar decomposition model used. Its presence is indicated by the slow decrease in soot yield with increasing axial location. This conclusion is corroborated by Figure 6.8 which shows a contour plot of the reaction rate for  $CO_2$  gasification for the CPD/TT case.

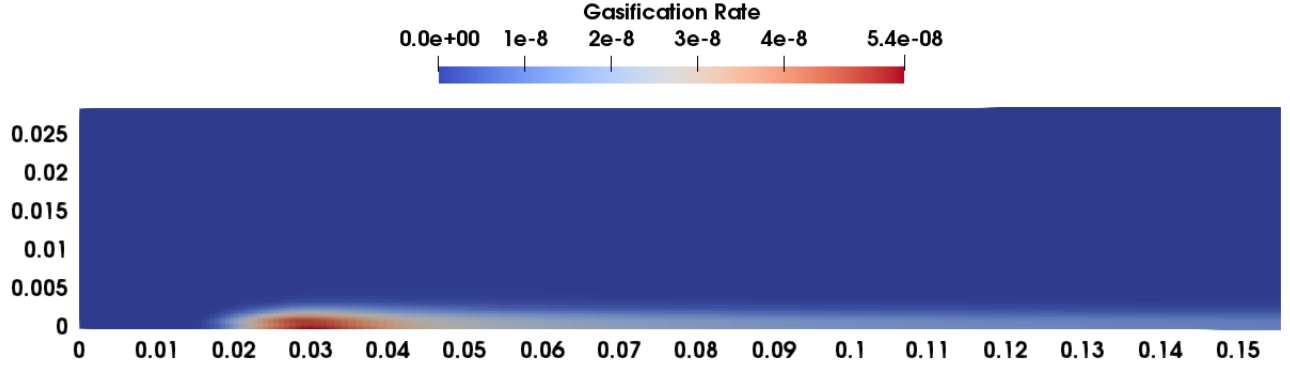


Figure 6.8: Soot gasification rate  $[kmol/(m^3s)]$  with  $CO_2$  for the CPD/TT model simulation case without soot growth. Pictured is the central plane of the simulation domain. The bottom axis is aligned with the central axis of the flow and the vertical axis represents radial displacement, both are in units of  $[m]$ .

### 6.3 Utah Hiawatha Coal with Co-flow Equivalence Ratio 1.26

The experimental data for the Utah Hiawatha coal taken with a co-flow equivalence ratio of 1.26 is also compared against simulation results. Three different model combinations are used for the comparisons. There are not any reported simulation results from Brown at these operating conditions. The results are presented in Figure 6.9. The results are very similar to those for the Utah Hiawatha  $\phi = 1.30$  case and illustrate the same trends.

### 6.4 Pittsburgh # 8 Coal with Co-flow Equivalence Ratio 1.30

To investigate the effect of different coal characteristics on the devolatilization models two simulations of the Pittsburgh # 8 coal run at a co-flow equivalence ratio of  $\phi = 1.30$  were performed. Ma performed the flat flame burner experiments for this coal and Brown simulated the flow as well which makes this another very useful test case. The co-flow heat loss for this case is the same as the  $\phi = 1.30$  Utah Hiawatha case.

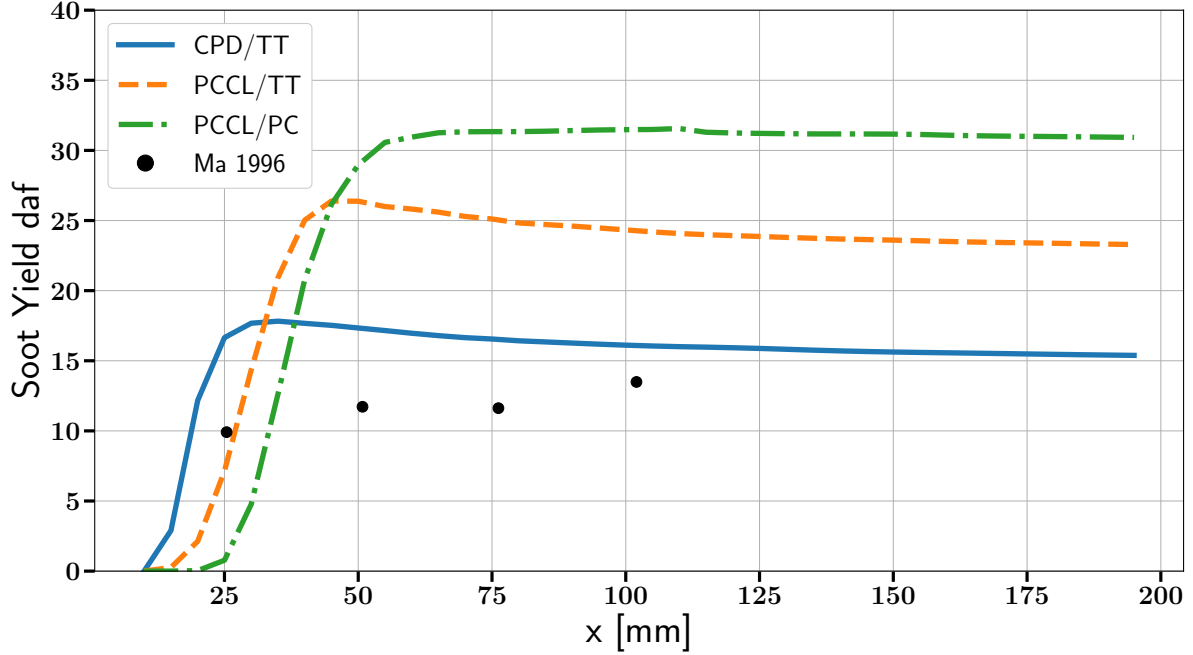


Figure 6.9: Simulated soot yield compared with experimental data for Utah Hiawatha coal at a co-flow equivalence ratio of  $\phi = 1.26$ .

This case was selected because it was the one that Brown’s model performed the most poorly on. In this case the CPD/TT model performs similarly to Brown’s. The comparison of these three simulation results reinforces the finding that properly predicting devolatilization is very important. As discussed above in Section 6.2 the TT model predicts higher soot formation than Brown’s model even though the rates used are the same. In this case the difference in soot production is countered by an opposing difference in tar yield predictions for the two cases. Table 5.5 shows that the DAF tar yield differs between C3M/CPD and the version of CPD used by Brown by 6%. This again illustrates the sensitivity of the soot yield results to devolatilization predictions.

The PCCL/TT simulation provides an even more extreme example of this trend. When compared to the CPD/TT simulation the effect of high tar yield can be seen clearly. Table 5.5 shows PCCL predicting 16% DAF higher tar yield than C3M/CPD. When the same tar decomposition model is used this results in a  $\approx 12\%$  difference in DAF soot yield.

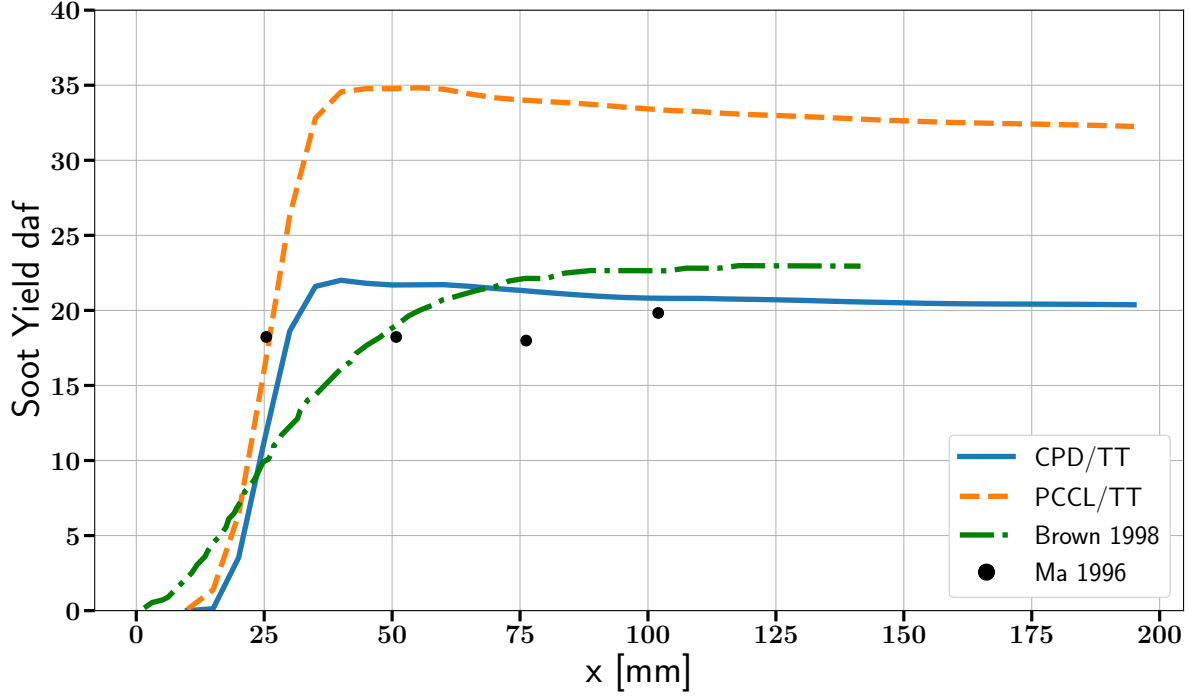


Figure 6.10: Simulated soot yield compared with experimental data for Pittsburgh #8 coal at a co-flow equivalence ratio of  $\phi = 1.30$ .

## 6.5 Tar and Soot Mass Fraction Predictions

Figures 6.11 and 6.12 illustrate particle mass loss due to devolatilization. The vertical axis of both plots aligns with the burner surface of the simulation. The horizontal axis is aligned with the central axis of the simulated flow. In both figures the spheres represent individual parcels and their color indicates their solid particle fraction. The solid particle fraction is the mass fraction of the particle composed by char and ash, in contrast to liquid water or mass that is to be released as volatiles.

In Figure 6.11 the presence of devolatilization is indicated in two ways. First the solid particle fraction increases from  $\approx 40\%$  to nearly  $100\%$ , which is the expected value upon the completion of evaporation and devolatilization. Second the color map of the gas phase indicates the tar mass fraction and shows a cloud of tar forming around the parcel. In the figure the tar cloud that forms around a parcel rapidly diffuses from the parcel and is consumed. This shows how rapidly the processes of soot formation and tar cracking occurs.

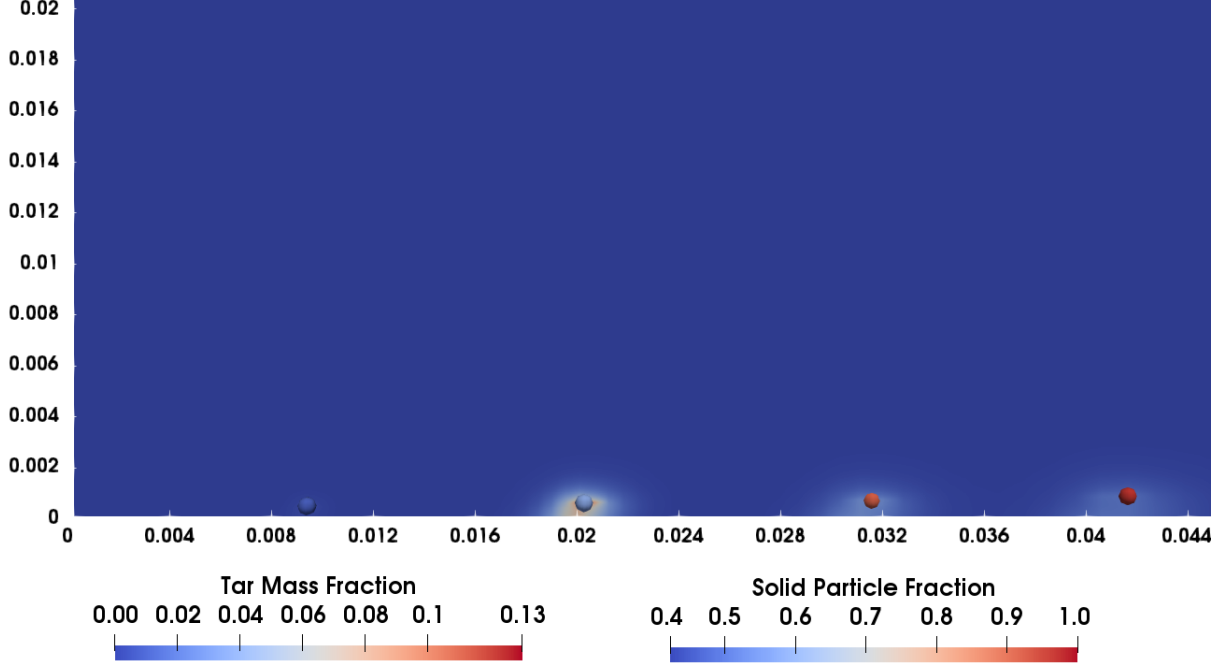


Figure 6.11: Simulated tar mass fraction and solid particle fraction. This is the result of a simulation performed with the PCCL/TT model combination with the  $\phi = 1.30$  co-flow equivalence ratio. The unit of the axes is meters.

Figure 6.12 is a result from the same timestep as Figure 6.11 but it shows the soot mass fraction within the gas phase rather than the tar mass fraction. It corroborates the claim that tar is rapidly converted to soot by showing a soot cloud forming as the tar is consumed. This plot also shows how important transient modeling is in these dispersed particle flows. The considerable thermal mass of the parcels significantly decreases the temperature of the gas that surrounds them. Since the conversion of tar to soot is a temperature driven process this cooler environment surrounding the parcels delays soot formation. Once the tar diffuses farther from the parcels, into regions of the flow that are unaffected by the parcels presence, then soot is formed more rapidly.

The transient effect that parcels have on their immediate gas environment is captured by a transient simulation and is neglected when a steady state approach is adopted. In steady state solutions parcels are evolved over an averaged field. In flows with higher particle loadings this effect is less important; the sources of many different particles within each cell

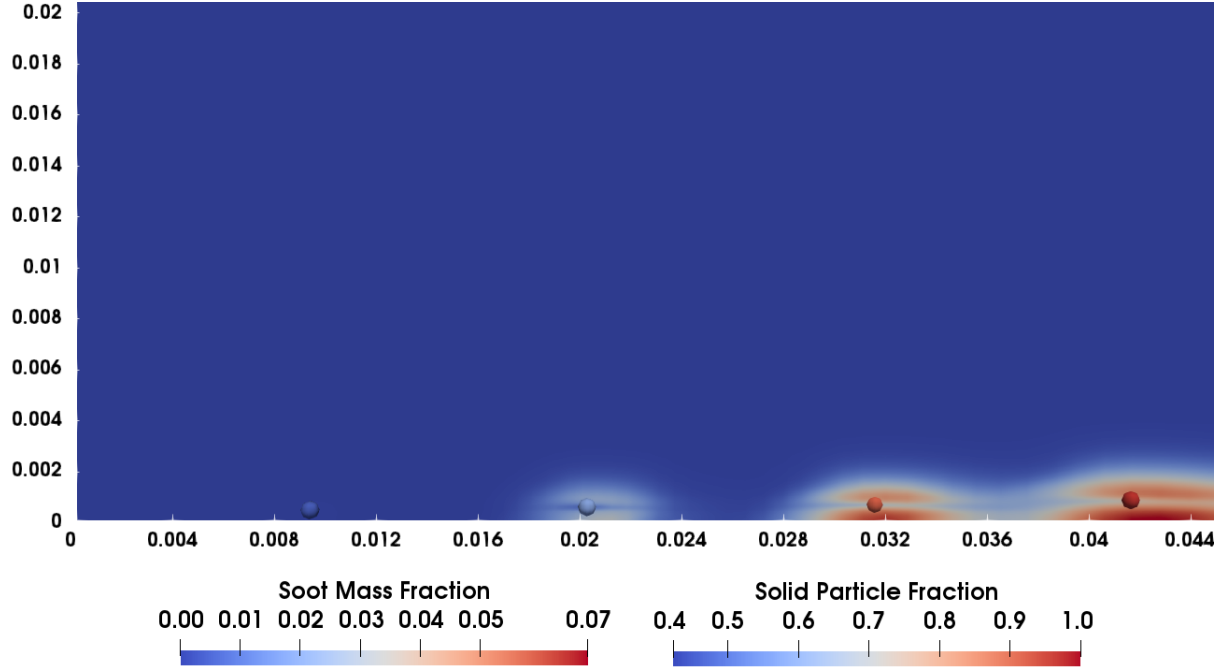


Figure 6.12: Simulated soot mass fraction and solid particle fraction. This is the result of a simulation performed with the PCCL/TT model combination with the  $\phi = 1.30$  co-flow equivalence ratio. The unit of the axes is meters.

physically produce an averaged field and it makes sense to model it as such. Where particles are instead very dispersed, as in the experiment considered here, capturing the evolving local environment of each parcel is important and evolving them over an averaged gas field leads to parcel processes, e.g. devolatilization, potentially occurring very differently.

# Chapter 7

## Conclusions and Future Work

Two standalone devolatilization submodels, the `nthOrderDevolatilization` and the `analyticalSFORDevolatilization` models, as well as a third devolatilization submodel that is incorporated into the PC tar decomposition model; one soot submodel, the Two Equation soot model; and two tar decomposition submodels, the TT model and the PC model, have been implemented in OpenFOAM . Additionally a novel framework for utilizing PCCL as a virtual experiment to fit rate constants in the TT tar decomposition model, the PCF, has been developed and implemented. The submodels rely on the built-in functionality of OpenFOAM to provide a complete chemical and energetic coupling between the main transport equations and the submodels. This effort provides a framework to include detailed tar and soot models, less based in empiricism than previous efforts, in large scale transient computational fluid dynamic simulations of multiphase reactive pulverized coal flows.

The modeling was validated against experimental results from the BYU laminar flat flame burner performed by Ma [2] as well as previous computational results, upon which much of the current work is based, using very similar methods from Brown [14]. The current simulation soot yield results are found to be in relatively good agreement with both previous simulation results and experiments. The importance of accurate primary devolatilization data is illustrated throughout the results. Regardless of the complexity and care taken in modeling soot and tar consumption the soot yields are very strongly dependent on the predicted tar and volatile yields from the coal particles. Furthermore it is shown that in low

particle loading experiments like the one considered here, simulations must be performed in a transient fashion to capture the localized effects of particles.

Of the three devolatilization models implemented in this work two, the `nthOrderDevolatilization` model and the devolatilization model included within the PC tar decomposition model, utilize PCCL to determine rate constants and yields, the remaining devolatilization model, the `analyticalSFORDevolatilization` model, uses rates determined by CPD. Generally the simulations that use the `analyticalSFORDevolatilization` model, and thus CPD, are in better agreement with soot yield data from both Ma’s and Brown’s findings.

This superior agreement is not surprising, at least when the TT model is employed to predict tar decomposition. The rates for the TT model are taken directly from Ma’s work which utilized CPD to predict devolatilization and then optimized the tar decomposition rates to fit soot yield data. If different devolatilization data were used, e.g. from PCCL, it would still be possible to tune tar decomposition rates to match experimental soot yields. In this context it is not surprising that using the TT tar decomposition model in conjunction with devolatilization characteristics predicted by PCCL, which differ from those predicted by CPD, leads to poorer agreement.

Furthermore since only one validation experiment is considered here our conclusions rely entirely on the accuracy of Ma’s measurements. Other experimental studies, that were not readily amenable to CFD simulations, account more fully for the conservation of mass and species and report higher tar and soot yields than are measured by Ma. A good survey of these experiments is provided by Niksa [45]. If these experiments were modeled they may show that PCCL outperforms CPD devolatilization predictions.

The PCF was developed to avoid some of the issues inherent in the design of the PC model. The results of simulations using the PCF were still found to be in poor agreement with experiments. This poor agreement is largely caused by an inability to accurately represent the heating environment experienced by tar in the CFD simulations with PCCL. This, in turn, lead to an over representation of soot formation from tar and a corresponding under prediction in tar cracking to light gases. These issues are discussed further in Section 6.2



and some possible steps forward are explained later in this section.

The PC model also represents a consistent approach, i.e. it uses PCCL for both devolatilization and tar decomposition predictions. The way in which PCCL calculates tar decomposition requires a discrete mass of tar to be considered. This paradigm does not easily fit into CFD simulations and requires the tar mass to be retained within the coal particle after its devolatilization. This retention limits the temperature and diffusion of the tar during its decomposition leading to inaccurate tar and ultimately soot yield predictions.

The TT tar decomposition model is based on the previous modeling work by Ma and Brown. In contrast to the PC model the tar is treated as a gas phase species which is much more conducive to CFD modeling. The rates used in the model were determined by Ma to force a match between one dimensional simulation and experimental soot yield results from the BYU flat flame burner. The same rates were used later by Brown in a three dimensional simulation of the same burner. Excellent agreement with experiments was found across a variety of coal types and heating experiments in both of the prior studies. When applied within the current framework only fair agreement was found. The fair agreement here is likely caused by modeling differences between this and previous studies. Most notably the mesh used here is much more refined than in Brown's work which lead to different temperature profiles and thus coal particle heating environments. This and other reasons are discussed further in Section 6.2.

Going forward, focus should be placed on tar decomposition models that are formulated in line with the TT model rather than the PC model. The inherent modeling flaws of the PC model limit its applicability such that even if the predictive powers offered by PCCL could be suitably improved the model does not warrant further investment. The TT model is versatile and future work should focus on finding appropriate rate constants for it.

There are two potential pathways forward in improving the TT model. First the work of Ma can be replicated. The same flat flame burner experimental results can be used to find the optimal rate constants in the TT model. This approach represents a new challenge because the time requirements to simulate the flat flame burner flow are not trivial; Ma used a one dimensional simulation that was able to quickly indicate the suitability of a particular

rate constants set.

The other possible pathway to improve the TT model relies on the PCF. The current limitations stem from an inability to fully utilize an important feature of PCCL. It should be possible, according to the PCCL documentation, to prescribe a heating rate for the tar decomposition simulation that differs from that used in the coal devolatilization simulation. Currently the same heating profile is used for both, i.e. the tar is decomposed with the same temperature history that the particle experiences. While the documentation does suggest this arrangement for a flow reactor, as is used here, in contrast to e.g. a fixed bed reactor, it is not clear that it is appropriate for present case. The co-flow that heats the particles often remains  $100 - 200[K]$  hotter than the particles themselves. Physically the tar will devolatilize and diffuse into this hotter surrounding gas, thus experiencing a much different heating profile than the particles. Although this may lead to higher soot yields since soot formation is a temperature driven process it is possible that by treating the tar with a more realistic temperature history the cracking rates at higher temperatures will also be increased.

It is expected that using the results of a PCCL simulation with a more physical tar decomposition heating profile may mitigate some of the issues currently affecting the PCF discussed above and described in more detail in Section 6.2. As a first attempt a constant temperature profile of  $1700[K]$  was prescribed for the tar decomposition simulation while the coal devolatilization simulation used the same linear temperature profile as before. The PCCL simulation failed to run to completion at these and a variety of related, but similar, heating profiles. If PCCL could be run successfully at these conditions it is expected that the results of the tar decomposition simulation would be more relevant at the higher temperatures experienced by the tar in the simulation and would therefore avoid the issues discussed previously that result in poor PCF performance.

# Appendix A

## DRM-22 Mechanism

### A.1 Kinetics

[illegible]

O+CH2<=>H+HCO	8.000E+13	0.000	0.00
O+CH2(S)<=>H+HCO	1.500E+13	0.000	0.00
O+CH3<=>H+CH2O	8.430E+13	0.000	0.00
O+CH4<=>OH+CH3	1.020E+09	1.500	8600.00
O+CO+M<=>CO2+M	6.020E+14	0.000	3000.00
H2/2.00/ O2/6.00/ H2O/6.00/ CH4/2.00/ CO/1.50/ CO2/3.50/ C2H6/3.00/ AR/0.50/			
O+HCO<=>OH+CO	3.000E+13	0.000	0.00
O+HCO<=>H+CO2	3.000E+13	0.000	0.00
O+CH2O<=>OH+HCO	3.900E+13	0.000	3540.00
O+C2H2<=>CH2(S)+CO	1.020E+07	2.000	1900.00
O+C2H2<=>CO+CH2	1.020E+07	2.000	1900.00
O+C2H4<=>CH3+HCO	1.920E+07	1.830	220.00
O+C2H5<=>CH3+CH2O	1.320E+14	0.000	0.00
O+C2H6<=>OH+C2H5	8.980E+07	1.920	5690.00
O2+CO<=>O+CO2	2.500E+12	0.000	47800.00
O2+CH2O<=>HO2+HCO	1.000E+14	0.000	40000.00
H+O2+M<=>HO2+M	2.800E+18	-0.860	0.00
O2/0.00/ H2O/0.00/ CO/0.75/ CO2/1.50/ C2H6/1.50/ N2/0.00/ AR/0.00/			
H+2O2<=>HO2+O2	3.000E+20	-1.720	0.00
H+O2+H2O<=>HO2+H2O	9.380E+18	-0.760	0.00
H+O2+N2<=>HO2+N2	3.750E+20	-1.720	0.00
H+O2+AR<=>HO2+AR	7.000E+17	-0.800	0.00
H+O2<=>O+OH	8.300E+13	0.000	14413.00
2H+M<=>H2+M	1.000E+18	-1.000	0.00
H2/0.00/ H2O/0.00/ CH4/2.00/ CO2/0.00/ C2H6/3.00/ AR/0.63/			
2H+H2<=>2H2	9.000E+16	-0.600	0.00
2H+H2O<=>H2+H2O	6.000E+19	-1.250	0.00
2H+CO2<=>H2+CO2	5.500E+20	-2.000	0.00
H+OH+M<=>H2O+M	2.200E+22	-2.000	0.00
H2/0.73/ H2O/3.65/ CH4/2.00/ C2H6/3.00/ AR/0.38/			
H+HO2<=>O2+H2	2.800E+13	0.000	1068.00

H+H <sub>2</sub> O <sub>2</sub> <=>2OH	1.340E+14	0.000	635.00
H+H <sub>2</sub> O <sub>2</sub> <=>H <sub>2</sub> O+H <sub>2</sub>	1.210E+07	2.000	5200.00
H+CH <sub>2</sub> (+M)<=>CH <sub>3</sub> (+M)	2.500E+16	-0.800	0.00
LOW / 3.200E+27 -3.140 1230.00/			
TR0E/ 0.6800 78.00 1995.00 5590.00 /			
H <sub>2</sub> /2.00/ H <sub>2</sub> O/6.00/ CH <sub>4</sub> /2.00/ CO/1.50/ CO <sub>2</sub> /2.00/ C <sub>2</sub> H <sub>6</sub> /3.00/ AR/0.70/			
H+CH <sub>3</sub> (+M)<=>CH <sub>4</sub> (+M)	1.270E+16	-0.630	383.00
LOW / 2.477E+33 -4.760 2440.00/			
TR0E/ 0.7830 74.00 2941.00 6964.00 /			
H <sub>2</sub> /2.00/ H <sub>2</sub> O/6.00/ CH <sub>4</sub> /2.00/ CO/1.50/ CO <sub>2</sub> /2.00/ C <sub>2</sub> H <sub>6</sub> /3.00/ AR/0.70/			
H+CH <sub>4</sub> <=>CH <sub>3</sub> +H <sub>2</sub>	6.600E+08	1.620	10840.00
H+HCO(+M)<=>CH <sub>2</sub> O(+M)	1.090E+12	0.480	-260.00
LOW / 1.350E+24 -2.570 1425.00/			
TR0E/ 0.7824 271.00 2755.00 6570.00 /			
H <sub>2</sub> /2.00/ H <sub>2</sub> O/6.00/ CH <sub>4</sub> /2.00/ CO/1.50/ CO <sub>2</sub> /2.00/ C <sub>2</sub> H <sub>6</sub> /3.00/ AR/0.70/			
H+HCO<=>H <sub>2</sub> +CO	7.340E+13	0.000	0.00
H+CH <sub>2</sub> O(+M)<=>CH <sub>3</sub> O(+M)	5.400E+11	0.454	2600.00
LOW / 2.200E+30 -4.800 5560.00/			
TR0E/ 0.7580 94.00 1555.00 4200.00 /			
H <sub>2</sub> /2.00/ H <sub>2</sub> O/6.00/ CH <sub>4</sub> /2.00/ CO/1.50/ CO <sub>2</sub> /2.00/ C <sub>2</sub> H <sub>6</sub> /3.00/			
H+CH <sub>2</sub> O<=>HCO+H <sub>2</sub>	2.300E+10	1.050	3275.00
H+CH <sub>3</sub> O<=>OH+CH <sub>3</sub>	3.200E+13	0.000	0.00
H+C <sub>2</sub> H <sub>2</sub> (+M)<=>C <sub>2</sub> H <sub>3</sub> (+M)	5.600E+12	0.000	2400.00
LOW / 3.800E+40 -7.270 7220.00/			
TR0E/ 0.7507 98.50 1302.00 4167.00 /			
H <sub>2</sub> /2.00/ H <sub>2</sub> O/6.00/ CH <sub>4</sub> /2.00/ CO/1.50/ CO <sub>2</sub> /2.00/ C <sub>2</sub> H <sub>6</sub> /3.00/ AR/0.70/			
H+C <sub>2</sub> H <sub>3</sub> (+M)<=>C <sub>2</sub> H <sub>4</sub> (+M)	6.080E+12	0.270	280.00
LOW / 1.400E+30 -3.860 3320.00/			
TR0E/ 0.7820 207.50 2663.00 6095.00 /			
H <sub>2</sub> /2.00/ H <sub>2</sub> O/6.00/ CH <sub>4</sub> /2.00/ CO/1.50/ CO <sub>2</sub> /2.00/ C <sub>2</sub> H <sub>6</sub> /3.00/ AR/0.70/			
H+C <sub>2</sub> H <sub>3</sub> <=>H <sub>2</sub> +C <sub>2</sub> H <sub>2</sub>	3.000E+13	0.000	0.00

H+C2H4(+M)<=>C2H5(+M)	1.080E+12	0.454	1820.00
LOW / 1.200E+42 -7.620 6970.00/			
TROE/ 0.9753 210.00 984.00 4374.00 /			
H2/2.00/ H2O/6.00/ CH4/2.00/ CO/1.50/ CO2/2.00/ C2H6/3.00/ AR/0.70/			
H+C2H4<=>C2H3+H2	1.325E+06	2.530	12240.00
H+C2H5(+M)<=>C2H6(+M)	5.210E+17	-0.990	1580.00
LOW / 1.990E+41 -7.080 6685.00/			
TROE/ 0.8422 125.00 2219.00 6882.00 /			
H2/2.00/ H2O/6.00/ CH4/2.00/ CO/1.50/ CO2/2.00/ C2H6/3.00/ AR/0.70/			
H+C2H6<=>C2H5+H2	1.150E+08	1.900	7530.00
H2+CO(+M)<=>CH2O(+M)	4.300E+07	1.500	79600.00
LOW / 5.070E+27 -3.420 84350.00/			
TROE/ 0.9320 197.00 1540.00 10300.00 /			
H2/2.00/ H2O/6.00/ CH4/2.00/ CO/1.50/ CO2/2.00/ C2H6/3.00/ AR/0.70/			
OH+H2<=>H+H2O	2.160E+08	1.510	3430.00
2OH(+M)<=>H2O2(+M)	7.400E+13	-0.370	0.00
LOW / 2.300E+18 -0.900 -1700.00/			
TROE/ 0.7346 94.00 1756.00 5182.00 /			
H2/2.00/ H2O/6.00/ CH4/2.00/ CO/1.50/ CO2/2.00/ C2H6/3.00/ AR/0.70/			
2OH<=>O+H2O	3.570E+04	2.400	-2110.00
OH+HO2<=>O2+H2O	2.900E+13	0.000	-500.00
OH+H2O2<=>H2O+H2O	5.800E+14	0.000	9560.00
OH+CH2<=>H+CH2O	2.000E+13	0.000	0.00
OH+CH2(S)<=>H+CH2O	3.000E+13	0.000	0.00
OH+CH3<=>CH2+H2O	5.600E+07	1.600	5420.00
OH+CH3<=>CH2(S)+H2O	2.501E+13	0.000	0.00
OH+CH4<=>CH3+H2O	1.000E+08	1.600	3120.00
OH+CO<=>H+CO2	4.760E+07	1.228	70.00
OH+HCO<=>H2O+CO	5.000E+13	0.000	0.00
OH+CH2O<=>HCO+H2O	3.430E+09	1.180	-447.00
OH+C2H2<=>CH3+CO	4.830E-04	4.000	-2000.00

OH+C2H3<=>H2O+C2H2	5.000E+12	0.000	0.00
OH+C2H4<=>C2H3+H2O	3.600E+06	2.000	2500.00
OH+C2H6<=>C2H5+H2O	3.540E+06	2.120	870.00
2H2O<=>O2+H2O2	1.300E+11	0.000	-1630.00
DUPLICATE			
2H2O<=>O2+H2O2	4.200E+14	0.000	12000.00
DUPLICATE			
H2O+CH2<=>OH+CH2O	2.000E+13	0.000	0.00
H2O+CH3<=>O2+CH4	1.000E+12	0.000	0.00
H2O+CH3<=>OH+CH3O	2.000E+13	0.000	0.00
H2O+CO<=>OH+CO2	1.500E+14	0.000	23600.00
H2O+CH2O<=>HCO+H2O2	1.000E+12	0.000	8000.00
CH2+O2<=>OH+HCO	1.320E+13	0.000	1500.00
CH2+H2<=>H+CH3	5.000E+05	2.000	7230.00
2CH2<=>H2+C2H2	3.200E+13	0.000	0.00
CH2+CH3<=>H+C2H4	4.000E+13	0.000	0.00
CH2+CH4<=>2CH3	2.460E+06	2.000	8270.00
CH2(S)+N2<=>CH2+N2	1.500E+13	0.000	600.00
CH2(S)+AR<=>CH2+AR	9.000E+12	0.000	600.00
CH2(S)+O2<=>H+OH+CO	2.800E+13	0.000	0.00
CH2(S)+O2<=>CO+H2O	1.200E+13	0.000	0.00
CH2(S)+H2<=>CH3+H	7.000E+13	0.000	0.00
CH2(S)+H2O<=>CH2+H2O	3.000E+13	0.000	0.00
CH2(S)+CH3<=>H+C2H4	1.200E+13	0.000	-570.00
CH2(S)+CH4<=>2CH3	1.600E+13	0.000	-570.00
CH2(S)+CO<=>CH2+CO	9.000E+12	0.000	0.00
CH2(S)+CO2<=>CH2+CO2	7.000E+12	0.000	0.00
CH2(S)+CO2<=>CO+CH2O	1.400E+13	0.000	0.00
CH3+O2<=>O+CH3O	2.675E+13	0.000	28800.00
CH3+O2<=>OH+CH2O	3.600E+10	0.000	8940.00
CH3+H2O2<=>H2O+CH4	2.450E+04	2.470	5180.00

```

2CH3(+M)<=>C2H6(+M)                2.120E+16  -0.970   620.00
    LOW /  1.770E+50  -9.670  6220.00/
    TROE/  0.5325 151.00 1038.00 4970.00 /
H2/2.00/ H2O/6.00/ CH4/2.00/ CO/1.50/ CO2/2.00/ C2H6/3.00/ AR/0.70/
2CH3<=>H+C2H5                        4.990E+12   0.100  10600.00
CH3+HCO<=>CH4+CO                     2.648E+13   0.000    0.00
CH3+CH2O<=>HCO+CH4                   3.320E+03   2.810   5860.00
CH3+C2H4<=>C2H3+CH4                  2.270E+05   2.000   9200.00
CH3+C2H6<=>C2H5+CH4                  6.140E+06   1.740  10450.00
HCO+H2O<=>H+CO+H2O                   2.244E+18  -1.000  17000.00
HCO+M<=>H+CO+M                       1.870E+17  -1.000  17000.00
H2/2.00/ H2O/0.00/ CH4/2.00/ CO/1.50/ CO2/2.00/ C2H6/3.00/
HCO+O2<=>HO2+CO                      7.600E+12   0.000   400.00
CH3O+O2<=>HO2+CH2O                   4.280E-13   7.600 -3530.00
C2H3+O2<=>HCO+CH2O                   3.980E+12   0.000  -240.00
C2H4(+M)<=>H2+C2H2(+M)                8.000E+12   0.440  88770.00
    LOW /  7.000E+50  -9.310 99860.00/
    TROE/  0.7345 180.00 1035.00 5417.00 /
H2/2.00/ H2O/6.00/ CH4/2.00/ CO/1.50/ CO2/2.00/ C2H6/3.00/ AR/0.70/
C2H5+O2<=>HO2+C2H4                   8.400E+11   0.000   3875.00
END

```

## A.2 Thermodynamics

```

THERMO
!300.000 1000.000 5000.000
! GRI-Mech Version 3.0 Thermodynamics released 7/30/99
! NASA Polynomial format for CHEMKIN-II
! see README file for disclaimer
0          L 1/900  1          G  200.000 3500.000 1000.000  1

```



2.56942078E+00-8.59741137E-05 4.19484589E-08-1.00177799E-11 1.22833691E-15 2  
 2.92175791E+04 4.78433864E+00 3.16826710E+00-3.27931884E-03 6.64306396E-06 3  
 -6.12806624E-09 2.11265971E-12 2.91222592E+04 2.05193346E+00 4  
 02 TPIS890 2 G 200.000 3500.000 1000.000 1  
 3.28253784E+00 1.48308754E-03-7.57966669E-07 2.09470555E-10-2.16717794E-14 2  
 -1.08845772E+03 5.45323129E+00 3.78245636E+00-2.99673416E-03 9.84730201E-06 3  
 -9.68129509E-09 3.24372837E-12-1.06394356E+03 3.65767573E+00 4  
 H L 7/88H 1 G 200.000 3500.000 1000.000 1  
 2.50000001E+00-2.30842973E-11 1.61561948E-14-4.73515235E-18 4.98197357E-22 2  
 2.54736599E+04-4.46682914E-01 2.50000000E+00 7.05332819E-13-1.99591964E-15 3  
 2.30081632E-18-9.27732332E-22 2.54736599E+04-4.46682853E-01 4  
 H2 TPIS78H 2 G 200.000 3500.000 1000.000 1  
 3.33727920E+00-4.94024731E-05 4.99456778E-07-1.79566394E-10 2.00255376E-14 2  
 -9.50158922E+02-3.20502331E+00 2.34433112E+00 7.98052075E-03-1.94781510E-05 3  
 2.01572094E-08-7.37611761E-12-9.17935173E+02 6.83010238E-01 4  
 OH RUS 780 1H 1 G 200.000 3500.000 1000.000 1  
 3.09288767E+00 5.48429716E-04 1.26505228E-07-8.79461556E-11 1.17412376E-14 2  
 3.85865700E+03 4.47669610E+00 3.99201543E+00-2.40131752E-03 4.61793841E-06 3  
 -3.88113333E-09 1.36411470E-12 3.61508056E+03-1.03925458E-01 4  
 H20 L 8/89H 20 1 G 200.000 3500.000 1000.000 1  
 3.03399249E+00 2.17691804E-03-1.64072518E-07-9.70419870E-11 1.68200992E-14 2  
 -3.00042971E+04 4.96677010E+00 4.19864056E+00-2.03643410E-03 6.52040211E-06 3  
 -5.48797062E-09 1.77197817E-12-3.02937267E+04-8.49032208E-01 4  
 H02 L 5/89H 10 2 G 200.000 3500.000 1000.000 1  
 4.01721090E+00 2.23982013E-03-6.33658150E-07 1.14246370E-10-1.07908535E-14 2  
 1.11856713E+02 3.78510215E+00 4.30179801E+00-4.74912051E-03 2.11582891E-05 3  
 -2.42763894E-08 9.29225124E-12 2.94808040E+02 3.71666245E+00 4  
 H202 L 7/88H 20 2 G 200.000 3500.000 1000.000 1  
 4.16500285E+00 4.90831694E-03-1.90139225E-06 3.71185986E-10-2.87908305E-14 2  
 -1.78617877E+04 2.91615662E+00 4.27611269E+00-5.42822417E-04 1.67335701E-05 3  
 -2.15770813E-08 8.62454363E-12-1.77025821E+04 3.43505074E+00 4

C	L11/88C	1		G	200.000	3500.000	1000.000	1
	2.49266888E+00	4.79889284E-05	-7.24335020E-08	3.74291029E-11	-4.87277893E-15	2		
	8.54512953E+04	4.80150373E+00	2.55423955E+00	-3.21537724E-04	7.33792245E-07	3		
	-7.32234889E-10	2.66521446E-13	8.54438832E+04	4.53130848E+00			4	
CH	TPIS79C	1H	1	G	200.000	3500.000	1000.000	1
	2.87846473E+00	9.70913681E-04	1.44445655E-07	-1.30687849E-10	1.76079383E-14	2		
	7.10124364E+04	5.48497999E+00	3.48981665E+00	3.23835541E-04	-1.68899065E-06	3		
	3.16217327E-09	-1.40609067E-12	7.07972934E+04	2.08401108E+00			4	
CH2	L S/93C	1H	2	G	200.000	3500.000	1000.000	1
	2.87410113E+00	3.65639292E-03	-1.40894597E-06	2.60179549E-10	-1.87727567E-14	2		
	4.62636040E+04	6.17119324E+00	3.76267867E+00	9.68872143E-04	2.79489841E-06	3		
	-3.85091153E-09	1.68741719E-12	4.60040401E+04	1.56253185E+00			4	
CH2(S)	L S/93C	1H	2	G	200.000	3500.000	1000.000	1
	2.29203842E+00	4.65588637E-03	-2.01191947E-06	4.17906000E-10	-3.39716365E-14	2		
	5.09259997E+04	8.62650169E+00	4.19860411E+00	-2.36661419E-03	8.23296220E-06	3		
	-6.68815981E-09	1.94314737E-12	5.04968163E+04	-7.69118967E-01			4	
CH3	L11/89C	1H	3	G	200.000	3500.000	1000.000	1
	2.28571772E+00	7.23990037E-03	-2.98714348E-06	5.95684644E-10	-4.67154394E-14	2		
	1.67755843E+04	8.48007179E+00	3.67359040E+00	2.01095175E-03	5.73021856E-06	3		
	-6.87117425E-09	2.54385734E-12	1.64449988E+04	1.60456433E+00			4	
CH4	L 8/88C	1H	4	G	200.000	3500.000	1000.000	1
	7.48514950E-02	1.33909467E-02	-5.73285809E-06	1.22292535E-09	-1.01815230E-13	2		
	-9.46834459E+03	1.84373180E+01	5.14987613E+00	-1.36709788E-02	4.91800599E-05	3		
	-4.84743026E-08	1.66693956E-11	-1.02466476E+04	-4.64130376E+00			4	
CO	TPIS79C	1O	1	G	200.000	3500.000	1000.000	1
	2.71518561E+00	2.06252743E-03	-9.98825771E-07	2.30053008E-10	-2.03647716E-14	2		
	-1.41518724E+04	7.81868772E+00	3.57953347E+00	-6.10353680E-04	1.01681433E-06	3		
	9.07005884E-10	-9.04424499E-13	-1.43440860E+04	3.50840928E+00			4	
CO2	L 7/88C	1O	2	G	200.000	3500.000	1000.000	1
	3.85746029E+00	4.41437026E-03	-2.21481404E-06	5.23490188E-10	-4.72084164E-14	2		
	-4.87591660E+04	2.27163806E+00	2.35677352E+00	8.98459677E-03	-7.12356269E-06	3		

	2.45919022E-09-1.43699548E-13-4.83719697E+04	9.90105222E+00	4
HCO	L12/89H 1C 10 1 G	200.000 3500.000 1000.000	1
	2.77217438E+00 4.95695526E-03-2.48445613E-06	5.89161778E-10-5.33508711E-14	2
	4.01191815E+03 9.79834492E+00 4.22118584E+00-3.24392532E-03	1.37799446E-05	3
	-1.33144093E-08 4.33768865E-12 3.83956496E+03	3.39437243E+00	4
CH2O	L 8/88H 2C 10 1 G	200.000 3500.000 1000.000	1
	1.76069008E+00 9.20000082E-03-4.42258813E-06	1.00641212E-09-8.83855640E-14	2
	-1.39958323E+04 1.36563230E+01 4.79372315E+00-9.90833369E-03	3.73220008E-05	3
	-3.79285261E-08 1.31772652E-11-1.43089567E+04	6.02812900E-01	4
CH2OH	GUNL93C 1H 30 1 G	200.000 3500.000 1000.000	1
	3.69266569E+00 8.64576797E-03-3.75101120E-06	7.87234636E-10-6.48554201E-14	2
	-3.24250627E+03 5.81043215E+00 3.86388918E+00	5.59672304E-03 5.93271791E-06	3
	-1.04532012E-08 4.36967278E-12-3.19391367E+03	5.47302243E+00	4
CH3O	121686C 1H 30 1 G	300.00 3000.00 1000.000	1
	0.03770799E+02 0.07871497E-01-0.02656384E-04	0.03944431E-08-0.02112616E-12	2
	0.12783252E+03 0.02929575E+02 0.02106204E+02	0.07216595E-01 0.05338472E-04	3
	-0.07377636E-07 0.02075610E-10 0.09786011E+04	0.13152177E+02	4
CH3OH	L 8/88C 1H 40 1 G	200.000 3500.000 1000.000	1
	1.78970791E+00 1.40938292E-02-6.36500835E-06	1.38171085E-09-1.17060220E-13	2
	-2.53748747E+04 1.45023623E+01 5.71539582E+00-1.52309129E-02	6.52441155E-05	3
	-7.10806889E-08 2.61352698E-11-2.56427656E+04-1.50409823E+00		4
C2H	L 1/91C 2H 1 G	200.000 3500.000 1000.000	1
	3.16780652E+00 4.75221902E-03-1.83787077E-06	3.04190252E-10-1.77232770E-14	2
	6.71210650E+04 6.63589475E+00 2.88965733E+00	1.34099611E-02-2.84769501E-05	3
	2.94791045E-08-1.09331511E-11 6.68393932E+04	6.22296438E+00	4
C2H2	L 1/91C 2H 2 G	200.000 3500.000 1000.000	1
	4.14756964E+00 5.96166664E-03-2.37294852E-06	4.67412171E-10-3.61235213E-14	2
	2.59359992E+04-1.23028121E+00 8.08681094E-01	2.33615629E-02-3.55171815E-05	3
	2.80152437E-08-8.50072974E-12 2.64289807E+04	1.39397051E+01	4
C2H3	L 2/92C 2H 3 G	200.000 3500.000 1000.000	1
	3.01672400E+00 1.03302292E-02-4.68082349E-06	1.01763288E-09-8.62607041E-14	2

	3.46128739E+04	7.78732378E+00	3.21246645E+00	1.51479162E-03	2.59209412E-05	3
	-3.57657847E-08	1.47150873E-11	3.48598468E+04	8.51054025E+00		4
C2H4	L 1/91C	2H	4	G	200.000 3500.000 1000.000	1
	2.03611116E+00	1.46454151E-02	-6.71077915E-06	1.47222923E-09	-1.25706061E-13	2
	4.93988614E+03	1.03053693E+01	3.95920148E+00	-7.57052247E-03	5.70990292E-05	3
	-6.91588753E-08	2.69884373E-11	5.08977593E+03	4.09733096E+00		4
C2H5	L12/92C	2H	5	G	200.000 3500.000 1000.000	1
	1.95465642E+00	1.73972722E-02	-7.98206668E-06	1.75217689E-09	-1.49641576E-13	2
	1.28575200E+04	1.34624343E+01	4.30646568E+00	-4.18658892E-03	4.97142807E-05	3
	-5.99126606E-08	2.30509004E-11	1.28416265E+04	4.70720924E+00		4
C2H6	L 8/88C	2H	6	G	200.000 3500.000 1000.000	1
	1.07188150E+00	2.16852677E-02	-1.00256067E-05	2.21412001E-09	-1.90002890E-13	2
	-1.14263932E+04	1.51156107E+01	4.29142492E+00	-5.50154270E-03	5.99438288E-05	3
	-7.08466285E-08	2.68685771E-11	-1.15222055E+04	2.66682316E+00		4
CH2CO	L 5/90C	2H	20	1	G 200.000 3500.000 1000.000	1
	4.51129732E+00	9.00359745E-03	-4.16939635E-06	9.23345882E-10	-7.94838201E-14	2
	-7.55105311E+03	6.32247205E-01	2.13583630E+00	1.81188721E-02	-1.73947474E-05	3
	9.34397568E-09	-2.01457615E-12	-7.04291804E+03	1.22156480E+01		4
HCCO	SRIC91H	1C	20	1	G 300.00 4000.00 1000.000	1
	0.56282058E+01	0.40853401E-02	-0.15934547E-05	0.28626052E-09	-0.19407832E-13	2
	0.19327215E+05	-0.39302595E+01	0.22517214E+01	0.17655021E-01	-0.23729101E-04	3
	0.17275759E-07	-0.50664811E-11	0.20059449E+05	0.12490417E+02		4
HCCOH	SRI91C	20	1H	2	G 300.000 5000.000 1000.000	1
	0.59238291E+01	0.67923600E-02	-0.25658564E-05	0.44987841E-09	-0.29940101E-13	2
	0.72646260E+04	-0.76017742E+01	0.12423733E+01	0.31072201E-01	-0.50866864E-04	3
	0.43137131E-07	-0.14014594E-10	0.80316143E+04	0.13874319E+02		4
H2CN	41687H	2C	1N	1	G 300.00 4000.000 1000.000	1
	0.52097030E+01	0.29692911E-02	-0.28555891E-06	-0.16355500E-09	0.30432589E-13	2
	0.27677109E+05	-0.44444780E+01	0.28516610E+01	0.56952331E-02	0.10711400E-05	3
	-0.16226120E-08	-0.23511081E-12	0.28637820E+05	0.89927511E+01		4
HCN	GRI/98H	1C	1N	1	G 200.000 6000.000 1000.000	1

0.38022392E+01	0.31464228E-02	-0.10632185E-05	0.16619757E-09	-0.97997570E-14	2
0.14407292E+05	0.15754601E+01	0.22589886E+01	0.10051170E-01	-0.13351763E-04	3
0.10092349E-07	-0.30089028E-11	0.14712633E+05	0.89164419E+01		4
HNO	And93	H	1N	10	1
			G	200.000	6000.000
0.29792509E+01	0.34944059E-02	-0.78549778E-06	0.57479594E-10	-0.19335916E-15	2
0.11750582E+05	0.86063728E+01	0.45334916E+01	-0.56696171E-02	0.18473207E-04	3
-0.17137094E-07	0.55454573E-11	0.11548297E+05	0.17498417E+01		4
N	L	6/88N	1		
			G	200.000	6000.000
0.24159429E+01	0.17489065E-03	-0.11902369E-06	0.30226245E-10	-0.20360982E-14	2
0.56133773E+05	0.46496096E+01	0.25000000E+01	0.00000000E+00	0.00000000E+00	3
0.00000000E+00	0.00000000E+00	0.56104637E+05	0.41939087E+01		4
NNH	T07/93N	2H	1		
			G	200.000	6000.000
0.37667544E+01	0.28915082E-02	-0.10416620E-05	0.16842594E-09	-0.10091896E-13	2
0.28650697E+05	0.44705067E+01	0.43446927E+01	-0.48497072E-02	0.20059459E-04	3
-0.21726464E-07	0.79469539E-11	0.28791973E+05	0.29779410E+01		4
N2O	L	7/88N	2O	1	
			G	200.000	6000.000
0.48230729E+01	0.26270251E-02	-0.95850874E-06	0.16000712E-09	-0.97752303E-14	2
0.80734048E+04	-0.22017207E+01	0.22571502E+01	0.11304728E-01	-0.13671319E-04	3
0.96819806E-08	-0.29307182E-11	0.87417744E+04	0.10757992E+02		4
NH	And94	N	1H	1	
			G	200.000	6000.000
0.27836928E+01	0.13298430E-02	-0.42478047E-06	0.78348501E-10	-0.55044470E-14	2
0.42120848E+05	0.57407799E+01	0.34929085E+01	0.31179198E-03	-0.14890484E-05	3
0.24816442E-08	-0.10356967E-11	0.41880629E+05	0.18483278E+01		4
NH2	And89	N	1H	2	
			G	200.000	6000.000
0.28347421E+01	0.32073082E-02	-0.93390804E-06	0.13702953E-09	-0.79206144E-14	2
0.22171957E+05	0.65204163E+01	0.42040029E+01	-0.21061385E-02	0.71068348E-05	3
-0.56115197E-08	0.16440717E-11	0.21885910E+05	-0.14184248E+00		4
NH3	J	6/77N	1H	3	
			G	200.000	6000.000
0.26344521E+01	0.56662560E-02	-0.17278676E-05	0.23867161E-09	-0.12578786E-13	2
-0.65446958E+04	0.65662928E+01	0.42860274E+01	-0.46605230E-02	0.21718513E-04	3
-0.22808887E-07	0.82638046E-11	-0.67417285E+04	-0.62537277E+00		4

NO	RUS 78N	10	1	G	200.000	6000.000	1000.000	1
	0.32606056E+01	0.11911043E-02	-0.42917048E-06	0.69457669E-10	-0.40336099E-14	2		
	0.99209746E+04	0.63693027E+01	0.42184763E+01	-0.46389760E-02	0.11041022E-04	3		
	-0.93361354E-08	0.28035770E-11	0.98446230E+04	0.22808464E+01		4		
NO2	L 7/88N	10	2	G	200.000	6000.000	1000.000	1
	0.48847542E+01	0.21723956E-02	-0.82806906E-06	0.15747510E-09	-0.10510895E-13	2		
	0.23164983E+04	-0.11741695E+00	0.39440312E+01	-0.15854290E-02	0.16657812E-04	3		
	-0.20475426E-07	0.78350564E-11	0.28966179E+04	0.63119917E+01		4		
HCNO	BDEA94H	1N	1C	10	1G	300.000	5000.000	1382.000
	6.59860456E+00	3.02778626E-03	-1.07704346E-06	1.71666528E-10	-1.01439391E-14	2		
	1.79661339E+04	-1.03306599E+01	2.64727989E+00	1.27505342E-02	-1.04794236E-05	3		
	4.41432836E-09	-7.57521466E-13	1.92990252E+04	1.07332972E+01		4		
HOCN	BDEA94H	1N	1C	10	1G	300.000	5000.000	1368.000
	5.89784885E+00	3.16789393E-03	-1.11801064E-06	1.77243144E-10	-1.04339177E-14	2		
	-3.70653331E+03	-6.18167825E+00	3.78604952E+00	6.88667922E-03	-3.21487864E-06	3		
	5.17195767E-10	1.19360788E-14	-2.82698400E+03	5.63292162E+00		4		
HNCO	BDEA94H	1N	1C	10	1G	300.000	5000.000	1478.000
	6.22395134E+00	3.17864004E-03	-1.09378755E-06	1.70735163E-10	-9.95021955E-15	2		
	-1.66599344E+04	-8.38224741E+00	3.63096317E+00	7.30282357E-03	-2.28050003E-06	3		
	-6.61271298E-10	3.62235752E-13	-1.55873636E+04	6.19457727E+00		4		
NCO	EA 93 N	1C	10	1	G	200.000	6000.000	1000.000
	0.51521845E+01	0.23051761E-02	-0.88033153E-06	0.14789098E-09	-0.90977996E-14	2		
	0.14004123E+05	-0.25442660E+01	0.28269308E+01	0.88051688E-02	-0.83866134E-05	3		
	0.48016964E-08	-0.13313595E-11	0.14682477E+05	0.95504646E+01		4		
CN	HBH92 C	1N	1	G	200.000	6000.000	1000.000	1
	0.37459805E+01	0.43450775E-04	0.29705984E-06	-0.68651806E-10	0.44134173E-14	2		
	0.51536188E+05	0.27867601E+01	0.36129351E+01	-0.95551327E-03	0.21442977E-05	3		
	-0.31516323E-09	-0.46430356E-12	0.51708340E+05	0.39804995E+01		4		
HCNN	SRI/94C	1N	2H	1	G	300.000	5000.000	1000.000
	0.58946362E+01	0.39895959E-02	-0.15982380E-05	0.29249395E-09	-0.20094686E-13	2		
	0.53452941E+05	-0.51030502E+01	0.25243194E+01	0.15960619E-01	-0.18816354E-04	3		

```

0.12125540E-07-0.32357378E-11 0.54261984E+05 0.11675870E+02          4
N2          121286N  2          G  300.000 5000.000 1000.000  1
0.02926640E+02 0.14879768E-02-0.05684760E-05 0.10097038E-09-0.06753351E-13 2
-0.09227977E+04 0.05980528E+02 0.03298677E+02 0.14082404E-02-0.03963222E-04 3
0.05641515E-07-0.02444854E-10-0.10208999E+04 0.03950372E+02          4
AR          120186AR 1          G  300.000 5000.000 1000.000  1
0.02500000E+02 0.00000000E+00 0.00000000E+00 0.00000000E+00 0.00000000E+00 2
-0.07453750E+04 0.04366000E+02 0.02500000E+02 0.00000000E+00 0.00000000E+00 3
0.00000000E+00 0.00000000E+00-0.07453750E+04 0.04366000E+02          4
C3H8        L 4/85C  3H  8          G  300.000 5000.000 1000.000  1
0.75341368E+01 0.18872239E-01-0.62718491E-05 0.91475649E-09-0.47838069E-13 2
-0.16467516E+05-0.17892349E+02 0.93355381E+00 0.26424579E-01 0.61059727E-05 3
-0.21977499E-07 0.95149253E-11-0.13958520E+05 0.19201691E+02          4
C3H7        L 9/84C  3H  7          G  300.000 5000.000 1000.000  1
0.77026987E+01 0.16044203E-01-0.52833220E-05 0.76298590E-09-0.39392284E-13 2
0.82984336E+04-0.15480180E+02 0.10515518E+01 0.25991980E-01 0.23800540E-05 3
-0.19609569E-07 0.93732470E-11 0.10631863E+05 0.21122559E+02          4
CH3CHO      L 8/88C  2H  40  1      G  200.000 6000.000 1000.000  1
0.54041108E+01 0.11723059E-01-0.42263137E-05 0.68372451E-09-0.40984863E-13 2
-0.22593122E+05-0.34807917E+01 0.47294595E+01-0.31932858E-02 0.47534921E-04 3
-0.57458611E-07 0.21931112E-10-0.21572878E+05 0.41030159E+01          4
CH2CHO      SAND860  1H  3C  2      G  300.000 5000.000 1000.000  1
0.05975670E+02 0.08130591E-01-0.02743624E-04 0.04070304E-08-0.02176017E-12 2
0.04903218E+04-0.05045251E+02 0.03409062E+02 0.10738574E-01 0.01891492E-04 3
-0.07158583E-07 0.02867385E-10 0.15214766E+04 0.09558290E+02          4
END

```

## Input Files

```

/*-----*-- C++ --*-----*/
| ===== |
| \\      / F ield      | OpenFOAM: The Open Source CFD Toolbox |
| \\      / O peration   | Version: 3.0.x                       |
| \\      / A nd          | Web:      www.OpenFOAM.org          |
|   \\\\   M anipulation |                                     |
/*-----*-----*/

FoamFile
{
    version      2.0;
    format       ascii;
    class        dictionary;
    location      "constant";
    object        coalCloud1Properties;
}

// * * * * *

solution

```



```

{
    active          true;
    transient       yes;
    coupled         true;
    cellValueSourceCorrection on;

    sourceTerms
    {
        schemes
        {
            rho          semiImplicit 1;
            U            semiImplicit 1;
            Yi           semiImplicit 1;
            h            semiImplicit 1;
            radiation     semiImplicit 1;
        }
    }

    interpolationSchemes
    {
        rho            cell;
        U              cellPoint;
        thermo:mu       cell;
        T              cell;
        Cp             cell;
        kappa          cell;
        p              cell;
        G              cell;
    }
}

```

```

    integrationSchemes
    {
        U            Euler;
        T            analytical;
    }
}

constantProperties
{
    rho0            1000;
    T0              295;
    Cp0             1600;
    epsilon0        1;
    f0              0.5;

    TDevol          400;
    LDevol          0;
    hRetentionCoeff 1;

    constantVolume true;
}

subModels
{
    particleForces
    {
        sphereDrag;
        gravity;
    }

    injectionModels

```

```

{
  model1
  {
    type          patchInjection;
    massFlowRate  3.472e-8; //(foraxisymmetric) !mass flow arte in the
                  [+]experiment was 1.5 g/h
    massTotal     3.472e-7; // 10 s
    SOI           0;
    parcelBasisType mass;
    patchName     Coal_in;
    parcelsPerSecond 2.06318e+02; //Particle/s 2.06318e+02
    duration      10; //[s]
    U0            (1.899 0 0);
    flowRateProfile constant 1.0;
    sizeDistribution
    {
      type        uniform;
      fixedValueDistribution
      {
        value     20e-06; // 20 micrometers diameter
      }
      uniformDistribution
      {
        minValue  63e-06;
        maxValue  74e-06;
      }
    }
  }
}

```

```

dispersionModel none;

patchInteractionModel standardWallInteraction;

heatTransferModel RanzMarshall;

compositionModel singleMixtureFraction;

phaseChangeModel liquidEvaporation;

devolatilisationModel nthOrderDevolatilisation;

stochasticCollisionModel none;

surfaceReactionModel none;

surfaceFilmModel none;

radiation      on;

standardWallInteractionCoeffs
{
    type          rebound;
    //e           1;
    //mu          0;
}

RanzMarshallCoeffs
{
    BirdCorrection true;

```

```

}

singleMixtureFractionCoeffs
{
    phases
    (
        gas
        {
            // Taken from C3M/CPD
            // 298.15 - 1803 K
            // Same conditions as corresponding PCCL cases
            // For utah Hiawatha
            // See CPD to OF sheet for calculation

            TAR          0.55;
            CO           0.086;
            CO2          0.059;
            CH4          0.155;
            H2O          0.15;
        }
        liquid
        {
            H2O          1.0;
        }
        solid
        {
            // ash fraction directly from proximate
            // YSolid known from calulations
            // can be use to find these numbers

            // Y_C should be .386 from calcs,
            // somewhat independent check and it works out well

```

```

        ash            0.18;
        C              0.82;
    }

);

    // Water fraction was determined directly from
// the prox analysis. Others from CPD output files of C3M.
    // See the CPD to OF sheet to for details

    // daf fraction = 0.84
    YGasTot0          .454;
    YLiquidTot0       .076;
    YSolidTot0        .47;
}

liquidEvaporationCoeffs
{
    enthalpyTransfer enthalpyDifference;

    activeLiquids
    (
        H2O
    );
}

nthOrderDevolatilisationCoeffs
{
    // Taken from C3M CPD output. Utah Hiawatha coal
    // 298.15 - 1803 K
    // Same conditions as corresponding PCCL cases

```

```

        volatileData
    (
        (TAR      1.849e25  414175  6.73643)
          (H2O      1.849e25  414175  6.73643)
        (CH4      1.849e25  414175  6.73643)
        (CO       1.849e25  414175  6.73643)
        (CO2      1.849e25  414175  6.73643)
    );
        residualCoeff 0.001;
    }
}
// ***** //

```

# References

- [1] A. Dasgupta, “Numerical simulation of axisymmetric laminar diffusion flames with soot,” Ph.D. dissertation, Pennsylvania State University, 2015.
- [2] J. Ma, “Soot Formation During Coal Pyrolysis,” Ph.D. dissertation, Brigham Young University, 1996.
- [3] A. Brown, “Modeling soot in pulverized coal flames,” Ph.D. dissertation, Brigham Young University, 1997.
- [4] “Advanced Research Computing Center. 2012. Mount Moran: IBM System X cluster. Laramie, WY: University of Wyoming. <http://n2t.net/ark:/85786/m4159c>.”
- [5] H. G. Weller and G. Tabor, “A tensorial approach to computational continuum mechanics using object-oriented techniques,” *Computers in Physics*, vol. 12, no. 6, pp. 620–631, 1998.
- [6] T. H. Fletcher, A. R. Kerstein, R. J. Pugmire, and D. M. Grant, “Chemical percolation model for devolatilization. 2. Temperature and heating rate effects on product yields,” *Energy & Fuels*, vol. 4, no. 1, pp. 54–60, 1990. [Online]. Available: <http://pubs.acs.org/doi/abs/10.1021/ef00019a010>
- [7] J. Gibbins-Matham and R. Kandiyoti, “Coal Pyrolysis Yields from Fast and Slow Heating in a Wire-Mesh Apparatus with a Gas Sweep,” *Energy and Fuels*, vol. 2, no. 4, pp. 505–511, 1988.
- [8] S. Badzioch and P. Hawksley, “Kinetics of Thermal Decomposition of Pulverized Coal Particles,” *Ind. Eng. Chem. Proc. Des. Dev.*, Jan. 1970. [Online]. Available: [http://pubs.acs.org/cgi-bin/abstract.cgi/iepdaw/1970/9/i04/f-pdf/f\\\_i260036a005.pdf?sessid=600613](http://pubs.acs.org/cgi-bin/abstract.cgi/iepdaw/1970/9/i04/f-pdf/f\_i260036a005.pdf?sessid=600613)
- [9] W. Fu, Y. Zhang, H. Han, and D. Wang, “A general model of pulverized coal devolatilization,” *Fuel*, vol. 68, no. 4, pp. 505–510, apr 1989. [Online]. Available: <https://www.sciencedirect.com/science/article/pii/0016236189902743>
- [10] D. Anthony, J. Howard, H. Hottel, and H. Meissner, “Rapid devolatilization of pulverized coal,” *Symposium (International) on Combustion*, vol. 15, no. 1, pp. 1303–1317, jan 1975. [Online]. Available: <https://www.sciencedirect.com/science/article/pii/S0082078475803924>



- [11] D. M. Grant, R. J. Pugmire, T. H. Fletcher, and A. R. Kerstein, "Chemical Model of Coal Devolatilization Using Percolation Lattice Statistics," *Energy and Fuels*, vol. 3, no. 2, pp. 175–186, 1989.
- [12] "P.C. Coal Lab Version 5.0." [Online]. Available: [www.niksaenergy.com/products/pc-coal-lab](http://www.niksaenergy.com/products/pc-coal-lab)
- [13] "C3M chemistry management software," <https://mfix.netl.doe.gov/c3m/>.
- [14] A. L. Brown and T. H. Fletcher, "Modeling Soot Derived from Pulverized Coal," *Energy & Fuels*, vol. 84602, no. 8, pp. 745–757, 1998.
- [15] J. Rigby, J. Ma, B. W. Webb, and T. H. Fletcher, "Transformations of coal-derived soot at elevated temperature," *Energy and Fuels*, vol. 15, no. 1, pp. 52–59, 2001.
- [16] D. Bradley, M. Lawes, H. Y. Park, and N. Usta, "Modeling of laminar pulverized coal flames with speciated devolatilization and comparisons with experiments," *Combustion and Flame*, vol. 144, no. 1-2, pp. 190–204, 2006.
- [17] L. D. Smoot, M. D. Horton, and G. A. Williams, "Propagation of laminar pulverized coal-air flames," *Symposium (International) on Combustion*, vol. 16, no. 1, pp. 375–387, jan 1977. [Online]. Available: <https://www.sciencedirect.com/science/article/pii/S008207847780338X>
- [18] I. M. Kennedy, "Models of soot formation and oxidation," *Progress in Energy and Combustion Science*, vol. 23, no. 2, pp. 95 – 132, 1997. [Online]. Available: <http://www.sciencedirect.com/science/article/pii/S0360128597000075>
- [19] H. Calcote and D. Manos, "Effect of molecular structure on incipient soot formation," *Combustion and Flame*, vol. 49, no. 1, pp. 289 – 304, 1983. [Online]. Available: <http://www.sciencedirect.com/science/article/pii/0010218083901724>
- [20] K. Leung, R. Lindstedt, and W. Jones, "A simplified reaction mechanism for soot formation in nonpremixed flames," *Combustion and Flame*, vol. 87, no. 3-4, pp. 289–305, dec 1991. [Online]. Available: <https://www.sciencedirect.com/science/article/pii/001021809190114Q>
- [21] H. Guo, F. Liu, and G. J. Smallwood, "Soot and NO formation in counterflow ethylene/oxygen/nitrogen diffusion flames," *Combustion Theory and Modelling*, vol. 8, no. 3, pp. 475–489, 2004.
- [22] J. Moss, C. Stewart, and K. Syed, "Flowfield modelling of soot formation at elevated pressure," *Symposium (International) on Combustion*, vol. 22, no. 1, pp. 413–423, jan 1989. [Online]. Available: <https://www.sciencedirect.com/science/article/pii/S0082078489800487>

- [23] C. D. Stewart, K. J. Syed, and J. B. Moss, “Modelling soot formation in non-premixed kerosine-air flames,” *Combustion Science and Technology*, vol. 75, no. 4-6, pp. 211–226, 1991.
- [24] I. M. Kennedy, W. Kollmann, and J.-Y. Chen, “A model for soot formation in a laminar diffusion flame,” *Combustion and Flame*, vol. 81, no. 1, pp. 73–85, jul 1990. [Online]. Available: <https://www.sciencedirect.com/science/article/pii/001021809090071X>
- [25] M. Frenklach, “Method of moments with interpolative closure,” *Chemical Engineering Science*, vol. 57, no. 12, pp. 2229–2239, jun 2002. [Online]. Available: <https://www.sciencedirect.com/science/article/pii/S0009250902001136?via%3Dihub>
- [26] B. R. Adams and P. J. Smith, “Modeling effects of soot and turbulence-radiation coupling on radiative transfer in turbulent gaseous combustion,” *Combustion Science and Technology*, vol. 109, no. 1-6, pp. 121–140, 1995.
- [27] D. M. Christ, “The Effect of Char Kinetics on the Combustion of Pulverized Coal under Oxyfuel Conditions,” Ph.D. dissertation, Rheinisch-Westfälische Technische Hochschule Aachen, 2013. [Online]. Available: <http://publications.rwth-aachen.de/record/459438/files/5065.pdf>
- [28] A. Kazakov and M. Frenklach, “DRM22.” [Online]. Available: <http://www.me.berkeley.edu/drm/>
- [29] C. K. Law, *Combustion Physics*. Cambridge University Press, 2006.
- [30] E. Hairer and G. Wanner, *Solving Ordinary Differential Equations II*, ser. Springer Series in Computational Mathematics. Berlin, Heidelberg: Springer Berlin Heidelberg, 1996, vol. 14. [Online]. Available: <http://link.springer.com/10.1007/978-3-642-05221-7>
- [31] P. J. Coelho and M. G. Carvalho, “A Conservative Formulation of the Discrete Transfer Method,” *Transactions of the ASME - Journal of Heat Transfer*, vol. 119, pp. 118–128, 1997.
- [32] M. F. Modest, *Radiative Heat Transfer*. New York: McGraw-Hill, 1993.
- [33] M. J. Yu, S. W. Baek, and S. J. Kang, “Modeling of Pulverized Coal Combustion with Non-Gray Gas Radiation Effects,” *Combustion Science and Technology*, vol. 166, pp. 151–174, 2001.
- [34] W. Ranz and W. Marshall, “Evaporation from drops: Part 1 No Title,” *Chemical Engineering Progress*, vol. 48, no. 3, pp. 141–146, 1952.
- [35] —, “Evaporation from drops: Part 2,” *Chemical Engineering Progress*, vol. 48, no. 4, pp. 173–180, 1952.

- [36] K. Xu, H. Zhang, Y. Wu, M. Baroncelli, and H. Pitsch, “Transient model for soot formation during the combustion of single coal particles,” *Proceedings of the Combustion Institute*, vol. 36, no. 2, pp. 2131–2138, 2017. [Online]. Available: <http://dx.doi.org/10.1016/j.proci.2016.06.146>
- [37] A. Kronenburg, R. W. Bilger, and J. H. Kent, “Modeling soot formation in turbulent methane-air jet diffusion flames,” *Combustion and Flame*, vol. 121, no. 1-2, pp. 24–40, 2000.
- [38] A. J. Josephson, N. D. Gaffin, S. T. Smith, T. H. Fletcher, and D. O. Lignell, “Modeling Soot Oxidation and Gasification with Bayesian Statistics,” *Energy and Fuels*, vol. 31, no. 10, pp. 11 291–11 303, 2017.
- [39] A. Burcat, “Prof. Burcat’s Thermodynamic Data.” [Online]. Available: <http://garfield.chem.elte.hu/Burcat/burcat.html>
- [40] K. Xu, Y. Wu, H. Shen, Q. Zhang, and H. Zhang, “Predictions of soot formation and its effect on the flame temperature of a pulverized coal-air turbulent jet,” *Fuel*, vol. 194, no. x, pp. 297–305, 2017. [Online]. Available: <http://dx.doi.org/10.1016/j.fuel.2017.01.032>
- [41] A. J. Josephson, D. O. Lignell, A. L. Brown, and T. H. Fletcher, “Erratum: Revision to Modeling Soot Derived from Pulverized Coal (Energy and Fuels (1998) 12: 4 (745-757) DOI: 10.1021/ef9702207),” *Energy and Fuels*, vol. 30, no. 6, pp. 5198–5199, 2016.
- [42] J. C. Chen, C. Castagnoli, and S. Niksa, “Coal devolatilization during rapid transient heating. 2. Secondary pyrolysis,” *Energy & Fuels*, vol. 6, no. 3, pp. 264–271, 1992.
- [43] J. C. Chen and S. Niksa, “Coal devolatilization during rapid transient heating. 1. Primary devolatilization,” *Energy & Fuels*, vol. 6, no. 3, pp. 254–264, 1992.
- [44] D. G. Goodwin, H. K. Moffat, and R. L. Speth, “Cantera: An object-oriented software toolkit for chemical kinetics, thermodynamics, and transport processes,” <http://www.cantera.org>, 2017, version 2.3.0.
- [45] S. Niksa, “FLASHCHAIN Theory for Rapid Coal Devolatilization Kinetics. 11. Tar Hydroconversion during Hydrogasification of Any Coal,” *Energy and Fuels*, vol. 32, no. 7, pp. 7569–7584, 2018.